NTNU – Trondheim
Norwegian University of
Science and Technology

Hydroelastic Analysis of Flexible Wedges

Olav Aagaard

Marine Technology
Submission date: June 2013
Supervisor: Bernt Johan Leira, IMT
Co-supervisor: Bjørnar Pettersen, IMT
Svein Erling Heggelund, DNV

Norwegian University of Science and Technology
Department of Marine Technology

I. ABSTRACT

This thesis presents a simulation method for analyzing the coupled water entry problem of elastic bodies. The water entry problem is investigated using the software STAR CCM+ for computational fluid dynamics and Abaqus for finite element analyses.

Relevant literature on theory and numerical methods on water impact and fluid-structure interactions has been reviewed.

A model has been created in STAR CCM+ to analyze the water entry of rigid wedges. Convergence tests have been performed with respect to relevant parameters, and the method is verified through comparison with previous work. The agreement is good. The effect of viscosity and compressibility is investigated.

A model has been created in Abaqus to analyze the structural response of the water impact. Convergence tests with respect to relevant parameters have been conducted, and the method is verified through comparison to theory. The agreement is very good.

A co-simulation model with STAR CCM+ and Abaqus has been created. The hydroelastic water entry of deformable wedges is analyzed. The problem is analyzed with one-way coupling and two-way coupling. One-way coupling means that hydrodynamic pressures are exported to the structural model, and two-way coupling means that structural deformations are exported to the hydrodynamic model as well. Different coupling schemes are investigated, and numerical parameters governing the nature of the coupling are assessed.

Results from the coupled numerical model have been compared to experimental data. The agreement is poor, due to failure in properly recreating the experimental environment in the numerical model. Recommendations for experimental verification of the model are presented.

A parameter study has been conducted with respect to elasticity for the wedge impact, and the effect of structural nonlinearity has been assessed. It is found that the coupled solution for the structural response of a low-stiffness wedge exceeds the quasi-static response to an equivalent pressure.

Recommendations for future work with FSI-simulations on the water entry problem are presented.

II. SAMMENDRAG

Denne oppgaven presenterer en simuleringsmetode for å gjennomføre koblede, hydroelastiske analyser av legemer som treffer havoverflaten, såkalt «slamming». Problemet analyseres ved hjelp av numerisk strømningsmekanikk og elementmetoden. Programmene STAR CCM+ og Abaqus er brukt i analysene.

Litteratur om både teori og numeriske metoder for slamming og for hydroelastisitet har blitt gjennomgått.

En modell for å undersøke slamming av stive kiler har blitt laget i STAR CCM+. Konvergenstester med hensyn til relevante parametere har blitt gjennomført, og metoden verifiseres ved sammenligning med tidligere resultater. Overensstemmelsen er god. Effekten av kompressibilitet og viskositet for slammingproblemet blir også undersøkt.

En modell for å undersøke strukturresponsen for elastiske kiler har blitt laget i Abaqus. Konvergenstester med hensyn til relevante parametere har blitt gjennomført, og metoden verifiseres ved sammenligning med analytiske uttrykk for strukturrespons. Overensstemmelsen er svært god.

En koblet modell for å undersøke hydroelastisk slamming av fleksible kiler har blitt laget i STAR CCM+ og Abaqus. Slammingproblemet analyseres ved enveiskobling og ved toveiskobling av programmene. Enveiskobling innebærer at hydrodynamiske trykk beregnes i STAR CCM+ og brukes som last i en dynamisk elementanalyse i Abaqus. Toveiskobling innebærer at deformasjoner også overføres tilbake til den hydrodynamiske modellen. Forskjellige koblingsalgoritmer undersøkes, og de numeriske parameterne som styrer koblingsalgoritmen blir vurdert.

Resultater fra toveiskoblede analyser blir sammenlignet med eksperimentelle målinger. Overensstemmelsen er dårlig, fordi den numeriske modellen ikke ble laget slik at den gjengir fysikken i eksperimentet korrekt. Det foreslås alternative eksperimenter for å verifisere metoden.

En parameterstudie har blitt gjennomført, der elastisitetsmodulen til kilen varieres. Effekt av ikke-lineær respons undersøkes. Det konkluderes med at strukturresponsen som oppnås ved koblede hydroelastiske analyser overgår strukturresponsen funnet ved en kvasi-statisk responsanalyse basert på ekvivalente trykk fra de rigide impactsimuleringene.

Anbefalinger til videre arbeid med hydroelastiske simuleringer presenteres avslutningsvis.

III. PREFACE

The work resulting in this master's thesis has been carried out partly at NTNU, Department of Marine Technology, and partly at the offices of Det Norske Veritas (DNV) at Høvik. The assignment has been to investigate the coupled fluid-structure interaction problem of elastic wedges entering water. The initial months of the work were spend reviewing literature and theory on water impact and fluid-structure interactions, as well as getting familiarized with the relevant computer programs. The rest of the work has consisted of simulations and result analysis.

The thesis was written in spring 2013. The scope was proposed by my supervisor at DNV, Svein Erling Heggelund. I want to thank him for his excellent guidance and stimulating discussions, which helped me through halts and struggles along the way.

I would like to thank DNV for their hospitality and encouraging staff during the months that were spent at their offices. Thanks to Kristoffer Brinchmann and Cosmin Ciortan for their specialist opinions and guidance in their respective fields.

I would like to thank my supervisor Bernt Johan Leira at NTNU, for his encouraging guidance throughout the work. Thanks also to my co-supervisor Bjørnar Pettersen at NTNU for opinions of computational fluid dynamics.

Finally, I would like to thank Michael Glockenmeier and Rafael Ritterbusch from CD-ADAPCO for their supportive and friendly assistance along the way. Ritterbusch went the extra mile to help me with my simulations, and Glockenmeier saw to it that my experience with STAR CCM+ progressed as smoothly as possible.

Trondheim, June 07th 2013

Olav Aagaard

IV. PROJECT DESCRIPTION

Master Thesis, Spring 2013

for

Olav Aagaard

Hydroelastic Analysis of Flexible Wedges

Hydroelastisk Analyse av Fleksible Kiler

During the recent years, an increasing interest related to design and integrity of free fall lifeboats has been observed. Traditional calculation procedures for this type of hull structure have been insufficient and need to be further developed. The response consists both of quasi- static response, which is due to loads that are varying relatively slowly, and dynamic transient response caused by water impact and other effects. The flexibility of a lifeboat hull made out of composite material is much larger than the flexibility of a conventional steel ship structure. Therefore, the effect of hydroelasticity can be important.

The objective of this master thesis is to investigate the hydroelastic response of the lifeboat structure as it enters the water. This will be addressed using a two-way coupled numerical simulation for the fluid-structure interaction. The work will consist of:

1. A review of literature related to hydroelastic slamming as well as coupled fluid-structure simulations is to be performed and summarized.

2. Based on item 1, a set of computer programs is to be selected for the numerical analysis. It is expected that different computer programs will need to be coupled in order to achieve the objective of a satisfactory hydro-elastic analysis. Familiarity with the selected software is to be gained.

3. A reliable scheme for coupling of the selected software is to be developed. A simplified model of the free-fall lifeboat is to be established for the purpose of numerical load and response analysis.

4. Systematic convergence tests of the mesh refinement and parameters related to the simulation procedures are to be performed for the model from item 3.

5. Parameter studies in relation to the physical descriptors of the impact problem are to be performed for the numerical model. Comparison is to be made with response analyses

based on decoupled solutions for the load and response. Comparison is to be made with analytical solutions and experiments to the extent that such are available.

The work may turn out to be more extensive than expected. Therefore, some items may be omitted after consultation with the teaching supervisor without having a negative impact on the evaluation."

The work scope may prove to be larger than initially anticipated. Subject to approval from the supervisor, topics may be deleted from the list above or reduced in extent.

In the thesis the candidate shall present his personal contribution to the resolution of problems within the scope of the thesis work.

Theories and conclusions should be based on mathematical derivations and/or logic reasoning identifying the various steps in the deduction.

The candidate should utilise the existing possibilities for obtaining relevant literature.

The thesis should be organised in a rational manner to give a clear exposition of results, assessments, and conclusions. The text should be brief and to the point, with a clear language. Telegraphic language should be avoided.

The thesis shall contain the following elements: A text defining the scope, preface, list of contents, summary, main body of thesis, conclusions with recommendations for further work, list of symbols and acronyms, references and (optional) appendices. All figures, tables and equations shall be numbered.

The supervisor may require that the candidate, in an early stage of the work, presents a written plan for the completion of the work. The plan should include a budget for the use of computer and laboratory resources which will be charged to the department. Overruns shall be reported to the supervisor.

The original contribution of the candidate and material taken from other sources shall be clearly defined. Work from other sources shall be properly referenced using an acknowledged referencing system.

The thesis shall be submitted in 3 copies:

- Signed by the candidate
- The text defining the scope included
- In bound volume(s)
- Drawings and/or computer prints which cannot be bound should be organised in a separate folder.

Supervisor: Professor Bernt J. Leira

Co-supervisor: Bjørnar Pettersen

Contact person in DNV: Svein Erling Heggelund

Deadline: June 11th 2013

Trondheim, January 14th 2013

Bernt J. Leira

Bjørnar Pettersen

V. TABLE OF CONTENT

VI. LIST OF FIGURES

VII. TABLE OF TABLES

VIII. NOMENCLATURE

Some symbols may have different meaning in the different sections. This is defined at first appearance in the text. Vector and matrices are written in bold face.

A	Cross sectional area
A_{33}	Added mass in heave
$\boldsymbol{C}$	Damping matrix
c	Speed of sound
$c(t)$	Wetted length
C_p	Pressure coefficient
E	Young's modulus
F	Force
$\boldsymbol{f}$	Volume forces
g	Acceleration of gravity
I	Moment of inertia
$\boldsymbol{K}$	Stiffness matrix
$\boldsymbol{K_o}$	Matrix of linear stiffness terms
$\boldsymbol{K_\sigma}$	Matrix of nonlinear stiffness terms
L	Length of wedge plate
ΔL	Elongation of wedge plate
$\boldsymbol{M}$	Mass matrix
M	Mass
P	Axial force
p	Pressure
q	Evenly distributed load
$\boldsymbol{R}$	Load vector
$\boldsymbol{r}$	Displacement vector
T_1	First eigenperiod of the wedge plate
V	Impact velocity
$\mathbf{v}$	Velocity field
w	Deformation
w_0	Maximum deformation
WQ	Wetting time quotient
z_a	Distance to neutral axis
α	Volume fraction of fluid
ε	Strain
μ	Dynamic viscosity

ρ	Density
σ	Stress
σ_B	Bending stress
ϕ	Velocity potential
ω	Under-relaxation factor
ω_i	Eigenfrequency
ω_n	Natural frequency

IX. ABREVIATIONS

BEM	Boundary Element Method
CFD	Computational Fluid Dynamics
DAF	Dynamic Amplification Factor
DFBI	Dynamic Fluid-Body Interaction
DNS	Direct Numerical Simulation
DNV	Det Norske Veritas
FD	Finite Differential
FE	Finite Element
FEM	Finite Element Method
FSI	Fluid-Structure Interaction
FV	Finite Volume
HAF	Hydroelastic Amplification Factor
NS	Navier-Stokes
ODB	Output Database
PSA	Petroleum Safety Authority Norway
RANSE	Reynolds Averaged Navier-Stokes Equation
SIMPLE	Semi-Implicit Method for Pressure Linked Equations
SPH	Smoothed Particle Hydrodynamics
SST	Shear Stress Transport
VOF	Volume Of Fluid

1. INTRODUCTION

1.1. General

Free-fall lifeboats have shown a rapid development since their commercial dawn in 1978. They have many obvious advantages over the traditional lowered lifeboats. They can be deployed faster, and due to their path through the water after impact, they will quickly reach a position and velocity suited for an effective retreat from the platform or ship.

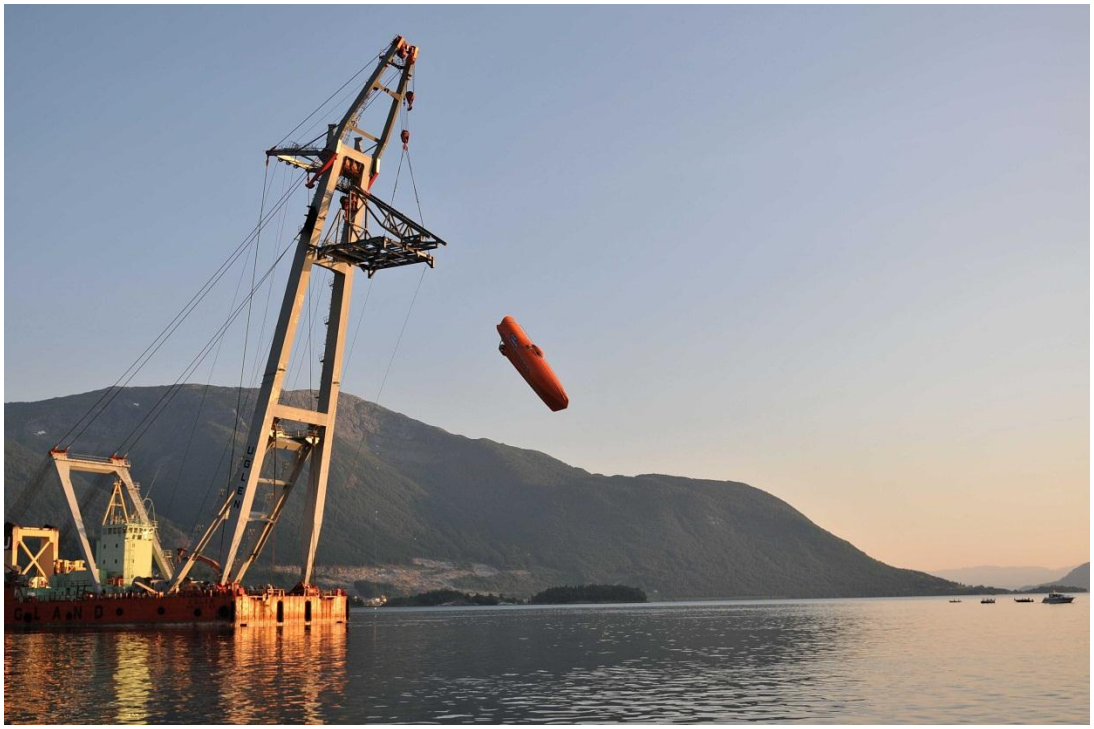

Figure 1 – Free-fall lifeboat during test drop. (http://themaritimeblog.com/, 2009)

In 2005 the Petroleum Safety Authority Norway (PSA) expressed concerns about the safety of the free-fall lifeboats in the Norwegian offshore industry. The reason for this was tests drops carried out at the platform Veslefrikk B, where damages were seen on the superstructure of the lifeboats (www.ptil.no, 2005). This led to investigations on the structural integrity of existing lifeboats, as well as a new DNV standard for free-fall lifeboats, the DNV-OS-E406.

In the aftermath of these events, the impact of free-fall lifeboats has been extensively studied, both numerically and through experiments. They are typically thin plated, composite hull structures. The high pressure peaks during slamming can lead to deformations in order of magnitude up to several times the plate thickness. This makes the numerical analysis of free-fall lifeboats complicated.

Conventional impact simulations assume that the hull remains rigid throughout the water entry. However, with large deformation, an interaction between hydrodynamic pressures and structural

deformations can be expected. This mutual dependency is called *hydroelasticity*. To analyze this, a proper fluid-structure interaction (FSI) analysis has to be carried out.

In this thesis, a two-way coupled simulation method for slamming analyses is presented. The method is compared to experimental data, and the necessity of a fully coupled FSI-analysis is parametrically investigated and discussed.

In chapter 1 previous work on slamming theory, numerical methods and experiments is presented.

In chapter 2 the theoretical background for the simulation method in this thesis is presented, and put into a perspective by comparison with other widely used methods on slamming simulations.

In chapter 3 the hydrodynamic model is described and verified with a comparison to previous work.

In chapter 4 the hydroelastic model is presented, and then compared to hydroelastic experiments for verification.

In chapter 5 a parametric study on the hydroelasticity phenomenon is conducted, and the necessity of a hydroelastic and structural nonlinearity is discussed.

In chapter 6 the method and results are discussed. Chapter 7 contains the conclusion, and chapter 8 presents recommendations for future work.

1.2. Previous work

The water entry problem has been studied by numerous scientists over the years. The earliest work commonly referred in literature is the work of von Karman (1929), where a potential theory solution to idealized cross sections is presented. His theory was later extended to account for the pile-up of water by Wagner (1932).

During the 20th century, scientists such as Dobrovol'skaya and Cointe have further developed the theory, and contributed to the refinement of the analytical solutions to the impact problem. With the introduction of modern computers and numerical methods, the impact problem has seen a renewed and rapid development.

Zhao and Faltinsen (1993) present a nonlinear boundary element method, capable of analyzing arbitrary cross sections. The slamming problem is analyzed satisfying the nonlinear free-surface boundary condition, maintaining conservation of mass, energy and momentum. This method was later extended to three-dimensional problems by Faltinsen and Chezhian (2005).

Methods based on solutions to the Navier-Stokes (NS)-equations have been developed. Particularly the smoothed particle hydrodynamics (SPH)-method and numerical solutions to the Reynolds Average Navier-Stokes (RANS)-equations have been extensively used (Faltinsen, 2000).

Different methods for FSI-simulations have been developed over the last 15 years. Korobkin et al. (2006) present a solution to the coupled equations for the impact of a wedge. A generalized Wagner theory is coupled with a finite element (FE)-solution for the structure. Lu et al. (2000) also present a nonlinear boundary element method for the water entry problem, and a finite element method is applied for the coupled, structural response. Solutions for different angles are presented, and it is emphasized that different hydroelastic behaviors will be of importance, depending on the impact angle.

Panciroli et al. (2013) present a fully coupled solution for a hydroelastic wedge entering water, by applying the SPH-method with an FE-code. The results are compared to experimental results, and show a reasonable agreement.

Piro and Maki (2011) solve the problem using a RANS-formulation of the water entry, coupled with an FE-code. The fully coupled analysis is compared to a one-way coupled analysis. A quasi-coupled analysis is presented, where structural effects on the pressure field are implicitly accounted for through artificial, acoustic cells emitting pressure waves on the fluid domain. This method shows excellent results, and has an advantage over a fully coupled analysis in that requirements to time steps and mesh size go down, and with it the computational cost.

Wang and Guedes Soares (2012) performed water entry experiments with large, 3-D wedges. Results are compared to a one-way coupled generalized Wagner method, where the pressure is mapped onto an FE-model of the structure.

In the above referred works, a considerable amount of work has been put in writing an appropriate coupling scheme. Lu et al. (2000) and Korobkin et al. (2006) develop entire codes for the FSI-problem. Piro and Maki (2011) use the freeware OpenFOAM and the commercial code Abaqus, coupled by developing a script for the coupling.

Such tailored methods are inflexible and inaccessible for non-specialized users. Easily accessible commercial codes for FSI-simulations are therefore sought. In this thesis, the built-in co-simulation engines in the CFD-code STAR CCM+ and the FEM-code Abaqus are used. The coupling schemes are fully integrated in both programs, and therefore easily accessible to the user.

1.3. An assessment of the structural integrity of a free-fall lifeboats

A structural integrity assessment of a free-fall lifeboat was conducted by Marintek (2006). The report from this work serves as a motivation for the numerical methods presented in this thesis.

The lifeboat hull consists of a multilayer composite. A 3-D FE-model was made, and nonlinear FE-analyses were performed. The FE-model was verified by comparison to an onshore, static experiment. The lifeboat was loaded with sandbags, and deformations were measured. The load case was reproduced in the FE-model, and a good agreement was found between experiment and model results.

Based on results from measurements and calculations, the water entry is divided into four phases. They are the *surface penetration phase, transient dynamic response phase, maximum submergence phase* and *surfacing phase.* A potential theory-based load model is established and calibrated by comparison to model and full scale tests. These loads are then applied to the FE-model. The responses during the transient dynamic response phase and particularly the maximum submergence phase are considered the most critical.

In the full scale test, deformations and pressures are measured on different locations on the hull. Figure 2 shows measurements of the maximum pressure at the stern of the lifeboat. For the given wave condition, a pronounced pressure oscillation is observed, with a dominating frequency of approximately 18 Hz. The oscillations are believed to be associated with the collapsing of the cavity created shortly after full submergence of the lifeboat. This phenomenon has not been thoroughly studied, but the oscillations of the pressure may indicate either the presence of trapped air or a hydroelastic response of the stern (Marintek, 2006).

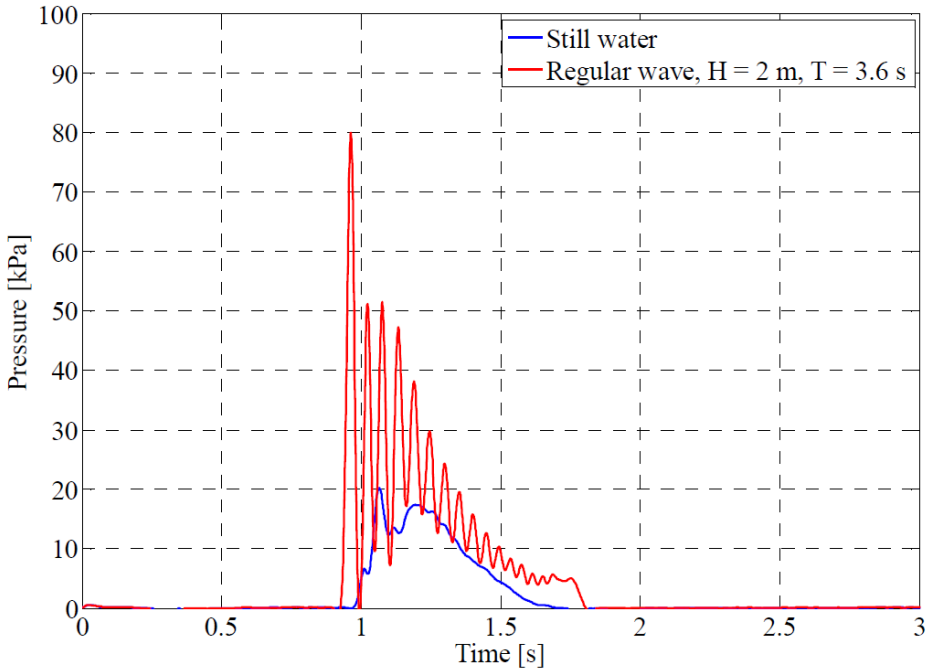

Figure 2 – Measured pressure at the stern of the lifeboat.

Figure 3 shows measured deformations from the experiment at different locations. Deformations are seen to be large in magnitude, with a highly oscillatory behavior. The high response oscillations are dominated by a frequency of approximately 5 Hz.

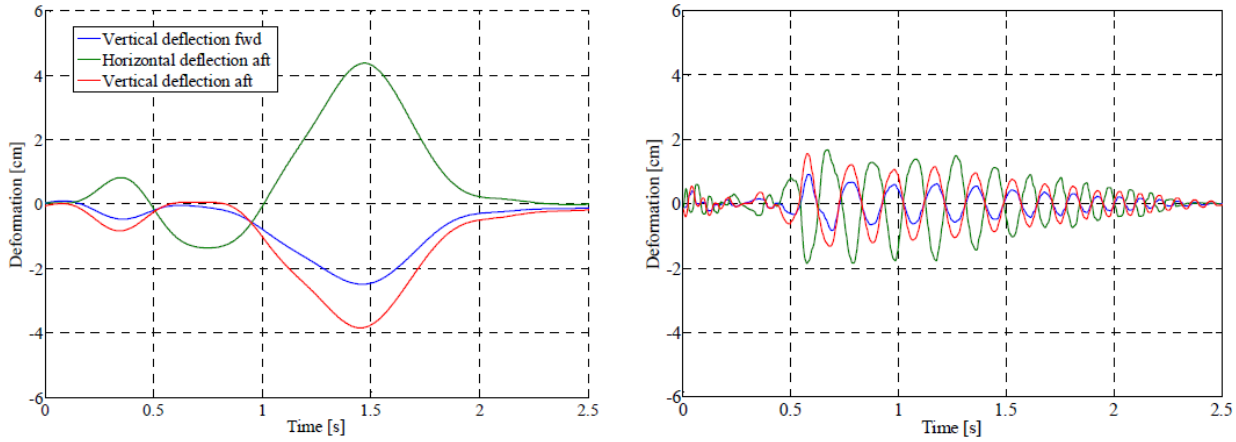

(a) Low-pass filtered (b) High-pass filtered

Figure 3 – Measured response at selected locations of the lifeboat.

The report concludes that the lifeboat does in fact lose its carrying capabilities for the greatest expected submergences, and as a consequence of these findings, design changes were proposed and implemented.

The large responses in the structure, oscillating at a relatively low frequency, would be better understood by conducting an FSI-analysis. The numerical methods used in the Marintek-report are based on the assumption that loads and responses can be assessed independently. However, for large responses, and in particular for oscillating responses, there is reason to believe that the loads and responses should display a mutual dependency, and the problem must be analyzed hydroelastically. For example, the oscillating frequencies found using the nonlinear FE-model are in fact seen to be in the region of 3 Hz, almost half the frequency seen in the measurements. It is concluded that this could be because the model fails to accurately account for changes in added mass.

The large deformations and oscillating pressure documented in the Marintek-report warrants a more thorough analysis. According to Faltinsen (2000), “Hydroelastic slamming must be hydrodynamically analyzed from a structural point of view”. This implies employing an FSI-analysis to the problem. The work presented in this thesis aims at finding a suitable method for such calculations.

2. THEORY

2.1. Water entry

2.1.1. Rigid wedge

A theoretical solution to the impact problem is presented in the following, using potential theory. Consider a two-dimensional, rigid wedge entering calm water with constant velocity, as shown in Figure 4 a).

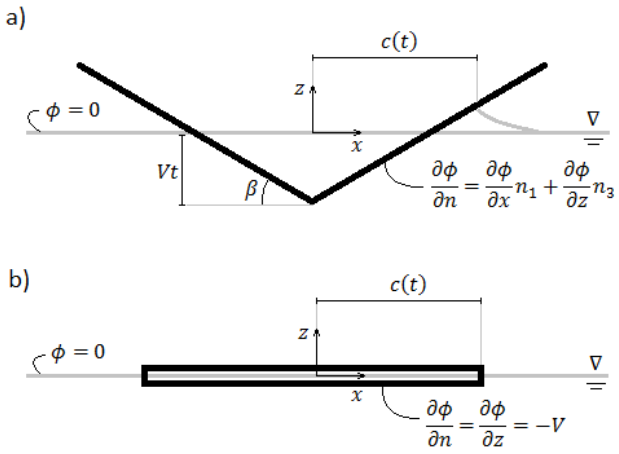

Figure 4 – Boundary value problem for the water impact of a wedge. a) – Original geometry. b) – equivalent plate geometry.

If an irrotational flow with constant density is assumed, there exists a velocity potential ϕ so that the velocity field can be written

$$\mathbf{v} = \nabla\phi \qquad \text{Eq. 2.1}$$

To find the velocity potential, an equivalent plate problem is considered, as seen in Figure 4 b). No gravity and a calm surface are assumed. The following boundary conditions are then valid

$$\phi = 0 \quad \text{for} \quad z = 0 \quad \text{and} \quad x > c(t)$$

$$\frac{\partial\phi}{\partial z} = -V \quad \text{for} \quad z = 0 \ \text{and} \quad -c(t) < x < c(t) \qquad \text{Eq. 2.2}$$

A solution to the boundary value problem is the velocity potential

$$\phi = -V\sqrt{c^2 - x^2} \qquad \text{Eq. 2.3}$$

The pressure is now found from the Bernouilli equation

$$p = -\rho\frac{\partial\phi}{\partial t} - \rho g z - \frac{\rho}{2}\mathbf{v}^2 \qquad \text{Eq. 2.4}$$

The slamming occurs over a short time interval, so that the hydrostatic term will be small. Also, the time gradients will dominate the spatial gradients during the impact. It is observed that

$$\mathbf{v}^2 = \left(\frac{\partial\phi}{\partial x}\right)^2 + \left(\frac{\partial\phi}{\partial z}\right)^2 \qquad \text{Eq. 2.5}$$

Therefore, the second order term may be neglected as well. The pressure may now be written

$$p = -\rho\frac{\partial\phi}{\partial t} = \rho V\frac{c}{\sqrt{c^2 - x^2}}\frac{\partial c}{\partial t} \qquad \text{Eq. 2.6}$$

It is difficult to find an analytical expression for the wetted length $c(t)$. Different approaches have been applied for different geometries. The expression proposed by Wagner (1932) is used in the following. Taking the pile-up of water into account, the wetted length is written

$$c = \frac{\pi V t}{2tan\beta} \qquad \text{Eq. 2.7}$$

The corresponding vertical force on the wedge can be found by integration

$$F_3 = \int_{-c}^{c} p dx = \rho V c\frac{\partial c}{\partial t}\int_{-c}^{c}\frac{dx}{\sqrt{c^2 - x^2}} = \frac{V}{2}\frac{\partial A_{33}}{\partial t} \qquad \text{Eq. 2.8}$$

where $A_{33} = \rho\pi c^2$ is the added mass of a flat plate in heave. A solution to the water entry problem is obtained. The pressure on the wedge bottom is often written as

$$p = \frac{1}{2}\rho C_p V_R^2 \qquad \text{Eq. 2.9}$$

where C_p is the pressure coefficient, and V_R is the effective impact velocity. This is a pragmatic approach that is easily calibrated by experimental results. C_p is dependent on position relative to the jet and the impact angle, as seen in Figure 5. It is seen that the pressure increases with increasing velocity and decreasing angle of impact.

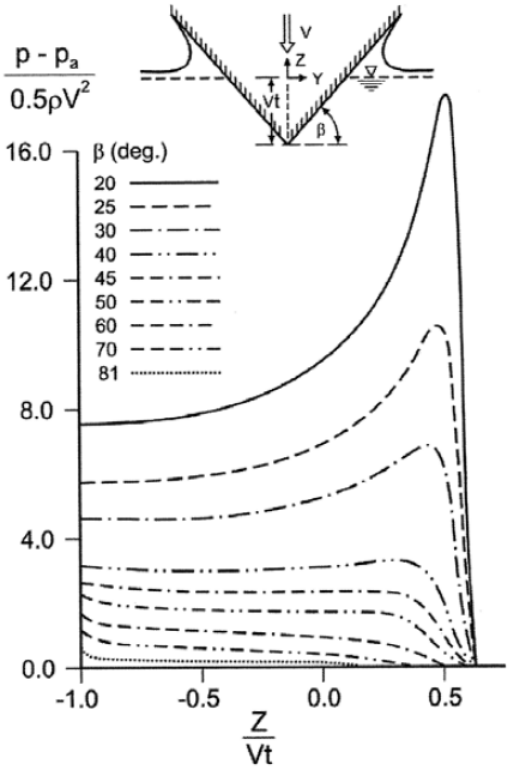

Figure 5 – Pressure coefficient distribution for different wedge angles entering water. (DNV, 2010)

The impact assessment described in DNV's recommended practices for environmental loads (DNV, 2010) are based on a potential theory approach. They have, however, been shown to be non-conservative for extreme load cases (Johannessen, 2012). Therefore it is of great importance to find better numerical approaches to assess the impact problem.

The theory outlined above is valid only for a wedge. For a different geometry, the wetted length $c(t)$ will display a different behavior. For an arbitrary geometry, there is no general, analytical expression that describes the wetted length. This puts every pressure estimate at the mercy of the validity of assumptions made when simplifying the geometry into a shape, for which analytical solutions apply. Alternatively, experimental values for C_p can be used, but they too will suffer from the fact that they are based on findings from idealized geometries. This problem has been addressed by several theorists, but will not be elaborated here.

2.1.2. Elastic wedge

Now consider the hydroelastic water entry of a wedge, see Figure 6.

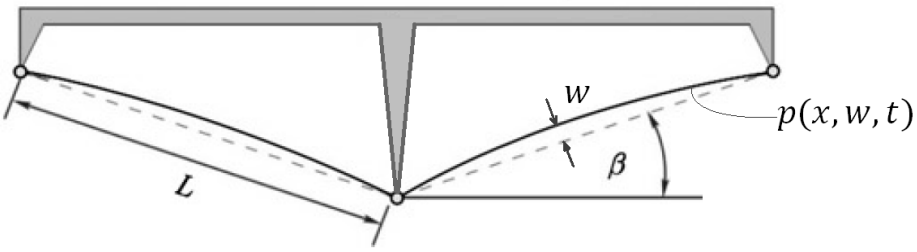

Figure 6 - Hydroelastic water entry of wedge.

The problem is still two-dimensional, with constant impact velocity. The difference from the rigid wedge is a mutual dependency between structural response and hydrodynamic load, i.e. $p = p(w)$. The hydroelastic equilibrium equation for the bottom of the wedge may be written

$$M\frac{\partial^2 w}{\partial t^2} + EI\frac{\partial^4 w}{\partial x^4} = p(x, w, t) \qquad \text{Eq. 2.10}$$

where M is the mass per unit length, w is the wedge deflection, EI is the structural stiffness and $p(x, w, t)$ is the slamming pressure. There exists no general solution to this equation. The coupled nature of the deformation and the pressure distribution makes any solution highly case dependent. Still, some simplified solutions do exist. A brief presentation of a solution for a single beam is found in the following, as described by Aarsnes (2012).

First, it is assumed that the deformation can be written as a linear sum of dry eigenmodes

$$w(x, t) = \sum_{i=1}^{N} q_i(t)\,\psi_i(x) \qquad \text{Eq. 2.11}$$

where $q_i(t)$ is the time dependent principal coordinate corresponding to $\psi_i(x, z)$. $\psi_i(x, z)$ is the i'th normal mode of the system. Inserting Eq. 2.11 into Eq. 2.10, and setting the external pressure load to zero, the dry eigenfrequencies of the beam may now be found by solving

$$-\omega_i^2 M\psi_i + EI\frac{\partial^4 \psi_i}{\partial x^4} = 0 \qquad \text{Eq. 2.12}$$

The eigenfrequencies are

$$\omega_i = \frac{C_{ii}}{M_{ii}} \qquad \text{Eq. 2.13}$$

where $M_{ii} = \int_{-\frac{L}{2}}^{\frac{L}{2}} M\,\psi_i^2(x)dx$ and $C_{ii} = \int_{-\frac{L}{2}}^{\frac{L}{2}} EI\,\frac{\partial^4\psi_i}{\partial x^4}\psi_i(x)dx$. M and EI may either be continuous functions, or FE-formulated, depending on the approach chosen. The fluid domain may also in this case be described by potential theory. The difference between this case and the rigid body wedge is that the boundary condition on the wedge bottom must account for the deformation of the beam. This can be expressed as

$$\frac{\partial\phi}{\partial z} = V(t) + \frac{\partial w}{\partial t} \quad \text{on} \quad z = 0 \qquad \text{Eq. 2.14}$$

Note that this is the same boundary condition as for the rigid wedge, except for the added velocity of the wedge deformation. We obtain the following velocity potential

$$\phi = \left(V(t) + \frac{\partial w(x,z,t)}{\partial t}\right)\sqrt{c^2 - x^2} \qquad \text{Eq. 2.15}$$

To arrive at a solution for **v** and $p(x,w,t)$ further simplifications have to be made. We assume constant velocity at impact. The slamming event is then divided into two phases. They are the *structural inertia phase*, where $t < t_1$, and the *free vibration phase*, where $t > t_1$, as seen in Figure 7.

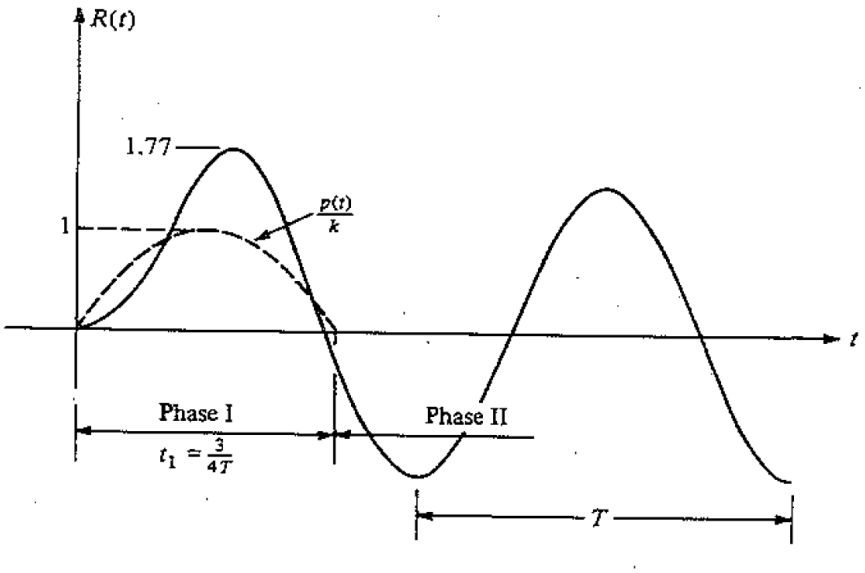

Figure 7 – The phases of impulse loading.

For the structural inertia phase it is assumed that the effect of the beam deformation on the pressure field can be expressed in terms of the mean deflection along the beam, i.e.

$$w(x,z,t) \approx \bar{w}(t) \quad \text{for} \quad t < t_1 \qquad \text{Eq. 2.16}$$

This allows for the use of the Wagner approach on the wetted length $c(t)$, reducing the problem to the familiar rigid wedge problem during the inertia phase. Furthermore, we assume that the structural inertia dominates structural stiffness during the inertia phase. Combining Eq. 2.6 with Eq. 2.10 we may now write

$$M\frac{\partial^2 w}{\partial t^2} = -\rho\frac{\partial \phi}{\partial t} \quad for \quad x < |c(t)| \quad on \quad z = 0 \qquad \text{Eq. 2.17}$$

$$M\frac{\partial^2 w}{\partial t^2} = 0 \quad for \quad x > |c(t)| \quad on \quad z = 0 \qquad \text{Eq. 2.18}$$

as boundary conditions for the velocity potential. This problem was solved by Faltinsen (1997), proposing the following initial conditions for the free vibration phase

$$\frac{\partial w(t = t_1)}{\partial t} = -V \qquad \text{Eq. 2.19}$$

$$w(x, t_1) \approx 0$$

Now the free vibration phase is considered. It was shown by Aarsnes (1994) that for a flat plate the deformation is dominated by the first eigenmode. Recalling that we now operate under the flat plate assumption, we may simplify Eq. 2.11 into

$$w(x, t) = q_1(t)\psi_1(x) \qquad \text{Eq. 2.20}$$

Aarsnes (2012) shows that the resulting pressure distribution p and bending stress distribution σ_B along the beam may be written as

$$p(x, t) = -\rho\frac{\partial \phi}{\partial t} = \frac{8\rho V\omega_{1,wet}}{\pi^2}\sin(\omega_{1,wet}t)\sqrt{(L/2)^2 - x^2} \qquad \text{Eq. 2.21}$$

$$\sigma_B = Ez_a\frac{4V}{\pi\omega_{1,wet}}\left(\frac{\pi}{\mathrm{L}}\right)^2\cos\left(\pi\frac{\mathrm{x}}{\mathrm{L}}\right)\sin(\omega_{1,wet}t) \qquad \text{Eq. 2.22}$$

with maximum values being

$$p_{max} = \frac{4\rho VL\omega_{1,wet}}{\pi^2} \qquad \text{Eq. 2.23}$$

$$\sigma_{B,max} = Ez_a\frac{4V}{\pi\omega_{1,wet}}\left(\frac{\pi}{\mathrm{L}}\right)^2 \qquad \text{Eq. 2.24}$$

Here, V is the impact velocity, $\omega_{1,wet}$ is the first wet eigenmode, L is the length of the beam, z_a is the height of the beam and E the Young's modulus of the beam. These expressions have shown reasonable agreement with experiments of flat plates during the initial phase, where the maximum stresses are measured (Aarsnes, 1994). Later, during the free vibration phase, they

become inaccurate. Note that $p \propto V$ and $\sigma_B \propto V$, as opposed to the rigid wedge theory, where the $p \propto V^2$. This is an important conclusion to draw from a hydroelastic analysis, implying a reduced pressure peak when including the beam elasticity.

This analysis has some questionable aspects. Assuming that $w(x,z,t) \approx \overline{w}(t)$ is fundamentally unphysical, but seems to be justifiable when compared to the experiments (Aarsnes, 1994). The analysis is based on the assumption that the wetting time is lower than the first eigenmode. For stiff steel and aluminum structures this would demand a low wetting time, suggesting very small angles and high impact velocities. On the other hand, it is assumed that the velocity is low enough to avoid effects of trapped air. This seemingly contradicting pair of base assumptions begs further investigation.

Furthermore, it is interesting that structural analysis is strictly linear. As was seen in Section 1.3, the deformations can be as large as the thickness in order of magnitude, suggesting that the effect of geometrical stiffness should be taken into account.

2.1.3. Linear and nonlinear geometry

In the previous section a hydroelastic beam was considered and a pressure distribution and stress distribution for the impact problem was proposed. The governing equation was formulated under the assumption that deformations would be small. For a thin, composite plate as the one used in the design of free-fall lifeboats, deformations have been shown to be in the same order of magnitude as the plate thickness. This implies that a nonlinear geometry should be considered. Expressions for equivalent static deformations are derived in the following.

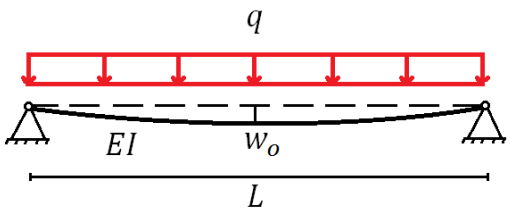

Figure 8 – Simply supported beam with small deformations.

The *small-deformation* assumption provides the following governing equation for a static case with an evenly distributed load,

$$EI\frac{\partial^4 w}{\partial x^4} = q \qquad \text{Eq. 2.25}$$

with the analytical solution

$$w_{max} = \frac{5}{384}\frac{qL^4}{EI} \qquad \text{Eq. 2.26}$$

The *large-deformation* assumption provides the following governing equation for a static case with an evenly distributed load

$$EI\frac{\partial^4 w}{\partial x^4} + P(w)\frac{\partial^2 w}{\partial x^2} + Mg\frac{\partial w}{\partial x} = q \qquad \text{Eq. 2.27}$$

The difference is that the axial force P(w) is included, as well as the static deformation due to the beam weight Mg. Note that the tension is dependent on the wedge deformation. This equation has no general analytical solution. A simplified solution is presented for later comparison. It is assumed that the static deformation due to the weight of the beam is negligible. Further, zero bending stiffness is assumed. This appears to be an unphysical assumption, but as will be seen in Chapter 5, the resulting response is in a reasonable region for very slender structures.

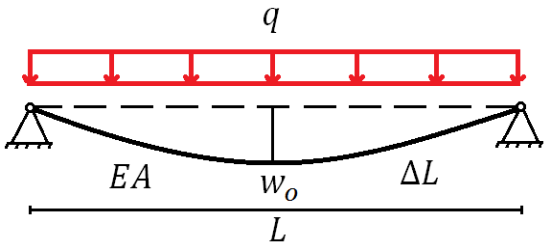

Figure 9 – Simply supported beam with large deformations.

The governing equation may now be written

$$P(w)\frac{\partial^2 w}{\partial x^2} = q \qquad \text{Eq. 2.28}$$

The approximation $w = w_{max}\sin\left(\frac{\pi x}{L}\right)$ is used for the wedge deformation. The deformation leads to an elongation ΔL of the wedge which can be calculated by numerically evaluating the integral equation for the arc-length

$$\Delta L = \int_0^L \sqrt{1 + \left(\frac{dw}{dx}\right)^2}\, dx - L \qquad \text{Eq. 2.29}$$

Now, the strain is defined as

$$\varepsilon = \frac{\Delta L}{L} \qquad \text{Eq. 2.30}$$

We apply Hooke's material law

$$\sigma = E\varepsilon \qquad \text{Eq. 2.31}$$

and use the axial stress definition

$$P = \sigma A. \qquad \text{Eq. 2.32}$$

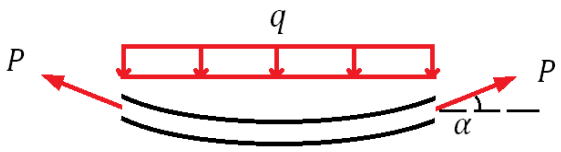

Figure 10 - Force equilibrium of a zero stiffness catenary.

An equilibrium consideration now gives the relationship between maximum deformation and line load q

$$2Psin(\alpha) = qL \qquad \text{Eq. 2.33}$$

The angle alpha is given as $\alpha = \frac{dw}{dx} = \frac{w_o \pi}{L}$ at the edges, which gives

$$q = 2EA\Delta Lsin\left(\frac{w_o \pi}{L}\right) \qquad \text{Eq. 2.34}$$

The importance of nonlinear effects will be analyzed in Chapter 4 and 5.

2.1.4. The importance of hydroelasticity

To evaluate whether or not hydroelasticity is of importance to a problem, a simple impulse consideration may be performed. For a sine load history, it is seen from Figure 7 that a load period of $t = 3/4T$ gives a *dynamic amplification factor* (DAF) of 1.77.

The hydroelasticity phenomenon has a similar range of relevance as a general impulse load. If the wetting time of the system is in the range of the lower eigenperiod, the system will respond as it does to impulse loads. If deformations in addition are large, there will be a mutual dependency between deformations and pressure field, and the problem will have to be addressed hydroelastically. The parameter of importance is therefore the *wetting time quotient*

$$WQ = \frac{t_1}{T_1} \qquad \text{Eq. 2.35}$$

Aarsnes (2012) suggests that hydroelasticity is important for a wedge shaped cross section when

$$\frac{tan\beta}{V\sqrt{\rho L^3/EI}} \leq 0.25 \qquad \text{Eq. 2.36}$$

Another approach is presented by Panciroli et al. (2012), where a hydroelasticity parameter R is proposed. It includes the deadrise angle β and impact velocity V, as well as the total system mass M and the lowest eigenfrequency of the system T. It is proposed that hydroelastic effects will be important when

$$R = \frac{tan\beta}{V}\frac{\sqrt{M}}{T} \in \langle 88{,}210 \rangle \qquad \text{Eq. 2.37}$$

The practical implication of the introduction of these parameters is that an arbitrary structure with little effort may be evaluated for hydroelasticity.

2.2. Computational fluid dynamics (CFD)

As was seen in Section 1.2, theoretical solutions to the water entry problem have been sought by many scientists over the years. The shortcomings of the theoretical approaches to describe the slamming problem have been their lacking ability to accurately describe complex geometries and 3-D effects, or more exotic phenomena such as hydroelasticity, cavitation and ventilation. Therefore, experiments and numerical methods have been designed to address the problem. The numerical methods for solving hydrodynamic problems are referred to as *computational fluid dynamics (*CFD).

There are many examples of rigid-body impact experiments in the literature, for example the ones presented by Tveitnes et al. (2008). Fewer attempts have been made to investigate the hydroelastic slamming of wedge-shaped bodies. Notable in the literature studied for this thesis, is the experiment series conducted by Panciroli et al. (2013). In Chapter 4 this series of experiments will be described and compared to results of the numerical model used in this thesis.

There are different numerical methods for analyzing the water entry problem numerically. In this thesis, the RANS-equations will be used. A brief description of other methods is included in the following.

Boundary element methods (BEM) have frequently been applied to study ships and offshore structures, including the impact problem. They are potential theory-based methods, with low computational costs compared to numerical solutions of the NS-equation.

In recent years, *Smoothed Particle Hydrodynamics* (SPH) has increasingly been employed for free surface simulations. It is based on representing the fluid continuum by a finite number of mesh free, discrete particles. Physical quantities such as pressure and velocities are assigned to each particle. They are then calculated as a smoothed average between the neighboring particles. The method has some advantages over the control volume-based numerical solutions to the NS-equation.

SPH by definition ensures conservation of mass, as the mass is initially distributed to the particles. The pressure field is described as a smoothed average between neighboring cells, needing significantly lower computational time than the methods employed in the mesh-based CFD. Finally, SPH displays excellent rendering of the free surface. If air is neglected, the surface is easily and implicitly described as the mere end of the particle region governed by gravity. A limitation to the method is the high number of particles needed to describe the domain, as particle size must be constant over the region. It has difficulties fulfilling the incompressibility property

of water. Finally, the high accuracy needed in boundary regions is also better described with regular, grid-based NS-solvers.

Nevertheless, the method is increasingly being used for flood simulations, and for marine applications involving complex free-surface geometries, such as slamming events.

CFD is a rapidly growing field, with new methods being developed continuously as computational power increases. The method used in this thesis is based on solving the (NS)-equation and the continuity equation, which together describe the conservation of impulse, mass and energy of an arbitrary fluid flow. There is no general solution to these equations, so depending on the case under consideration a numerical approach must be applied to analyze the problem. The theory and numerical approach used in these analyses are described in the following. The reader is encouraged to study the work of Ferziger and Peric (2011) and the online documentation presented by CD-ADAPCO (2012) and for further elaborations, as they constitute the basis for the theoretical descriptions.

2.2.1. Mathematical model

The continuity equation and the NS-equation can be written on differential form as

$$\frac{\partial \rho}{\partial t} + \nabla(\rho \mathbf{v}) = 0 \qquad \text{Eq. 2.38}$$

$$\frac{\partial \mathbf{v}}{\partial t} + \mathbf{v} \cdot \nabla \mathbf{v} = \frac{1}{\rho} \nabla p + \mu \nabla^2 \mathbf{v} + \rho \boldsymbol{f} \qquad \text{Eq. 2.39}$$

where ρ is the density of water, $\mathbf{v}$ is the velocity vector, p is the pressure, μ is the dynamic viscosity and $\boldsymbol{f}$ denotes volume forces (gravity). They may also be written on integral form on a given volume V with a surface S

$$\frac{\partial}{\partial t} \iiint_V \rho \, dV + \iint_S \rho \mathrm{v_i} \, dS = 0 \qquad \text{Eq. 2.40}$$

$$\underbrace{\frac{\partial}{\partial t} \iiint_V \rho \mathrm{v_i} \, dV}_{Unsteady} + \underbrace{\iint_S \rho \mathrm{v_i} (\mathbf{v} \cdot \mathbf{n}) \, dS}_{Convection} = \underbrace{-\iint_S p(\mathbf{i} \cdot \mathbf{n}) dS}_{Pressure} + \underbrace{\iint_S \mu(\nabla \mathrm{v_i} \cdot \mathbf{n}) dS}_{Diffusion} + \underbrace{\iiint_V \rho q_i dV}_{Body\ forces} \qquad \text{Eq. 2.41}$$

where $\mathrm{v_i}$ is the velocity component in i-direction, q_i is the body forces in i-direction, and $\mathbf{n}$ is the unit vector normal to the surface. The terms are described for later references. Solving these

equations requires a numerical approach, and both the pressure term and the diffusion term make the NS-equation particularly hard to solve.

2.2.2. Discretization

In order to solve the given set of equations, a numerical approach is necessary. Therefore, it is necessary to discretize the equations to algebraic expressions that can be solved throughout the domain. There are some fundamentally different approaches, and they will be described briefly.

The *finite differential* (FD)-method solves the equations in their differential form on a chosen set of grid points. The method is practical and efficient, but has some limitations. It is only applicable on relatively simple geometries, and is not necessarily conservative.

The *finite volume* (FV)-method solves the equations in their integral form on a chosen set of control volumes. The volumes may have arbitrary shapes. As the convection term and the diffusion term of the NS-equation are solved as surface integrals on the interfaces between control volumes, the method per definition is conservative. This method is by far the most used in RANSE-formulations, and is also applied in the commercial code used in this thesis.

The *finite element method* (FEM) is similar to the finite volume method. It too, discretizes the domain in finite volumes, but the values are given in the element corners, unlike the finite volume method. The physical equations are multiplied with weight functions, as a means to properly describe the distributions across the element. The weight functions are defined so that each assumes a value of either zero or one at each element node, allowing continuous fields to be described as linear sums of the weighted functions. This method is well suited for solid mechanics, but for CFD, this method also has problems describing complex geometries. The method is used in the structural solver, and is elaborated in Section 2.3.

2.2.3. Mesh

The FV-method is the basis for the solver used in this thesis. In general, the governing equations are discretized over a grid of cells, with nodal values of the physics fields at the center of each cell, see Figure 11.

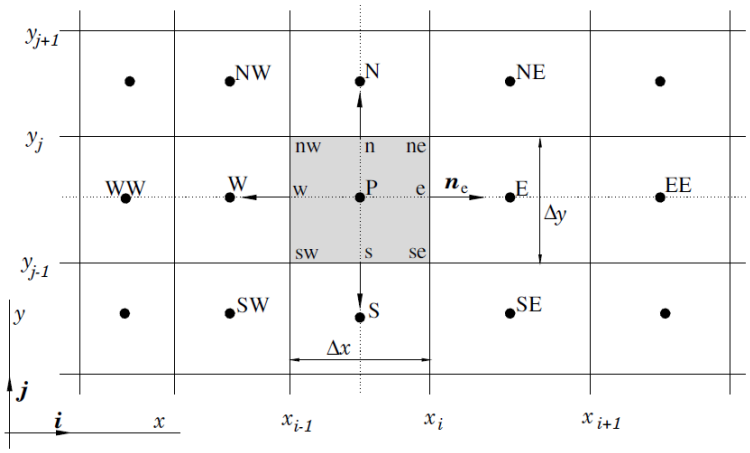

Figure 11 – Principle sketch over the trimmer mesh setup. (Ferziger and Peric, 2011)

The grid must not necessarily have a quadratic or even a perpendicular setup. In fact, a wide range of different grid propositions is used, each with advantages and disadvantages. Examples are the general *polyhedral* mesh, and the *tetrahedral* mesh. For the simulations run in this thesis, a grid is built up by *hexahedral* cells that are a 3-D equivalent of the setup seen above. This leads to a very effective solution, and is particularly well suited for free surface problems.

The mesh should be tailored to ensure an effective, but convergent solution for a given problem. The requirements to the mesh will be different at different locations in the fluid domain. Generally, areas with high gradients or high fluid velocities will require a finer mesh than areas with low gradients and low velocities. The Courant number requirement (see Section 2.2.12) should be satisfied. For turbulent fluid flows the requirement to the y+ value must also be considered (see Section 2.2.6). At the impact surface of a body entering water, high pressure gradients and large fluid velocities are expected. Therefore, a fine mesh is required.

In STAR CCM+, the mesh can be locally refined by applying a *volumetric control*. Regions are defined, for which the mesh setting may be set individually. This allows for a tailored mesh with the proper grid size in the entire region.

When modeling a moving object, additional challenges arise, related to the motion of the body entering water. The need for a fine mesh along the surface of the body makes a fixed mesh very ineffective, as it would require a fine mesh on a relatively large region. This can be coped with in different ways.

One possibility is the *overset* mesh technique, combined with a *dynamic fluid-body interaction* (DFBI)-model. The DFBI model calculates the trajectory of a rigid body, based on the mass distribution of the body and the pressure field in the fluid. A local overset mesh follows the object, and nodal values are interpolated between the background mesh and the moving mesh. This method is widely used in analyses of 6-*degree-of-freedom* (DOF) bodies.

If a constant velocity impact is assumed, a simpler approach can be used. The mesh can be given a constant global velocity equal to the impact velocity. This means that the entire mesh moves parallel to the body, and ensures high refinement on the required areas. Alternatively, the mesh and the object itself can be fixed at the initial location, with a free surface moving upwards towards the object. This will be done in the simulations in this thesis. Given the right boundary conditions, these two approaches are identical, and both allow for a more efficient mesh than the DFBI model.

2.2.4. Finite approximations

Surface integrals are generally discretized as

$$\iint_S f\, dS = \sum_k \iint_{S_k} f dS \qquad \text{Eq. 2.42}$$

where S_k is the k'th side of a control volume, and f is the function for either the convection or diffusion term. f can be expressed on the given surface as a linear combination of surrounding nodal values. In its simplest form the surface integral may be written

$$\iint_{S_k} f dS = f_k S_k \qquad \text{Eq. 2.43}$$

Similarly, volume integrals are generally discretized

$$\iiint_V g dV = g\Delta V \qquad \text{Eq. 2.44}$$

where g is the function for either the unsteady term or the body force term. ΔV is the volume of the cell.

These are just the fundamentals of discretizing the different terms, and more sophisticated methods can be used better to fit the chosen mesh, or to achieve a shorter solution time.

2.2.5. Pressure correction

There is no independent equation describing the pressure and its gradients. The pressure term must be solved iteratively and simultaneously with the velocity field. The approach is called *pressure correction,* and it iteratively corrects the pressure field so that the continuity equation is satisfied within each time step. By inserting the NS-equation in the continuity equation and assuming constant viscosity and density the following equation for the pressure is obtained

$$\frac{\partial}{\partial x_i}\left(\frac{\partial p}{\partial x_i}\right) = \frac{\partial}{\partial x_i}\left(\frac{\partial \rho u_i u_j}{\partial x_j}\right) p_{t-1} \qquad \text{Eq. 2.45}$$

Note that Einstein notation has been used. The method is now based on iteratively repeating two steps:

1. Use the old pressures p_{t-1} and velocity field $\mathbf{v}_{t-1}$ to calculate a temporary velocity field $\mathbf{v}^*$.
2. Use the velocity field $\mathbf{v}^*$ to calculate a pressure correction term p'.
3. Update the pressure field using the equation

$$p^{n+1} = p^n + \omega p' \qquad \text{Eq. 2.46}$$

where ω is an under-relaxation factor dictating the degree of field update between iterations. A high under-relaxation factor needs fewer iterations before converging and is suited for unsteady simulations. A low under-relaxation factor needs more iterations before converging, and is best suited for steady state problems, or initialization of an unsteady problem. This iteration process is repeated with the updated fields $\mathbf{v}^*$ and p^* until both the NS- and the continuity equation are satisfied. The convergence rate may be increased by introducing more complex iteration processes for the pressure. As the basic principles remain the same, these will not be elaborated. The process used in STAR CCM+ is called the SIMPLE-algorithm, and can be seen in APPENDIX D.

2.2.6. Turbulence

The diffusion term carries the information about viscosity and turbulence. The optimal description of turbulence would be through *Direct Numerical Simulation* (DNS), which solves the term directly. This is extremely costly, due to requirements to the mesh and time step needed to ensure convergence. DNS can only be used on smaller problems today, and is not well suited for commercial purposes. Therefore, numerous simplified models have been developed to provide a practical compromise between efficiency and accuracy. The one used in this thesis is called the k-ε model.

By expressing the velocities in the NS-equation as a linear combination of arithmetic means and standard deviations, the flow in i-direction may be written

$$u_i = \overline{u_i} + u_i' \qquad \text{Eq. 2.47}$$

where u_i' is a stochastic representation of the turbulence associated velocity. By applying this expression on the NS-equation, the *Reynolds Averaged Navier-Stokes* (RANS)-equation is obtained

$$\frac{\partial(\rho\bar{u}_i)}{\partial t} + \frac{\partial}{\partial x_j}\left(\rho\bar{u}_i\bar{u}_j + \rho\overline{u_i'u_i'}\right) = -\frac{\partial \bar{p}}{\partial x_i} + \mu\left(\frac{\partial \bar{u}_i}{\partial x_j} + \frac{\partial \bar{u}_j}{\partial x_i}\right) + \rho \boldsymbol{f} \qquad \text{Eq. 2.48}$$

As can be seen, additional unknowns have been introduced. They are handled by introducing two new expressions. The kinetic turbulent energy

$$k = \frac{1}{2}\left(\overline{u_i' u_i'}\right) \qquad \text{Eq. 2.49}$$

And the turbulent energy dissipation

$$\varepsilon = \frac{k^{\frac{3}{2}}}{L} \qquad \text{Eq. 2.50}$$

where L is a characteristic length associated with the highest kinetic turbulent energy. k and ε must be described by introducing equations of conservation for both. As they are rather complex, they have been left out. The turbulence is now stochastically accounted for, and this model describes the flow in the entire fluid domain.

However, at wall-boundaries the k-ε-model fails to describe the turbulent velocity gradients properly. To cope with this, the inner boundary layer is described by a *Shear stress transport* (SST)-model. A region at a given distance to the wall, often denoted by the dimensionless y+ value, is described by a *two-equation eddy-viscosity* model, but this will not be elaborated here. The combination gives an SST k-ε-model that is both robust and efficient, and widely used in turbulent flow simulations (Ferziger and Peric, 2011).

2.2.7. Free surface

For marine applications it is necessary to describe the free surface accurately. A free surface implies two fluid phases, air and water, with different material properties. Methods developed to account for this are generally divided into two groups, *surface tracing* and *surface capturing*.

In surface tracing techniques the domain is divided into two subdomains, where the interphase is traced and the mesh regenerated for both fluid phases at every time step. This leads to a great increase in computation time. Besides, these techniques are not well suited to describe complex surface geometries.

The surface capturing techniques imply that the free surface is captured by the initial mesh, demanding a mesh refinement at the free surface. One such method is called the *Volume-of-Fluid* (VOF)-method. In the literature on impact problems, the VOF-method is widely used to describe the two phases, as it effectively describes waves of arbitrary geometry, without having to update the mesh for every time step. The VOF-method introduces a volume fraction of fluid α to the problem, defined as

$$\alpha = \begin{cases} 1 & \text{for water} \\ 0 & \text{for air} \end{cases} \qquad \text{Eq. 2.51}$$

This pragmatic solution allows us to define the material quantities such as density and viscosity as continuous functions across the computational domain. By doing so, the two phases are in fact described as one, and the computational time is thus significantly reduced.

$$\rho = \alpha\rho_{water} + (1-\alpha)\rho_{air}$$
$$\mu = \alpha\mu_{water} + (1-\alpha)\mu_{air} \quad \text{Eq. 2.52}$$

The cost of this approach is the introduction of a new equation of conservation for α that must be solved for each time step.

$$\frac{\partial \alpha}{\partial t} + \nabla(\alpha \mathbf{v}) = 0 \quad \text{Eq. 2.53}$$

2.2.8. Compressibility

The introduction of compressibility of water is an effective way of reducing instabilities for the FSI-simulations run in this thesis. This can be done by introducing compressibility as it appears in physics, or by setting an artificial compressibility that still ensures a tolerable convergence level.

Defining the speed of sound c, the pressure dependency of the density is expressed as

$$\frac{\partial \rho}{\partial p} = \frac{1}{c^2} \quad \text{Eq. 2.54}$$

The density is now defined as

$$\rho = \rho_0 + \frac{p}{c^2} \quad \text{Eq. 2.55}$$

2.2.9. Solution process

When a mesh is chosen, the governing equations can be discretized into an algebraic equation set. Generally, this will take the form

$$A_P \phi_P + \sum_{nb} A_{nb} \phi_{nb} = Q_P \quad \text{Eq. 2.56}$$

A is a matrix that implicitly contains discretized information about the geometry and physics, ϕ is the relevant variable (for example a velocity component), and Q contains all terms that can be considered constant. P refers to the discretization point considered, and nb refers to all the neighboring points. The entire field is analyzed from this equation, so an appropriate combination of the terms for this equation must be found. For a steady state flow, or within a time step, the iterative solution for a velocity component ϕ is

$$\phi_P^{n+1} = \omega \frac{Q_P - \sum_{nb} A_{nb} \phi_{nb}^n}{A_P} + (1 - \omega)\phi_P^n \qquad \text{Eq. 2.57}$$

where n refers to the number of inner iterations and ω is the under-relaxation factor dictating the degree of field update between iterations, as for the pressure correction.

All field variables are updated by iteratively solving these equations. These iterations are referred to as *inner iterations*. The exception is the pressure term, which is solved by pressure correction after a full set of inner iterations. These iterations are referred to as *outer iterations*. Finally, for unsteady problems, results from a given time step is used as the initial conditions for a new set of inner and outer iterations for the new time step.

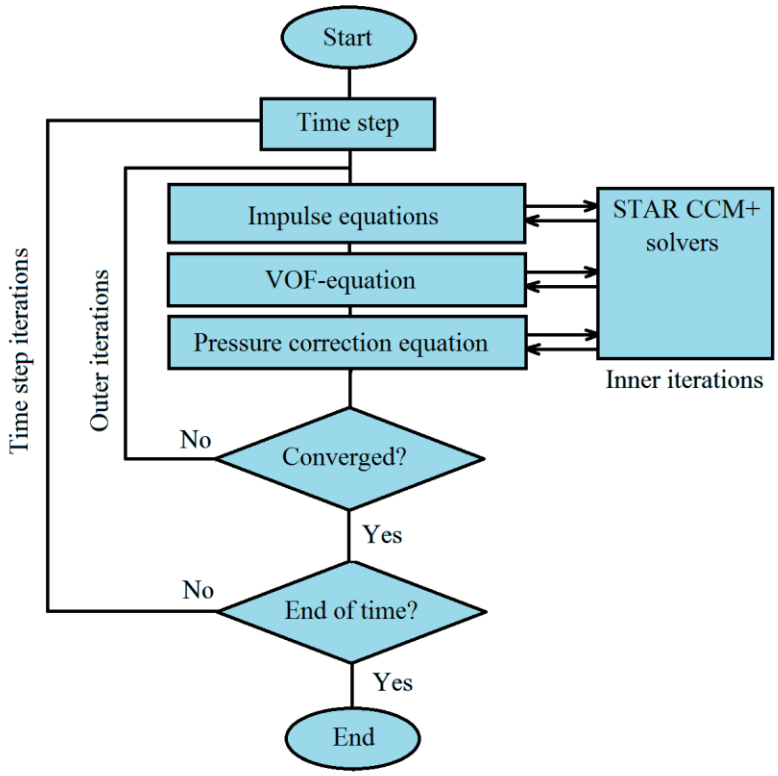

Figure 12 – Flowchart of the CFD process.

The time steps can be discretized in many ways. Explicit and implicit schemes are available, with 1st and 2nd order discretization being the most common ones, and the ones available in STAR CCM+ by default. Explicit schemes are less stable than implicit schemes, but the stability comes at the cost of computation time. We will not go into detail on the unsteady solver in STAR CCM+ here.

2.2.10. Simplifications

If an inviscid fluid flow with constant density and zero gravity is assumed, the following simplified equations is obtained

$$\nabla \mathbf{v} = 0 \qquad \text{Eq. 2.58}$$

$$\frac{\partial \mathbf{v}}{\partial t} + \mathbf{v} \cdot \nabla \mathbf{v} = \frac{1}{\rho} \nabla p \qquad \text{Eq. 2.59}$$

Note that the NS-equation is now reduced to the so-called Euler equation. This simplification allows us to approach the NS-equation directly, without having to modify it to the RANS-equation. The reason for this is that the viscosity is neglected, implying a turbulence-free fluid flow. The RANS-equation is a stochastic means to handle the delicate nature of turbulence, and the original equations may therefore be solved in their original state. This greatly simplifies the numerical approach needed. For the potential theory based solutions presented in Section 2.1.1, this assumption has been made, and results agree well with experiments. In Chapter 3 the validity of these assumptions will be discussed in detail.

2.2.11. Properties of the numerical approach

The quality of any given numerical model will depend on its ability to satisfy the following criteria:

1. *Consistency* – The equations of the numerical model should converge to the governing equations, as time-steps and grid size go to zero.
2. *Boundedness* – Values should remain in their domain. For example, concentrations should lie between 0 and 1, and cell volumes should remain positive.
3. *Stability* – Numerical errors should not propagate. This ensures boundedness, and also ensures convergence for iterative processes.
4. *Convergence* – The solution to the numerical model should converge to the solution of the governing equations, as time steps and grid size go to zero. This can be difficult to check, and experiments are often the only approach. It should be noted that the convergence term is widely used in numerical modeling, and the parameters under consideration must always be stated when convergence tests are done, to avoid confusion.
5. *Conservativeness* – Conservation of quantities defined by the conservation equations stated in the mathematical model must be satisfied. By applying a FV-method, this is satisfied by definition.
6. *Accuracy* – The model should be accurate within a tolerable limit. Some errors will inevitably occur. *Model errors* are errors associated with the difference between reality and the exact solution to the governing equations chosen. *Discretization errors* are the errors associated with the difference between the exact solution to the numerical model and the exact solution to the governing equations. *Iteration errors* are errors associated with the difference between the iterative solution to the algebraic equations and exact

solutions to the algebraic equations. Model errors may be particularly difficult to assess. It is nevertheless important that one remains aware of them.

2.2.12. Convergence

To ensure that a correct solution has been reached, convergence tests should always be performed. Generally, it is recommended to reduce time steps and cell size gradually until velocities and pressures converge. More specifically, the following values should be tested:

1. Physical models included
2. Domain size
3. Grid size
4. Time step
5. Inner and outer iterations
6. Finite approximations
7. Under-relaxation factors

For a solution of the RANS-equation in the time domain, caution must be observed when discretizing the domain. If the cells are too small compared with the time step, numerical smearing and energy dissipation may occur, leading to instability and in some cases divergence (Ferziger and Peric, 2011). The problem arises when the fluid crosses more than one cell between two time steps, as illustrated in Figure 13.

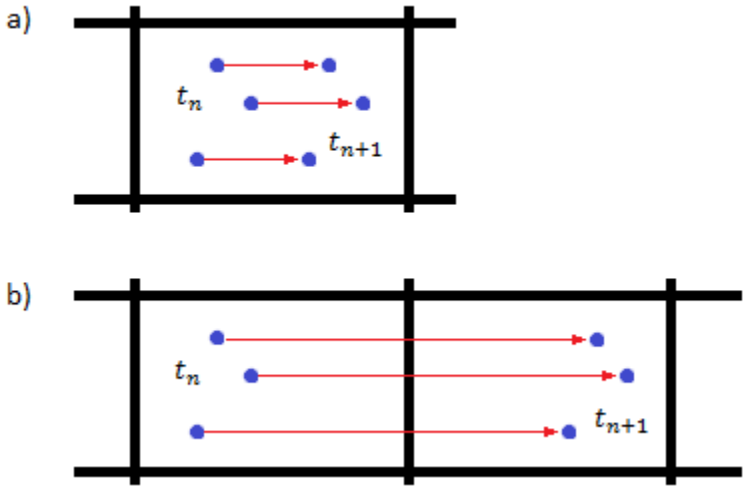

Figure 13 – Visualization of the importance of Courant number. a) Acceptable convection b) Unacceptable convection.

To avoid this, a match between fluid velocity, cell size and time step is needed to ensure convergence. By introducing the Courant number C_r this problem can be assessed quantitatively, by imposing the following demand to the discretization

$$C_r = V\frac{\Delta t}{\Delta x} \leq 1 \qquad \text{Eq. 2.60}$$

where V is the fluid velocity, Δt is the time step and Δx is the characteristic cell length. If an implicit solution method is chosen instead of the explicit one, the convergence tends to be more robust, and C_r values above 1 can be chosen, if convergence is otherwise demonstrated.

A correct combination of discretization methods, under-relaxation factors and iterations is also imperative to ensure convergence. Some discretization methods are unconditionally stable. Others are stable only for a given set of conditions. The appropriate combinations are best found from experience. Recommendations are found in the online documentations of STAR CCM+, CD-ADAPCO (2012).

2.3. Finite element method (FEM)

The structural part of the problem will be solved using the finite element method. The theory is based on the work presented by Moan (2003), Moan (2012) and the online documentation for Abaqus, Dassault-Systèmes (2013).

2.3.1. Static

For a shell element approach the structural domain is discretized into a finite number of 8-node shell elements with 5 DOFs per node (S8R5-elements). For a solid element approach the structural domain is discretized into a finite number of 8 node solid elements with 3 DOFs per node (C3D8R-elements).

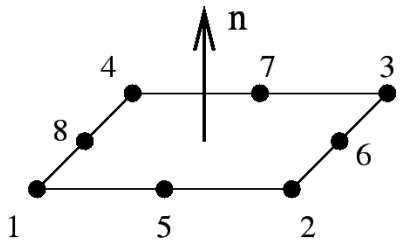

Figure 14 – Eight node shell element.

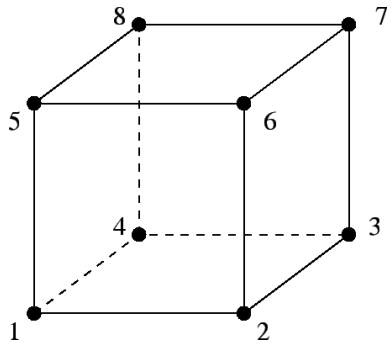

Figure 15 – Eight node solid element.

The deformation field is made continuous through interpolation functions between the nodes. Each DOF corresponds to an entry in the global deformation matrix $\boldsymbol{r}$ defined as

$$\boldsymbol{r} = \begin{bmatrix} r_1 \\ r_2 \\ \dots \\ r_n \end{bmatrix} \quad \text{Eq. 2.61}$$

where n is the number of DOFs in the system. The basis for the analysis is the FE-formulation of the equation of equilibrium

$$\boldsymbol{K}\boldsymbol{r} = \boldsymbol{R} \quad \text{Eq. 2.62}$$

where $\boldsymbol{K}$ is the global stiffness matrix, and $\boldsymbol{R}$ is the global load vector.

2.3.2. Dynamic

For the dynamic case, inertia, damping and time dependency of the deformation must be described. The deformations are time dependent, i.e.

$$\boldsymbol{r}(t) = \begin{bmatrix} r_1(t) \\ r_2(t) \\ \dots \\ r_n(t) \end{bmatrix} \quad \text{Eq. 2.63}$$

The basis for the analysis is the FE-formulation of the dynamic equation of equilibrium

$$\boldsymbol{M}\ddot{\boldsymbol{r}}(t) + \boldsymbol{C}\dot{\boldsymbol{r}}(t) + \boldsymbol{K}\boldsymbol{r}(t) = \boldsymbol{R}(t) \quad \text{Eq. 2.64}$$

where $\boldsymbol{M}$ is the global mass matrix and $\boldsymbol{C}$ is the global damping matrix. The resulting system is a set of linear equations with n degrees of freedom. The system is solved by using the *direct integration method.* There are different formulations of direct integration methods for finite elements, but they are all based on integrating the load vector over the system nodes, and expressing $\ddot{\boldsymbol{r}}$ and $\dot{\boldsymbol{r}}$ as finite differential approximations of $\boldsymbol{r}$. A slightly modified Newmark's β-family method is used in this analysis. At the time t_{k+1} the acceleration and velocity may be approximated as

$$\ddot{\boldsymbol{r}}_{k+1} = \frac{1}{\beta h^2}\,\boldsymbol{r}_{k+1} - \boldsymbol{a}_k$$
$$\dot{\boldsymbol{r}}_{k+1} = \frac{\lambda}{\beta h}\boldsymbol{r}_{k+1} - \boldsymbol{b}_k \quad \text{Eq. 2.65}$$

where β and λ are constants defining the nature of the approximations, h is the time increment, and $\boldsymbol{a}_k$ and $\boldsymbol{b}_k$ are calculated from the previous time step as

$$\boldsymbol{a}_k = \frac{1}{\beta \Delta t^2}\,\boldsymbol{r}_k + \frac{1}{\beta \Delta t}\dot{\boldsymbol{r}}_k + \left(\frac{1}{2\beta} - 1\right)\ddot{\boldsymbol{r}}_k$$

$$\boldsymbol{b}_k = \frac{\lambda}{\beta \Delta t}\,\boldsymbol{r}_k + \left(\frac{\lambda}{\beta} - 1\right)\dot{\boldsymbol{r}}_k + \left(\frac{\lambda}{2\beta} - 1\right)\ddot{\boldsymbol{r}}_k \qquad \text{Eq. 2.66}$$

where Δt is the time increment. By inserting Eq. 2.65 into Eq. 2.64 the equations can be solved for $\boldsymbol{r}$. Then $\dot{\boldsymbol{r}}$ and $\ddot{\boldsymbol{r}}$ are found from Eq. 2.65. This procedure is repeated for every time step. The method is either conditionally or unconditionally stable, depending on the values chosen for β and λ.

Generally, the time steps must be sufficiently small to capture the impulse period as well as the excited response periods. Typically, Δt is set to maximum $T_p/15$ or $T_n/15$, where T_p is the impulse period and T_n is the lowest relevant eigenmode of the system. In our case, the impulse period is the time for full submergence neglecting pileup. Abaqus will determine the needed time increment, depending on the loading.

2.3.3. Eigenvalue problem

To evaluate the eigenfrequencies of a system, the eigenvalue problem must be solved. By assuming zero damping the dynamic equilibrium equation may be written

$$\boldsymbol{M}\ddot{\boldsymbol{r}}(t) + \boldsymbol{K}\boldsymbol{r}(t) = \boldsymbol{R}(t) \qquad \text{Eq. 2.67}$$

It is assumed that the deformations can be written as a linear combination of weighted contributions from different eigenmodes, i.e.

$$\ddot{\boldsymbol{r}}(t) = \sum_{i}^{n} \boldsymbol{\varphi_i}\, y_i(t) = \boldsymbol{\varphi y} \qquad \text{Eq. 2.68}$$

where n is the number of eigenmodes included in the system. By inserting Eq. 2.68 into Eq. 2.67 the following eigenvalue problem is obtained

$$(\boldsymbol{K} - \omega_i^2 \boldsymbol{M})\boldsymbol{\varphi} = \boldsymbol{0} \qquad \text{Eq. 2.69}$$

where ω_i are the natural frequencies of the system. This equation is solved by using the Lanczos algorithm (Dassault-Systèmes, 2013). However, this will not be described in detail here.

2.3.4. Nonlinear geometry

In FEM, it is possible to account for large deformations. In its simplest form, the finite element formulations apply a constant stiffness matrix with loads applied to the undeformed geometry. If deformations become sufficiently large, both the stiffness and the load appliance will vary with the deformations. This is accounted for by applying a geometrical nonlinear finite element formulation.

The stiffness is now expressed as a combination of linear and nonlinear contributions, i.e.

$$\boldsymbol{K}(\boldsymbol{r}) = \boldsymbol{K_o} + \boldsymbol{K_\sigma}(\boldsymbol{r}) \qquad \text{Eq. 2.70}$$

where $\boldsymbol{K_o}$ refers to the small deformation stiffness matrix and $\boldsymbol{K_\sigma}(\boldsymbol{r})$ refers to the nonlinear contributions. The global finite element equilibrium equation is now written as a finite differential equation

$$\boldsymbol{K}(\boldsymbol{r})d\boldsymbol{r} = d\boldsymbol{R} \qquad \text{Eq. 2.71}$$

This equation can be solved incrementally, iteratively or preferably by a combination of the two. Examples of such schemes are the *Euler-Cauchy* method (incremental), the *modified Newton-Raphson* method (iterative) or the *Riks-Wempner* method (combined method). The Riks-Wempner method is the basis for the nonlinear solver used in Abaqus. It is an arc-length method that combines an incremental approach (predictor) with an incremental approach (corrector). The mathematical details will not be elaborated here, but Figure 16 gives a visualization of the solution procedure.

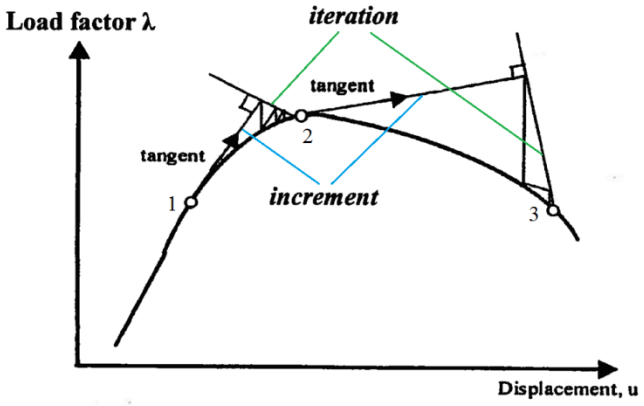

Figure 16 – Schematic illustration of the arc-length method. (Moan, 2012)

The steps are taken with a given arc-length in the load-displacement plane, and a steady state for the increment level is achieved iteratively. A new step can then be applied with a new arc-length, and so on. This method is effective and stable, and ensures that large deformations are properly accounted for.

2.4. Coupling of CFD and FEM

There exist different types of couplings between the fluid and solid domain. They are all categorized as *Fluid-Structure Interaction* (FSI)-problems. They are defined as problems where there is a dependency between hydrodynamic forces and the structural response. It is the numerical equivalent of the theoretical term hydroelasticity. This dependency may either go one way only, or there may be a mutual dependency.

The term FSI is used both for rigid body motions and for deformable bodies, which may cause some confusion. For FSI-problems with rigid bodies, only the rigid motions will be coupled to the fluid. These are defined by the geometry and mass distribution, as well as the 6 degrees of freedom of the rigid body. A typical problem is a conventional ship motion analysis. For deformable bodies interacting with a fluid, the deformations must also be taken into account, and possibly also the effect these deformations have on the fluid. For these analyses, a fluid analysis and a structural analysis will have to be solved simultaneously. In this thesis, FSI refers to this mutual dependency.

2.4.1. Coupling methods

For the conventional approach to marine simulations, the structure is assumed rigid as the fluid velocities and pressures are computed. The resulting pressures are then applied as a load history on a separate structural model to assess the structural integrity. Mapping of this pressure field onto the structural model may be complicated, and therefore the simulations may be performed simultaneously. This is called a *one-way coupled* analysis.

The pressure field is calculated using CFD for each time step, and exported onto the structural FE-model. This way, transient response may be accurately described. The pressure field is calculated neglecting these deformations, which may in many cases be sufficiently accurate. Examples of such cases are ringing or whipping of ship hulls.

If the deformations are large, the effects on the fluid cannot be neglected. In these cases, the full system of equations for both the fluid and the structural domain must be solved simultaneously. This is called a *two-way coupling*. For the CFD process, this means including a full structural analysis of the problem, with redefined boundary conditions and remeshing of the fluid domain for each time step.

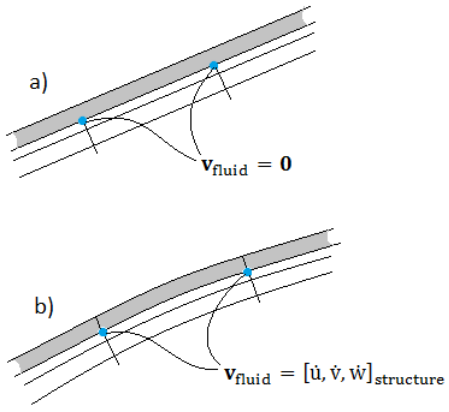

Figure 17 – Condition at the fluid-structure interaction boundary. a) Rigid body. b) FSI-model.

It is distinguished between *loose* and *strong* coupling. Loosely coupled problems are problems where the mutual dependency in time is low. An example would be a steady state deformable body in current. The time history is unimportant; only the resulting deformed steady state of the

solid and the fluid flow is important. A strongly coupled problem is a problem where the mutual dependency of two domains is great, and a small change in one domain leads to an immediate response in the other. Example of such cases are vortex-induced vibration of marine risers, or hydroelastic impact.

The hydroelastic wedge entering water constitutes a transient problem with large deformations relative to the plate thickness. In Section 2.1.2, a flat plate entering water was shown to have the following approximate initial conditions after the structural inertia phase

$$w_0 = 0$$
$$\dot{w}_0 = V \qquad \text{Eq. 2.72}$$

where w_0 is the initial deformation and $\dot{w}_0$ is the initial velocity at the middle of the plate. V is the wedge velocity at impact. This goes to show that the hydroelastic slamming problem is highly coupled, and the problem should be solved using a full two-way coupled analysis.

2.5. Coupling between STAR CCM+ and Abaqus

The software's chosen for the co-simulations in this thesis is STAR CCM+ from CD-ADAPCO and Abaqus from 3DS. They both have built-in modules supporting co-simulation with one another. The simulations are run from the STAR CCM+ environment, which includes Abaqus in its solver process. Abaqus is called upon at given intervals set by the user.

2.5.1. Field exchange

When conducting an FSI co-simulation, the nature of the coupling must be specified. This is done by specifying a set of FSI-boundaries, for which data are interchanged. The appropriate data must also be selected. It is imperative that the FSI-boundaries in both programs have the same coordinates, or else the co-simulation will fail due to topology inconsistency. For a DFBI-simulation this can be challenging, but can be dealt with by letting Abaqus calculate the rigid body motion. For the setup used in this thesis the wedge remains fixed at the origin throughout the impact, making the mapping of imported and exported fields easy. The data interchanged are structural deformations and hydrodynamic pressure.

Software	Export	Import
Abaqus	Deformations	Pressure
STAR CCM+	Pressure	Deformations

Table 1 – Field exchange between STAR CCM+ and Abaqus.

The deformations imported to STAR CCM+ may be under-relaxed between inner iterations. This is done to introduce the deformation smoothly, without sudden discontinuities leading to pressure divergence.

2.5.2. Coupling schemes

There are different coupling algorithms, and the algorithm chosen must reflect the degree of coupling in the physical problem. For loosely coupled problems, it is sufficient to update the fields between every time step. This is called explicit coupling schemes (see Figure 18). For strongly coupled problems, it may be necessary to update the fields at every outer iteration in the CFD process. This is called an implicit coupling scheme (see Figure 19). This leads to a more costly coupling, but the simulation will be more stable.

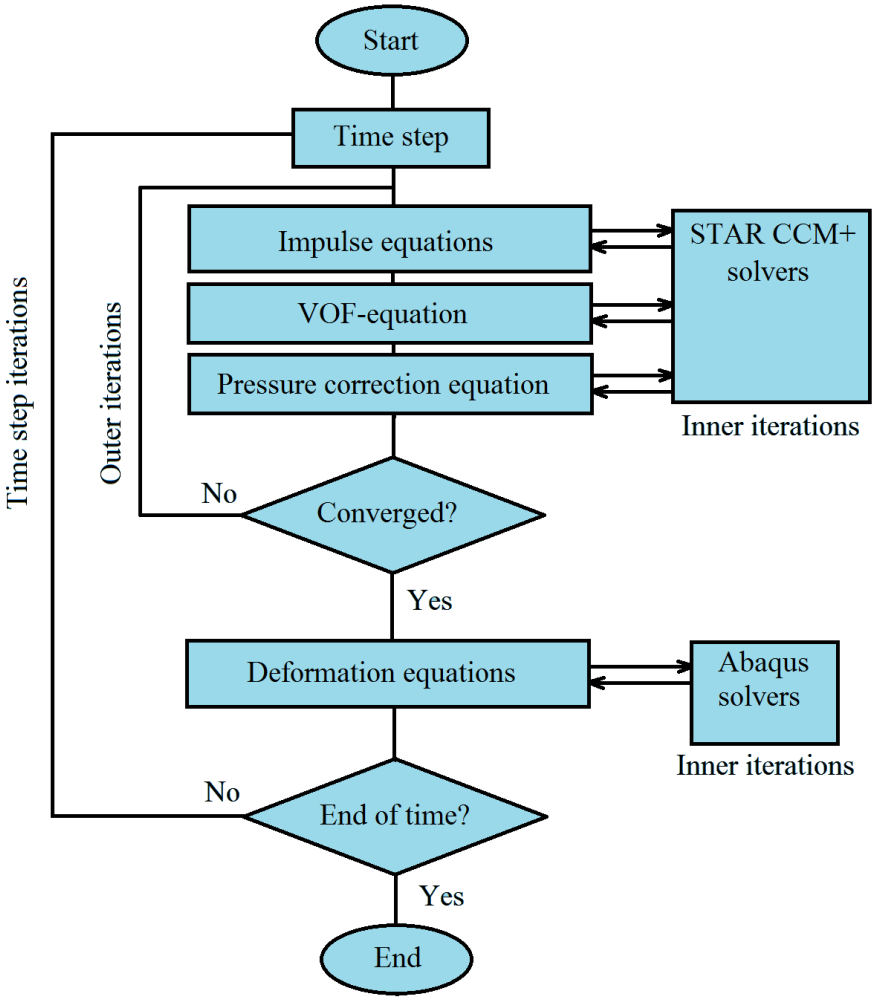

Figure 18 – Flowchart for a two-way coupled simulation with explicit coupling.

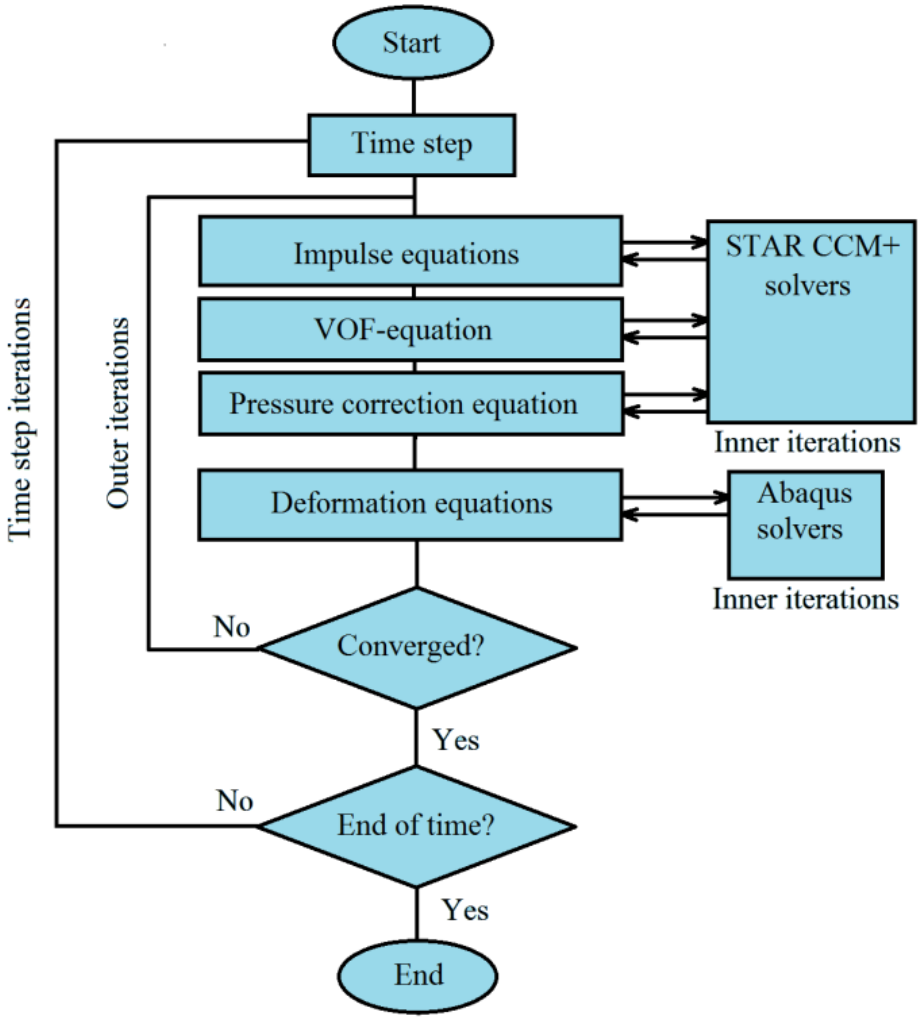

Figure 19 - Flowchart for a two-way coupled simulation with implicit coupling.

2.5.3. Mesh morphing

Regardless of whether a DFBI-model or a fixed mesh is applied, the mesh will have to be updated to account for the deformations. This is done by the *mesh morhper* model in STAR CCM+. The mesh morpher allows boundaries and nodes to move within the domain, and deforms the mesh for every time step. When the mesh morpher is activated, every boundary enclosing the fluid domain is given an additional boundary condition, determining the nature of the mesh morpher at this boundary. Some important morpher conditions are seen in Table 2.

Morpher condition	Description
Fixed	Nodes on this surface have zero displacement.
Floating	Nodes on this surface are free to move in all directions.
In plane	Nodes on this surface are allowed to move on the surface, but have zero displacement normal to the boundary.
Fixed plane	Nodes on this surface are allowed to move on the surface, but have zero displacement normal to the boundary. The boundary is treated as an infinite plane.
Co-simulation	Nodes on this surface are moved according to an imported displacement field.

Table 2 – Morpher conditions

The less constraint a boundary is given, the less computational cost the remeshing will require. The morphing is computed on the basis of control vertices. They are essentially lines that are interpolated on the basis of the nodal positions, and are used to reduce computational cost for the mesh morpher. The *vertex thin factor* controls the number of control vertices used. By lowering the vertex thin factor, the morpher ignores a fraction of the nodal positions when computing the control vertices. Caution must be exercised when using this factor, as boundary displacement may become inaccurate. It should be noted that it is not only the nodes that move, but the boundary itself. When the mesh boundary conditions are set, the 3-D mesh is recomputed.

The effect of structural deformation on the fluid properties is expressed through the *grid flux*. The grid flux is calculated as

$$\Phi = \iint_{S_k} \mathrm{v} dS \approx \mathrm{v} S_k \qquad \text{Eq. 2.73}$$

where S_k is the area of a cell boundary and v is the boundary-normal displacement velocity. It expresses the volume swept by the deformation between two time steps. For the co-simulation, the grid flux gives the impulse that leads to a change in velocity and pressure fields in the fluid domain. This effect can be under-relaxed or ignored altogether. For a steady state problem the grid flux term can be ignored, as the dynamics leading to the deformed state are of no concern. For a transient problem, and particularly for a strongly coupled problem, the effect cannot be neglected. As the grid flux term is a source of instability for the simulation, the effect may be under-relaxed. This is particularly relevant for the initial phase of the simulation, where the fluid fields are still non-physical. It may also be used to stabilize a simulation with strong coupling.

3. CONVERGENCE TESTS AND VERIFICATION OF THE CFD MODEL

3.1. A verification and validation study

Johannessen (2012) conducted a thorough convergence analysis for 2-D and 3-D wedges in STAR CCM+. In his work, Johannessen presents convergence tests with respect to domain size, grid size, time steps as well as a number of numerical parameters. Results are presented for wedge impacts at various angles, and compared to the results of Zhao and Faltinsen (1993). With reference to this work, results for various angles and impact velocities are not included in the scope of this thesis. A single setup is chosen to demonstrate the performance of the numerical model. For this setup, convergence tests and some general discussion will be presented.

3.2. Model setup

To verify the numerical model, a 2-D rigid wedge entering water at constant speed will now be considered. A model is made in STAR CCM+, with properties as can be seen in Table 3 and Table 4. ρ is the density and μ the is dynamic viscosity.

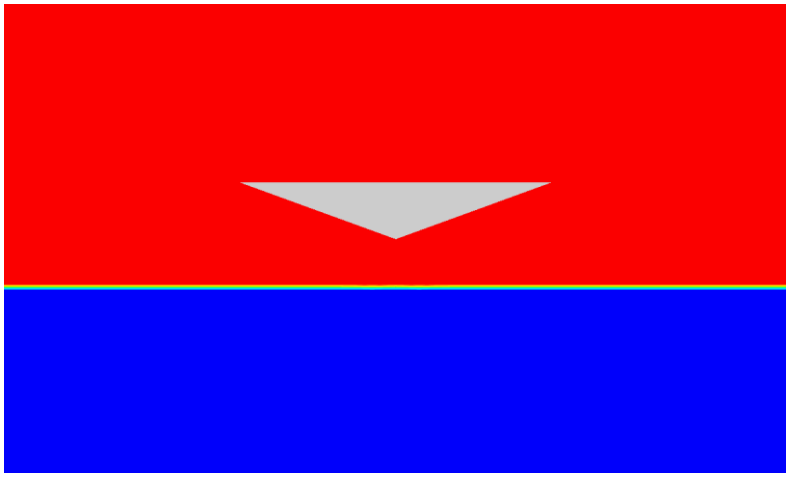

Figure 20 – VOF scene.

Property	Value
Length of wedge bottom [m]	1
Impact angle [°]	20
Impact velocity [m/s]	1

Table 3 – Problem setup

Material constant	Value
ρ_{water} $[kg/m^3]$	997.5
M_{air} $[kg/kmol]$	28.97
μ_{water} $[Ns/m^2]$	$8.89*10^{-4}$
μ_{air} $[Ns/m^2]$	$1.85*10^{-5}$
g $[m/s^2]$	-9.81

Table 4 – Physical constants

The wedge is fixed with the wedge apex at the origin. Water is entering the domain from below. Applying this configuration is practical for an idealized geometry, implying a minimal requirement to the mesh. For moving objects other mesh techniques must be used. Assuming symmetry, only half a wedge is modeled, with a symmetry boundary at the vertical plane crossing through the wedge apex.

Although the model is called two-dimensional, it is in fact a three-dimensional model with a low in-plane thickness. This is done mainly due to modeling convenience. Star CCM+ models are built up of volume cells, and although two-dimensionality is supported, the possibilities within this configuration are limited. With regard to the coupled analyses that will be run later, it is chosen to set up the model as a thin 3-D model.

3.2.1. Boundary conditions

The boundaries can be seen in Figure 21. The Bottom boundary is set to *velocity inlet*, where the velocity and the composition of fluid components (air and water) are specified. Only water is allowed to enter the domain. Similarly, the top boundary is set to *pressure outlet,* where the pressure and the composition of fluid components are specified. Only air is allowed to exit the domain. The latter is not strictly necessary, but is done merely for the sake of convenience. The wedge itself is given a *wall* boundary condition, meaning a *no-slip* boundary with $\mathbf{v} = \mathbf{0}$. If viscosity is neglected, this boundary is called a *free-slip* boundary, and the limitations to velocity is reduced to $v_{normal} = 0$. By using the *symmetry* condition at the front and back boundaries, two-dimensionality is ensured. The *symmetry* boundary condition is indistinguishable from a *free-slip* boundary, with the additional requirement that all gradients are zero by definition. The boundary conditions given can be seen in Table 5.

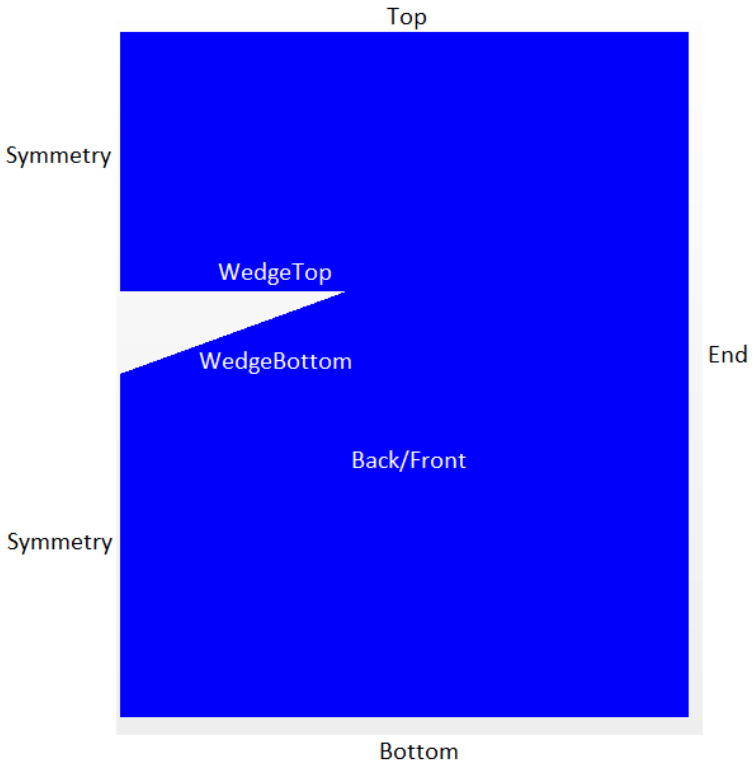

Figure 21 – Boundaries for the fluid domain.

Boundary	Condition
Front	Symmetry
Back	Symmetry
Symmetry	Symmetry
End	Symmetry
Top	Pressure outlet
Bottom	Velocity inlet
WedgeTop	Wall
WedgeBottom	Wall

Table 5 – Boundary conditions.

3.2.2. Initial conditions

The free surface is initialized at 30cm below the wedge. It is defined through the VOF-method. The initial velocity field is set to 1m/s in the vertical direction, normal to the velocity inlet. The

reason for the initial distance between the wedge and the free surface is to allow a steady velocity field and pressure field to be established before impact. The pressure is set to zero at the pressure outlet. The hydrostatic pressure is implicitly accounted for through the VOF-method.

Region/Boundary	Condition	Value
Top	Outlet pressure [Pa]	0
Bottom	Inlet velocity [m/s]	1
Entire domain	Initial velocity field [m/s]	1

Table 6 – Initial conditions.

3.3. Convergence tests on 2-D rigid wedge

In his master's thesis, Johannessen performed a number of convergence tests for different 2-D and 3-D wedge setups in STAR CCM+ (Johannessen, 2012). He primarily investigated convergence with respect to the pressure distribution on the wedge bottom and the residuals. Table 7 shows some of the conclusions of these tests, and constitutes a basis for the investigation performed in this thesis. There is, however, a large difference in our convergence criterion. Whereas Johannessen investigated the slamming phenomenon in order to achieve a convergent pressure distribution at the wedge, the convergence criterion here has been set as the total vertical force on the wedge. This is achieved with less computational costs than the pressure convergence, because the pressure peak must not necessarily converge. This is justified by considering that for dynamic response to hydroelastic slamming it is the total force impulse on the wedge that is of importance. As long as this impulse is correct, the true pressure peak may in fact be abandoned before it has converged. This is true from a theoretical point of view, and if the numerical model stays stable it is the most economic approach.

Tested property	Value
Domain height [m]	3.5
Domain width [m]	3
Minimum cell height [m]	0.00054
Minimum cell width [m]	0.0025
Viscosity	Laminar
Convection discretization	2^{nd}-order
Time discretization	2^{nd}-order
Velocity under-relaxation	0.9
Pressure under-relaxation	0.4
Inner iterations	20

Table 7 – Results from the convergence tests conducted by Johannessen (2012).

3.3.1. Mesh size

The mesh is built up by the hexahedral and tetrahedral cells. The domain is divided into subdomains with individual mesh size definitions (see Figure 22). They correspond to the expected need for accuracy in capturing the free surface, as well as requirements in regions with high gradients and fluid velocities. In addition, a surface layer is added on the wedge bottom (see Figure 23). This is done to ensure a very fine mesh at the interface between fluid and the wedge bottom, capable of capturing high velocities, high gradients and the turbulence model. Three different meshes are tried. Data for the different runs can be seen in Table 8.

The grid size determines to which degree high gradients and pressure peaks are correctly captured. Grid size and time steps must always be considered simultaneously, because the convergence and stability of the solution depend on their mutual relationship. For example, a very fine mesh will be of no avail, if the time step is too large to capture the changes between neighboring cells. The courant number is well fit to assess this relationship. For elaboration on this, it is referred to the discussion in Section 2.2.12.

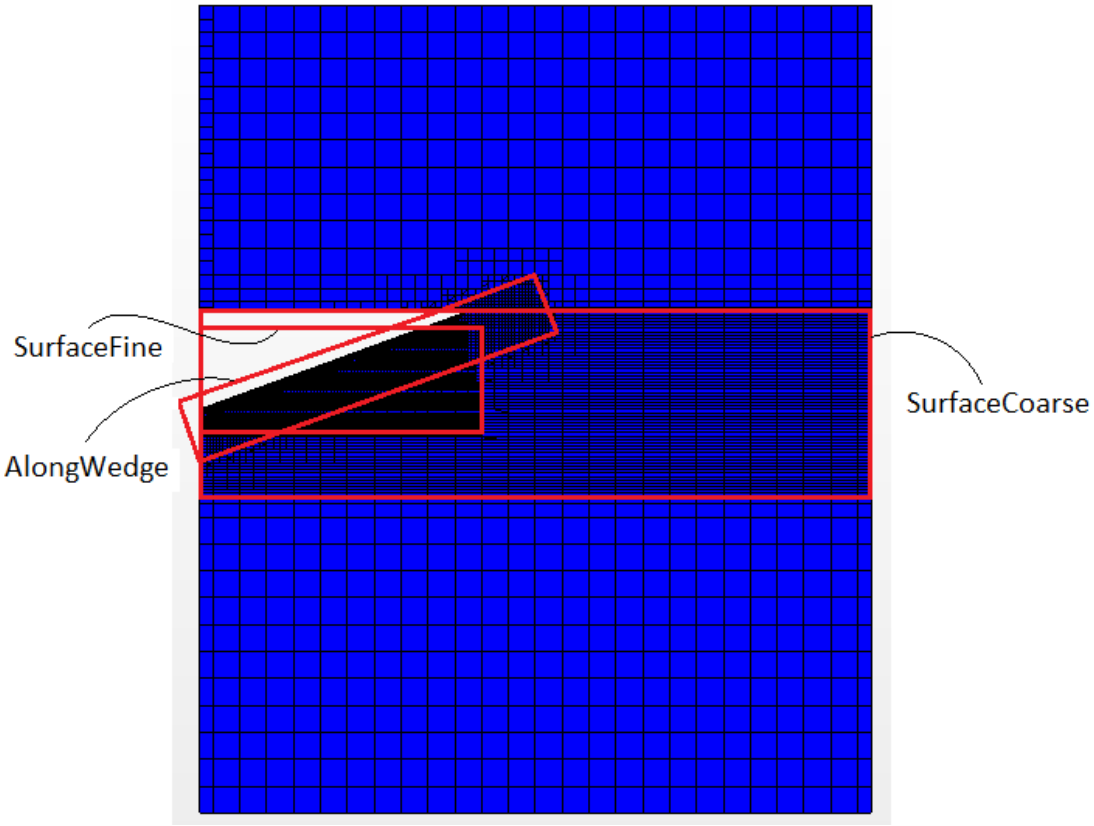

Figure 22 – Mesh with volumetrically controlled subdomains.

Mesh size	Coarse mesh	Medium mesh	Fine mesh
Total number of cells [-]	2936	9373	11785
Default (x,z) [m]	(0.1 , 0.1)	(0.1 , 0.1)	(0.1 , 0.1)
SurfaceCoarse (x,z) [m]	(0.1 , 0.0125)	(0.1 , 0.0125)	(0.1 , 0.0125)
SurfaceFine (x,z) [m]	(0.1 , 0.0125)	(0.05 , 0.00625)	(0.05 , 0.00625)
AlongWedge (x,z) [m]	(0.05 , 0.0125)	(0.00625 , 0.00625)	(0.00625 , 0.00625)
Number of surface layers [-]	4	8	10
Surface layer thickness [m]	0.02	0.02	0.03

Table 8 – Mesh setups.

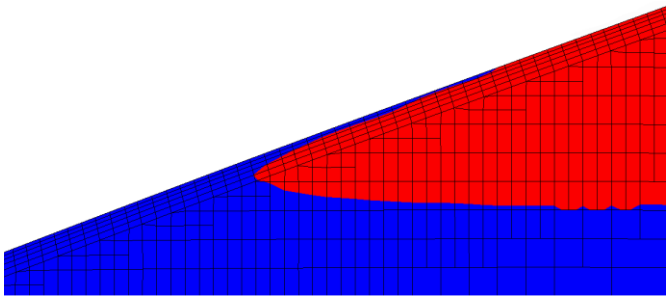

Figure 23 – Surface layer captured during the simulation.

Figure 24 shows the pressure coefficient along the wedge at t = 0.06s after impact for the different mesh setups. It is seen that the magnitude of the pressure peak grows with finer mesh, but the width of the peak decreases. Time steps were chosen so that $C_r \leq 1$ on the wedge bottom during the impact.

As the goal for these tests is to find a pressure that will suffice for a co-simulation with Abaqus, it is not the capturing of the pressure peak that is of importance, but rather the total vertical force on the wedge bottom. As we will see in Section 4.2.1 the total vertical force does in fact converge for lower time steps and coarser meshes than what is the case for the pressure peak. This is understood by considering that the pressure integrated over the wedge may converge although the peak has not yet converged.

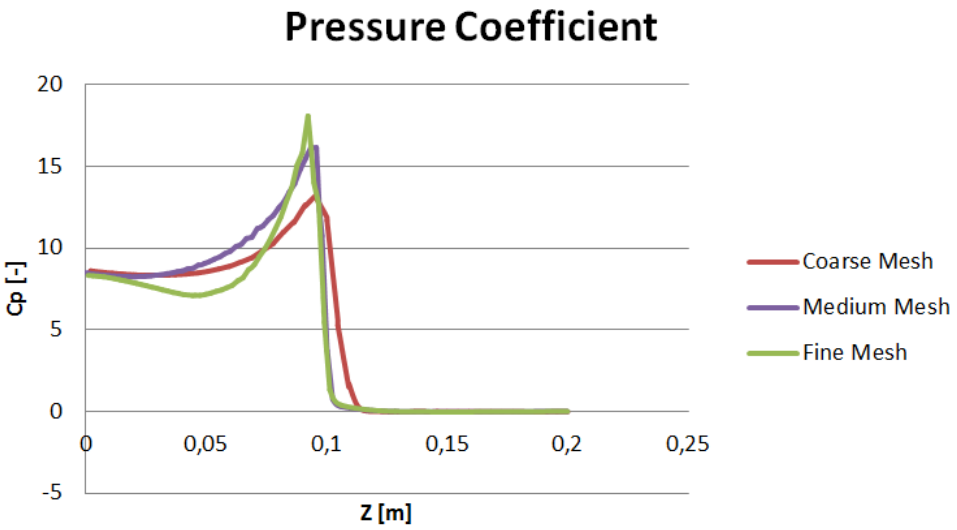

Figure 24 – Pressure coefficients for different meshes.

3.3.2. Domain size

A convergence test has been performed with respect to the domain size surrounding the wedge. Due to the symmetry boundaries at all vertical boundaries surrounding the wedge, it is expected that the domain size will affect the solution. Four domain sizes are tried, see Table 9.

Domain property	Small domain	Medium domain	Large domain	Very large domain
Domain height [m]	2.5	4	5	8
Domain width [m]	2.5	3	4	6
Total cell count [-]	14520	15010	15750	17280

Table 9 – Domain size setups.

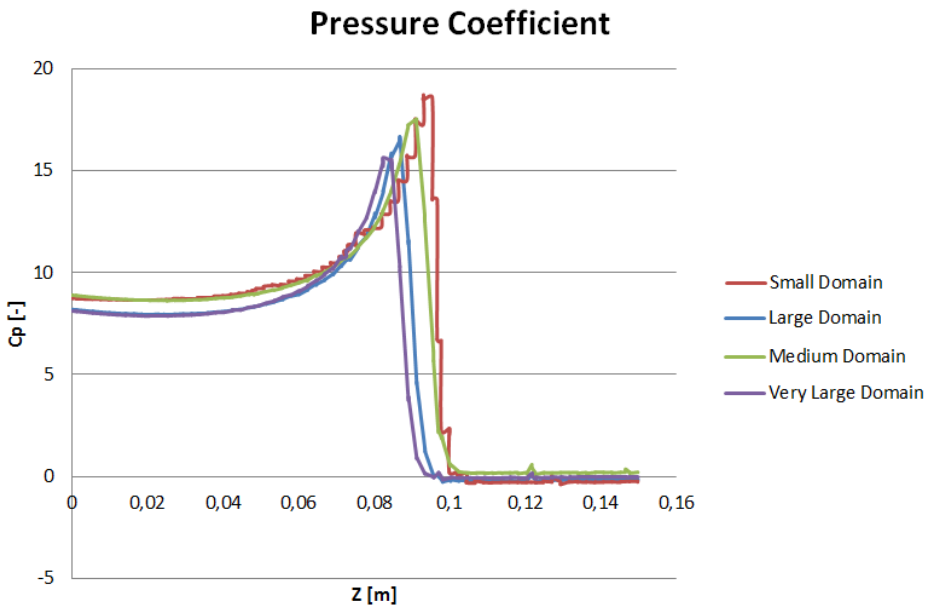

Figure 25 – Pressure coefficient on the wedge bottom for different domain size setups.

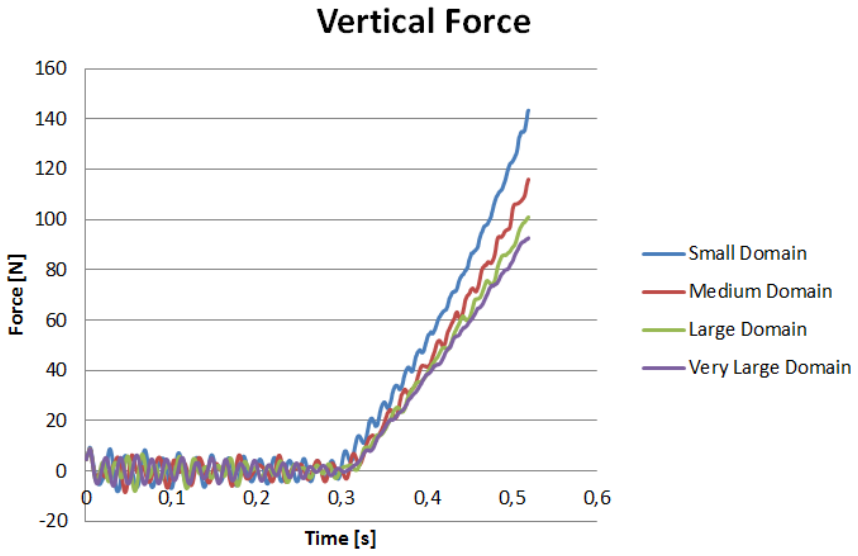

Figure 26 – Total vertical force on the wedge bottom for different domain size setups.

Figure 25 and Figure 26 show results from the four different domain sizes. It is evident that the smaller domains tend to under-predict the pressure field, and hence the total vertical force on the wedge. It is curious, however, that the pressure and the vertical force do not seem to converge properly, even for domain sizes far greater than the ones found by Johannessen (2012). This indicates that the rate of convergence with respect to domain size is dependent on other parameters than domain size only. Sources for this difference in convergence could be mesh resolution, time steps, as well as the physics included in the simulation.

By evaluating Figure 25, it is seen that the pressure distribution on the wedge bottom is not properly captured, due to a coarse mesh. Visually, this effect is emphasized by the fact that the model is three-dimensional, with every z-coordinate along the wedge bottom having multiple readings. Later, we only monitor the middle nodes along the wedge bottom, and get more smooth curves.

The total vertical forces seen in Figure 26 seem to oscillate. There is no obvious explanation for this behavior. One reason could be shock waves in the fluid domain. Another reason could be trapped air oscillating, but by evaluating the VOF-images, no air is seen on the wedge bottom. One final suggestion is that it could be due to air vortexes being shed at the wedge apex. This also seems strange, because it is not expected that air-induced pressure fluctuations should have such an impact on the total force. Of course, the oscillations could merely be the result of inaccurately set numerical values. As will be seen later, these oscillations do in fact disappear, as the model gets more properly tuned.

3.3.3. Viscosity

The effect of viscosity has been investigated. In his thesis, Johannessen concluded that a laminar model could describe the slamming phenomenon sufficiently accurately, and that the complex turbulence models available in STAR CCM+ should be avoided. However, to simplify the problem further, a comparison between a turbulent model and an inviscid model is presented in the following. With reference to the theory in Section 2.1.1, it is expected that the effect of viscosity is negligible.

Figure 27 shows the total vertical force on the wedge for an inviscid and a viscid simulation. It is seen that although minor fluctuations differ, the trend lines remain almost identical. This shows that turbulence may in fact be neglected, and corresponds well with the assumptions of water impact theory.

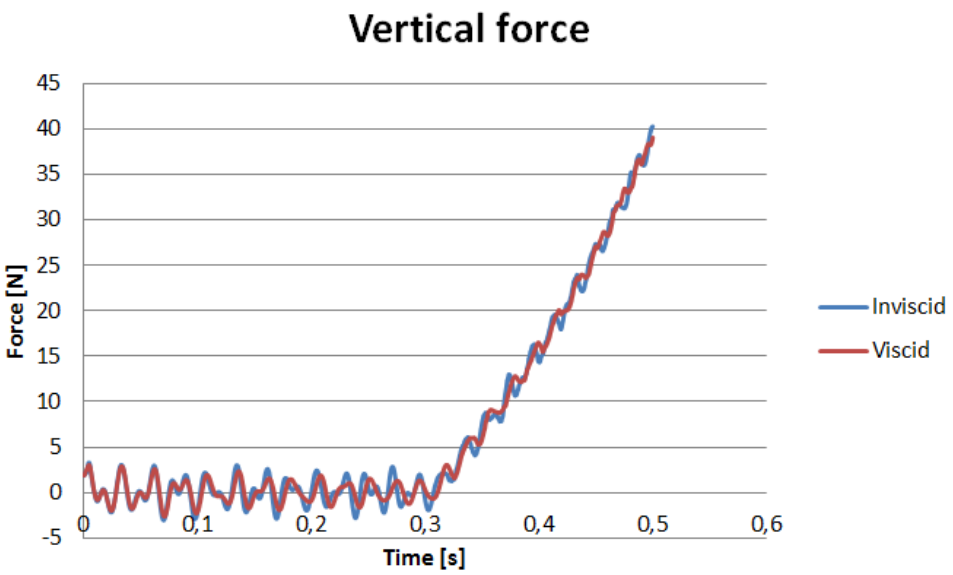

Figure 27 - Total vertical force on the wedge bottom for a viscid simulation and an inviscid simulation.

3.4. Comparison with previous results

To verify the numerical model, a comparison with previous results has been conducted. The setup for the model can be seen in Table 10. The setup is based on the knowledge acquired during the convergence tests. For comparison, the results of Zhao and Faltinsen (1993) and Johannessen (2012) are chosen. These results have been verified by comparison with experiments, and are considered to be accurate.

Property	Value
Domain height [m]	4
Domain width [m]	3
Minimum cell height [m]	0.0018
Minimum cell width [m]	0.0035
Viscid/Inviscid	Inviscid
Convection discretization	2nd order
Time discretization	1st order
Velocity under-relaxation	0.9
Pressure under-relaxation	0.4
Inner iterations	5
Time step [s]	0.0001

Table 10 – Model setup.

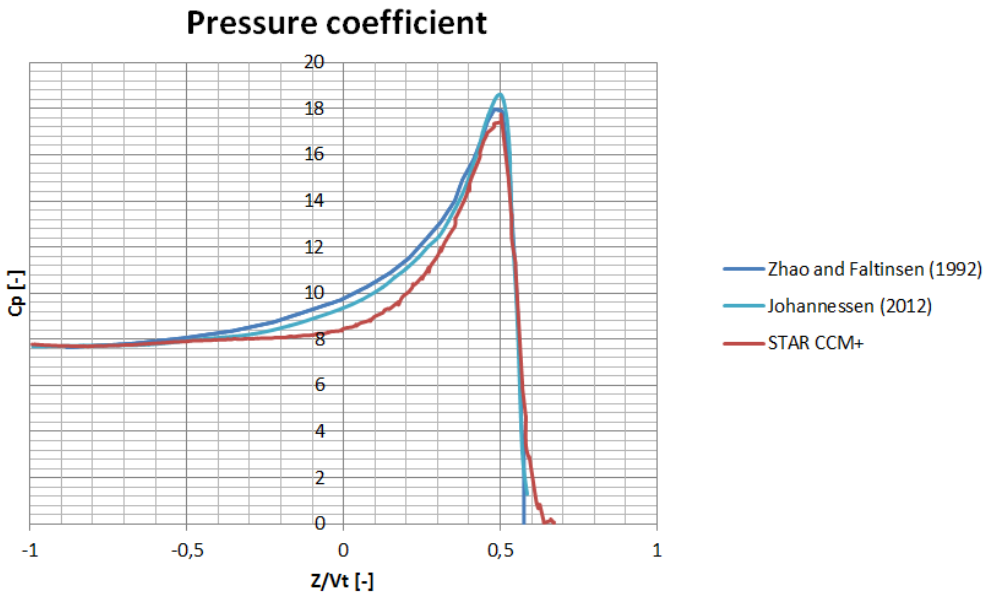

Figure 28 – Comparison between the current model and previous results.

A good agreement is seen between the results. The pressure peak has approximately the same value for all three setups.

The proper settings for the impact problem are found to be highly case-dependent. The needed mesh size will depend on the physics chosen. The time steps will depend on the mesh size. The number of inner iterations is strongly dependent on the under-relaxation factors, and the correct under-relaxation factors will depend on the chosen solver algorithms. Therefore, convergence tests should always be conducted. Only by studying the residuals and by running numerous setups with ever finer mesh and lower time steps, can convergence be assured.

4. VERIFICATION OF CO-SIMULATION MODEL

To verify the hydroelastic simulation method, the experiments presented by Panciroli et al. (2012) are chosen for comparison. A model is built in STAR CCM+ and Abaqus. To verify the model, convergence tests have been performed for both the hydrodynamic model and the structural model. Coupled analyses are performed and compared to the experimental values. The results are discussed.

4.1. A hydroelastic experiment

In 2012, several papers were published in cooperation between Università di Bologna and Southern Illinois University, documenting experiments on water-entry of an elastic wedge (Panciroli et al., 2012, Panciroli et al., 2013, Panciroli, 2013). More than 1200 runs were conducted, and a numerical model was used to compare with the experimental results. The experiments will be used as a comparison to the numerical approach presented in this thesis, and are therefore elaborated in the following.

The experimental setup is shown in Figure 29 and Figure 30. Material and geometrical data can be seen in Table 11 and Table 12. Wedges consisting of two 300mm long plates were dropped into the water, along fixed rails on both sides. The plates were connected to a 27mm long reinforced support at the wedge apex. It was installed in order to be able to adjust angles for different runs. Angles were adjustable between 0° and 50°, and the maximum velocity was 8.8m/s. Accelerations and velocities were measured. Two strain gauges were installed at 30mm and 120mm distance to the support.

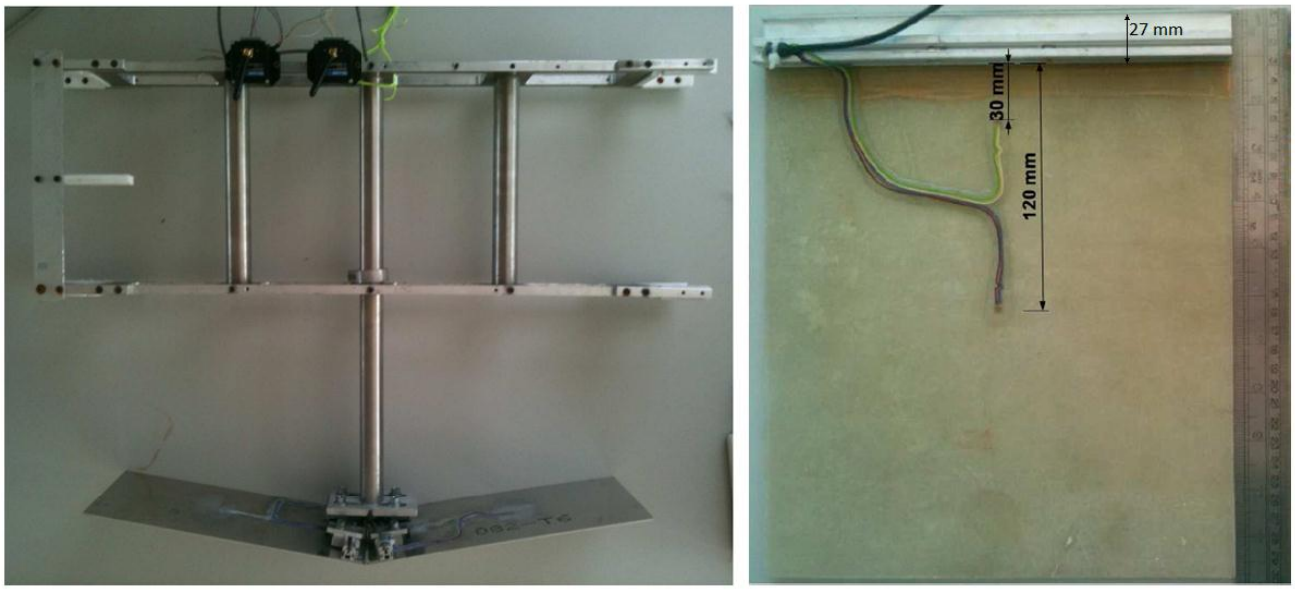

Figure 29 – Experimental setup. Left – The wedge-dropping installation. Right – The strain gauges installed at the wedge plate. (Panciroli, 2013)

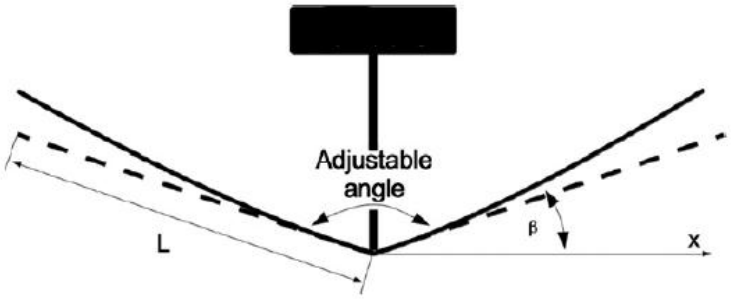

Figure 30 – Idealized experiment setup. (Panciroli, 2013)

Material	E [GPa]	$\boldsymbol{\nu}$ [-]	$\boldsymbol{\rho}$ $[\boldsymbol{kg/m^3}]$
Aluminium	68	0.3	2700
Vinylester	20.4	0.28	2650

Table 11 – Material data for the elastic wedge plates.

Object	**Length [mm]**	**Width [mm]**	**Depth [m]**	**Thickness [mm]**
Wedge	300	250	-	2 and 4
Tank	1600	1000	800	-

Table 12 – Geometrical data for the elastic wedge plates.

It should be noted that the plate thicknesses are very low. The reason for this is to lower the stiffness and consequently induce hydroelastic behavior for larger angles and lower impact velocities. Also, the free end boundary is curious, and unconventional for slamming experiments, and for ship structures in general. This too was done in order to increase deformations for lower impact velocity (Panciroli et al., 2013). The resulting structure is a very light wedge with low bending stiffness.

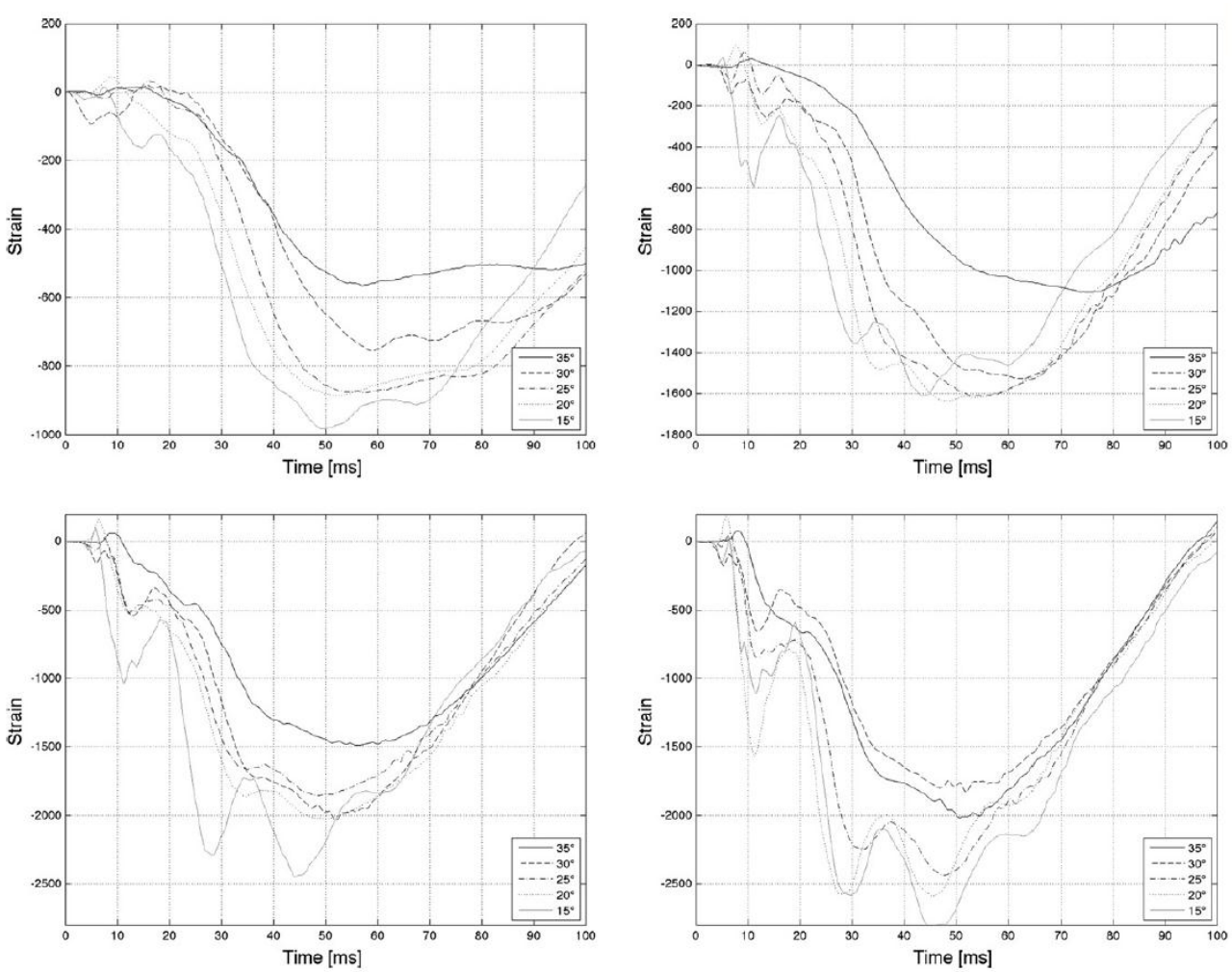

Figure 31 – Microstrain measured at 30mm from the wedge apex for various impact velocities. Top left - 3m/s. Top right – 4.2m/s. Bottom left – 5.2m/s. Bottom right – 6m/s. (Panciroli, 2013)

Figure 31 shows strain measurements for various impact velocities. In particular for the higher impact velocities, a distinct oscillatory behavior is seen. In the paper, it is concluded that the plate oscillates in more than one eigenmode. Their configurations actually showed experiments where higher order modes dominate the response. This is interesting from a theoretical point of view, emphasizing the extreme response of hydroelastic slamming. For ship structures, however, the plates will typically be clamped, and have a far greater thickness, increasing the stiffness dramatically, so that the mode of interest in any practical case should be the first one (Aarsnes, 1994).

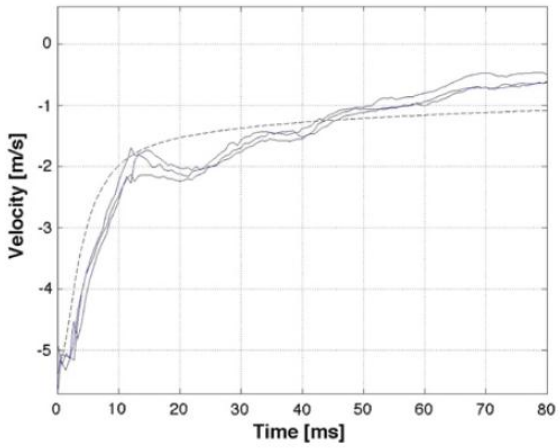

Figure 32 – Velocity monitoring for a 5m/s initial velocity impact. (Panciroli, 2013)

Figure 32 shows the development of the velocity for a 5m/s initial velocity impact. Note that the wedge velocity decays drastically during the first 10ms of impact. Due to the low weight of the wedge, high decelerations result from the large initial slamming pressures. This goes to show that a rapid deceleration of the wedge is expected before the water entry is over.

The numerical approach used consisted of an SPH-model for the fluid domain, assuming incompressible and inviscid fluid flow. Air was neglected, removing the possibility of entrapped air. 3-D effects were neglected, and symmetry assumed, so that only half of the wedge was modeled. The wedge was simulated using shell elements with four integration points. The nature of the numerical coupling has not been elaborated in the paper. Their results show good agreement with the experimental data.

4.2. CFD model

The numerical model in this thesis will be compared to the results from this experiment. A model is made in STAR CCM+. The wedge is built up by a 300mm long plate entering water at a velocity of 3m/s. The mesh and boundaries are shown in Figure 33 and Figure 34. Only half the wedge is modeled, with a symmetry condition at the vertical plane crossing through the wedge apex. The domain is given a small in-plane depth, so the impact can be considered a 2-D case. Data on the setup can be seen in Table 13. Boundary conditions and initial conditions can be seen in Table 14 and Table 15. Material data are the same as in chapter 3.

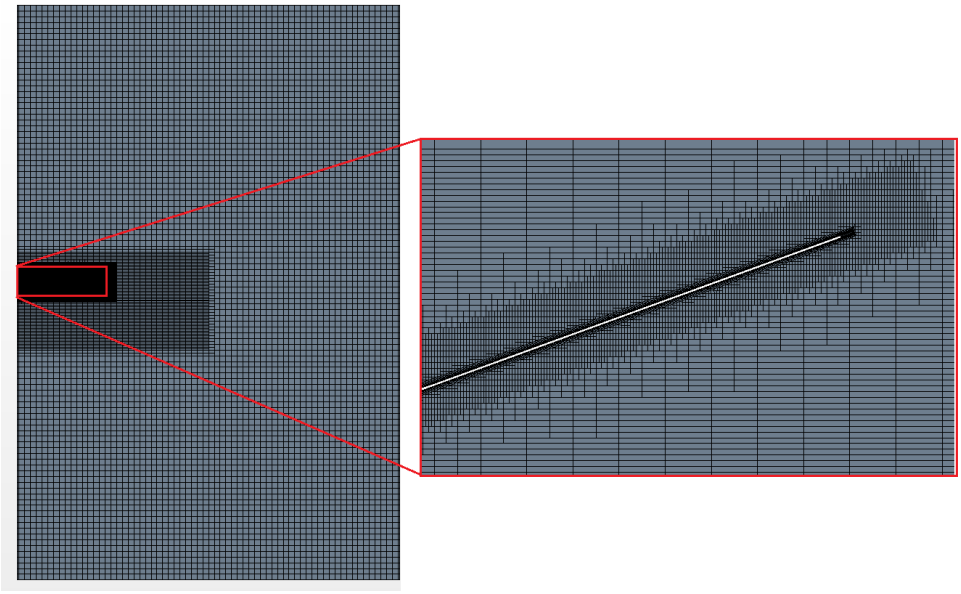

Figure 33 – CFD-mesh for the co-simulation.

Figure 34 – Domain boundaries.

Property	Value
Domain depth [m]	0.005
Wedge length [m]	0.3
Wedge thickness [m]	0.002
Wedge angle [deg]	20
Minimum cell height [m]	0.0004
Minimum cell width [m]	0.002
Number of cells [-]	89639
Impact velocity [m/s]	3
Viscosity	No
Gravity	Yes

Table 13 – Simulation setup.

Boundary	Condition
Front	Symmetry
Back	Symmetry
Symmetry	Symmetry
End	Symmetry
Top	Pressure outlet
Bottom	Velocity inlet
WedgeTop	Wall
WedgeBottom	Wall
WedgeEnd	Wall

Table 14 – Boundary conditions.

Region/Boundary	Condition	Value
Top	Outlet pressure [Pa]	0
Bottom	Inlet velocity [m/s]	3

Table 15 – Initial conditions.

4.2.1. Convergence tests

Convergence tests have been performed with respect to time step, domain size and water compressibility. The mesh and time steps are chosen so that $C_r \leq 1$ on the wedge bottom. The reason for these tests is merely to confirm and strengthen the results from Chapter 3. Water compressibility is investigated as a means to reduce instability, as discussed in Section 2.2.8.

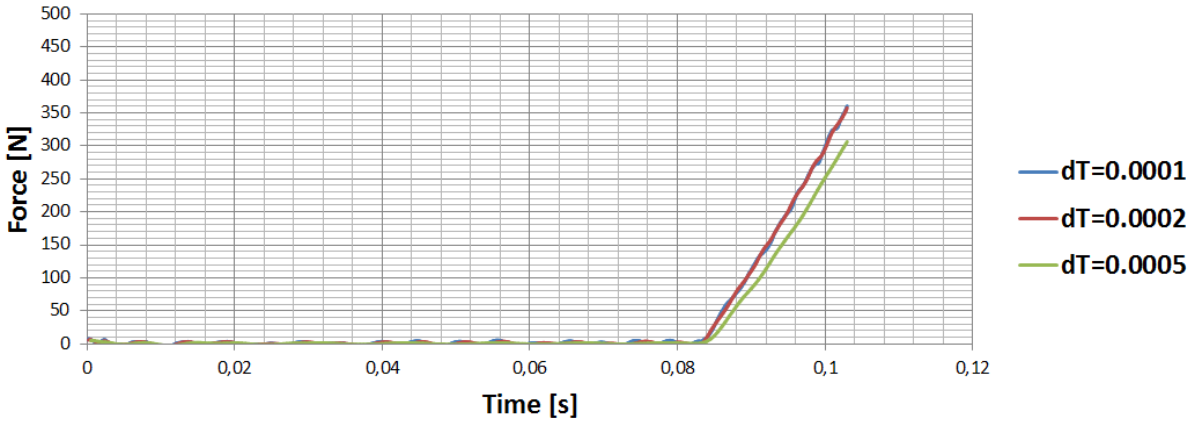

Figure 35 – Total vertical force on the wedge bottom for different time steps.

Figure 35 shows the total vertical force on the wedge at impact for various time steps. It is seen that the convergence of the total force is still reached at the same time step as for the wedge in chapter 3.

Table 16 shows the different domain sizes tried. Figure 36 shows the total vertical force on the wedge for the various domain sizes. It is seen that convergence is reached with the medium domain size. It is also seen that the oscillations on the total force are gone with this particular numerical setup.

Domain property	Small domain	Medium domain	Large domain
Domain height [m]	1.75	3	5
Domain width [m]	1	2	3
Total cell count [-]	80252	89639	109677

Table 16 – Domain sizes.

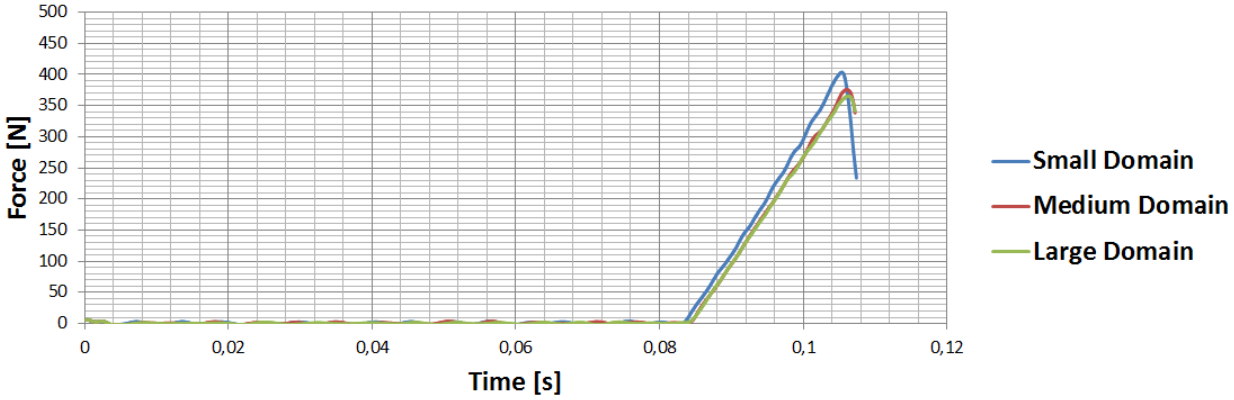

Figure 36 – Total vertical force on the wedge bottom for different domain sizes.

To stabilize the simulation compressibility may be introduced to the simulation. An artificial compressibility is introduced by defining a speed of sound in water of 300 m/s, and applying the expressions seen in Section 2.2.8. This is multiple times lower than in reality, but results show that the effect on the impact pressure is negligible (see Figure 37).

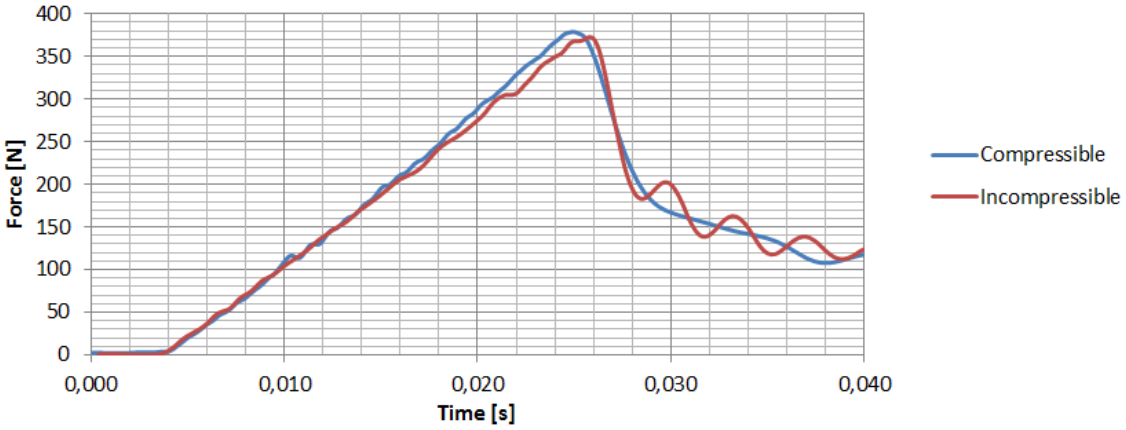

Figure 37 – Total vertical force on the wedge bottom for a compressible and an incompressible simulation.

It is seen that the total vertical force agree well for the two simulations. In fact, it is seen that for the setup chosen for this experiment, the compressible flow displays a steadier solution than the incompressible one, as expected. Note that the impact occurs slightly later for the compressible flow. This is because the water sinks under its own weight as it approaches the wedge. The conclusion is that compressibility may be an effective way to reduce divergence for the co-simulations.

4.3. FEM model

An Abaqus model is made, as seen in Figure 38. The wedge is 300mm long with a thickness of 2mm. The wedge is given a small in-plane depth corresponding to the one in the STAR CCM+ model. Only half the wedge has been modeled, as in STAR CCM+. The plate is clamped at the wedge apex and all other boundaries are free. For geometrical and material data, see Table 17 and Table 18.

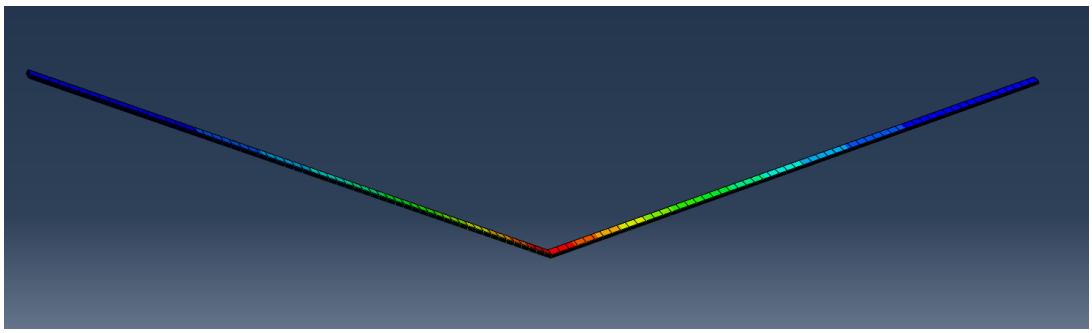

Figure 38 - Abaqus model.

Property	Value
Wedge length [m]	0.3
Wedge thickness [m]	0.002
Wedge depth [m]	0.005

Table 17 – Geometrical data.

Property	Value
Material	Aluminum
Density [kg/m3]	2700
Young's modulus [GPa]	68
Poisson's Ratio [-]	0.3

Table 18 – Material data

4.3.1. Element choice

The co-simulation demands a topological correspondence between boundaries that interchange data. They are the wedge top, the wedge bottom and the wedge end in STAR CCM+. These surfaces need to be properly modeled in Abaqus.

If the body were enclosing a volume, shell elements could be used for the FSI-boundary, as only a plane interface would be required. But because the wedge end is free and the fluid domain encloses the wedge plate on all sides, the only convenient way to create spatial correspondence between Abaqus and STAR CCM+ is to use solid elements. The reason for this is that shell elements do not possess a real thickness, and this makes it impossible to give a proper spatial reference between the shell element model and the STAR CCM+ model. This prohibits us from using shell elements. The elements chosen are C3D8R elements. These are 8-node, linear, solid elements.

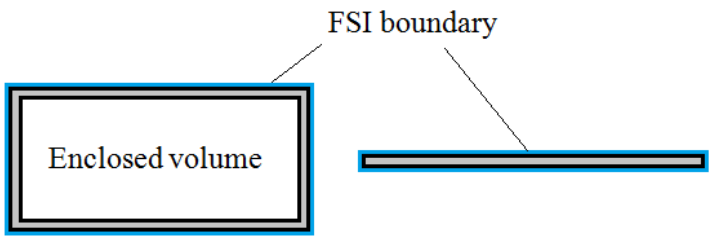

Figure 39 – FSI boundaries for different plate setups. Left – The FSI-boundary can be described with 2-D shell elements. Right – The fluid encloses all sides of the plate, and solid elements must therefore be used.

4.3.2. Convergence tests

To ensure that the model properly describes the physics of the structure, a convergence test on the mesh size is performed, and results are compared to theory.

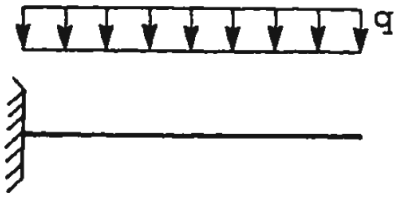

Figure 40 – Equivalent clamped beam.

The analytical solution for deformation of an equivalent beam with a uniform loading is

$$w = \frac{qx^2}{24EI}(x^2 + 6L^2 - 4Lx) \qquad \text{Eq. 4.1}$$

where q is the uniform load, EI is the stiffness and x is the position along the beam length L. The plate is loaded with an evenly distributed unit load of 1 N/m^2 normal to the wedge top, and a general static analysis is performed. Figure 41 and Figure 42 show the displacement along the wedge for different mesh setups.

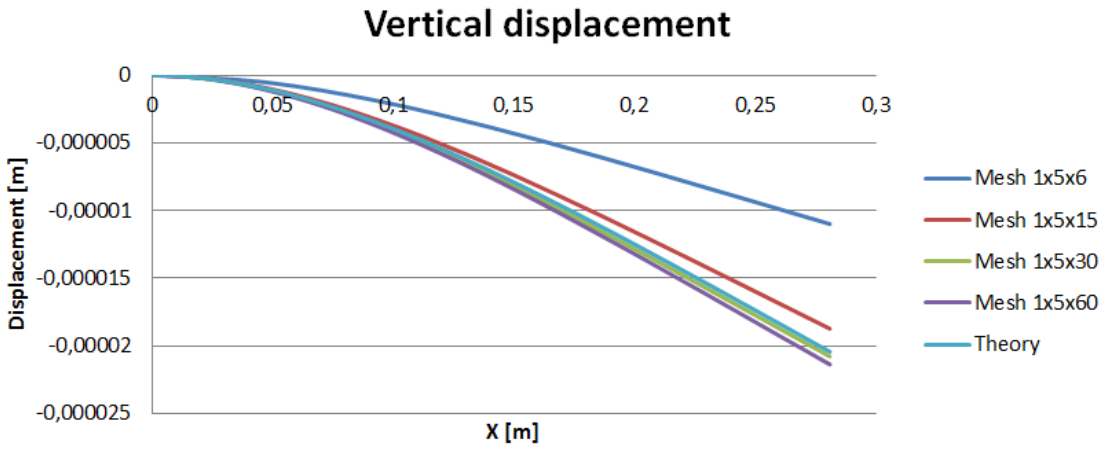

Figure 41 – Vertical displacement of the plate for different mesh refinements in the longitudinal direction.

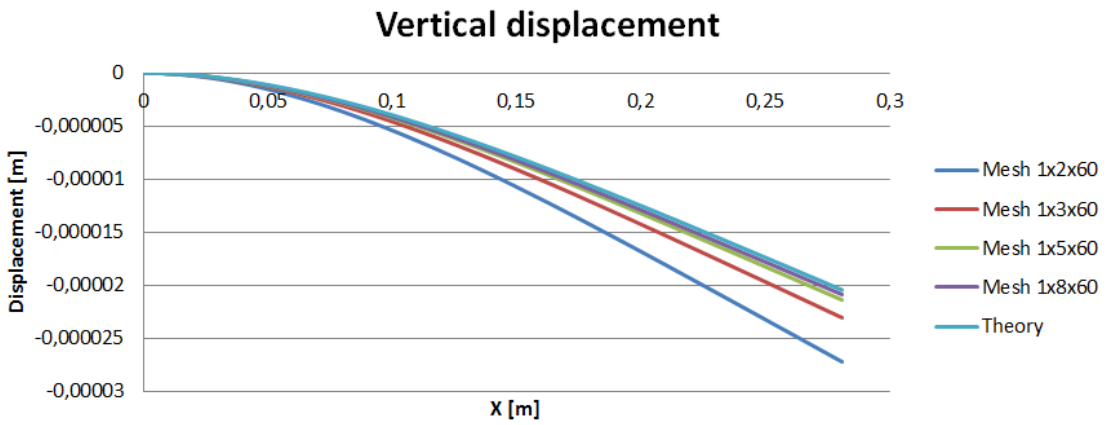

Figure 42 – Vertical displacement of the plate for different mesh refinements through thickness.

It is seen that for meshes with too few cells in length direction, Abaqus under-predicts the vertical deformation of the plate. At least 30 cells are required along the wedge to achieve a wedge deformation according to beam theory. However, it is expected that not only the first eigenmode will be excited during the co-simulation, but possibly other low order modes. Therefore, a mesh of 60 cells in length direction is chosen.

It is seen that for meshes with too few cells through the thickness of the plate, Abaqus over-predicts the deformation of the plate. At least 5 cells are required through the thickness of the wedge to achieve a wedge deformation according to theory.

4.3.3. Nonlinear geometry

The plate used in the experiment is very thin, and large deformations are observed. The effect of large deformations is investigated in Abaqus. To achieve large deformations, a uniformly distributed load of 3000 N/m^2 is applied to the wedge. A linear and a nonlinear, general static analysis are performed, see Figure 43.

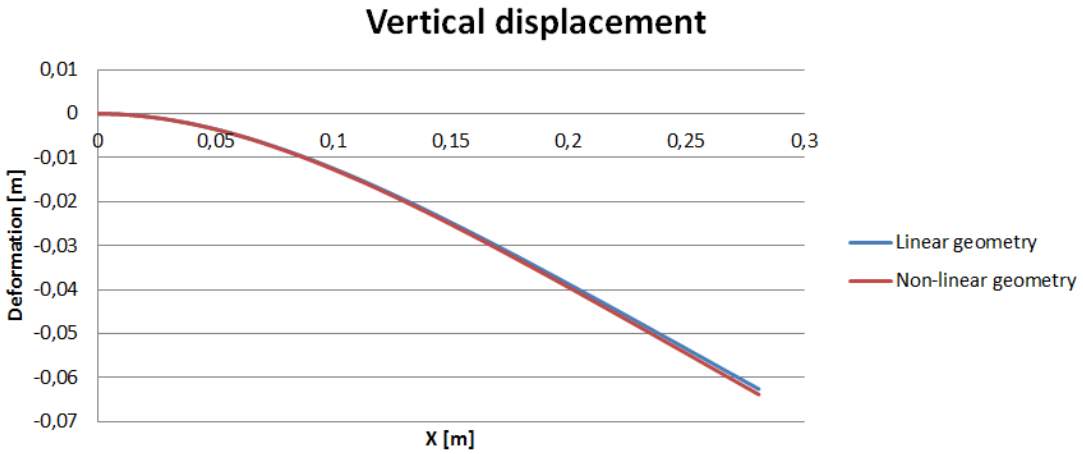

Figure 43 – Vertical displacement of the plate for a linear and a nonlinear analysis.

It is seen that the effect of large deformations is close to zero for the clamped wedge. This is understood by considering that the load is distributed normal to the wedge surface, making no contribution to the axial stress distribution. There are two main sources of geometrical nonlinearity. Firstly, forces are applied to the deformed geometry instead of the undeformed geometry. Secondly, large deformations lead to an updated stiffness of the structure. However, the boundary conditions do not allow for axial stresses to develop, and therefore no effect is seen on the maximum deformations.

4.3.4. Eigenfrequencies

The eigenfrequencies of the wedge have been calculated. They are found in Abaqus, by eigenvalue analysis, as described in 2.3.3. They are presented in the following, and compared to the experimental data presented by Panciroli (2013). It is seen that the Abaqus model display an excellent agreement.

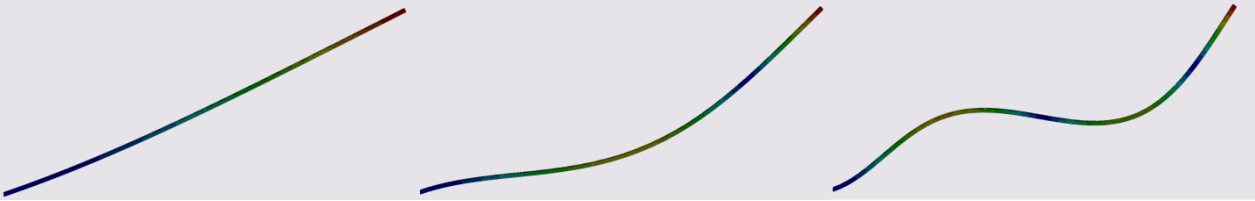

Figure 44 – Eigenmodes of the wedge plate. They are the first, second and third eigenmode from left to right.

Eigenmode	Abaqus	Experiment
1	18.06	18.01
2	113.2	112.89
3	316.9	316.1

Table 19 – Eigenmodes from Abaqus and experiment.

4.4. Co-simulation

Co-simulations have been performed with STAR CCM+ and Abaqus. The geometries are identical with the ones seen earlier in this chapter. The results are compared with experimental data, and the agreement is discussed.

4.4.1. Boundary conditions and initial conditions

Boundaries are identical with the rigid wedge CFD-case, with two exceptions. The front, back and end boundaries are changed from symmetry to free-slip walls. The reason for this is related to

the morphing of the mesh, which will be described in the next section. Additionally, the wedge top, wedge bottom and wedge end boundaries are now defined as co-simulation walls. This means that they will adapt the appropriate deformation field from Abaqus and update the geometry accordingly. The FSI boundaries can be seen in Figure 45, boundary conditions can be seen in Table 20 and initial conditions in Table 21.

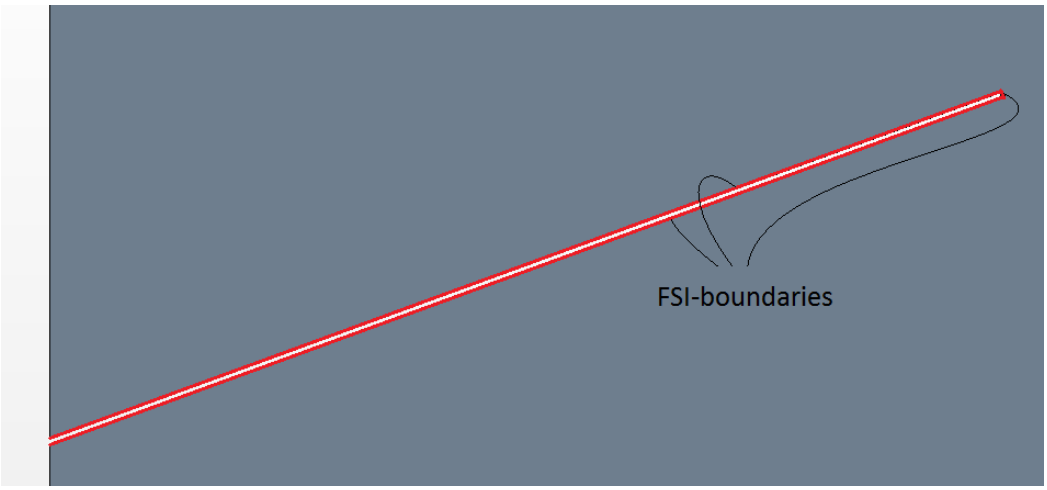

Figure 45 – FSI-boundaries.

Boundary	Boundary condition
Front	Free-slip wall
Back	Free-slip wall
Symmetry	Symmetry
End	Free-slip wall
Top	Pressure outlet
Bottom	Velocity inlet
WedgeTop	Co-simulation wall
WedgeBottom	Co-simulation wall
WedgeEnd	Co-simulation wall

Table 20 – Boundary conditions.

Boundary	Condition	Value
Top	Outlet pressure [Pa]	0
Bottom	Inlet velocity [m/s]	3
-	Initial velocity field [u,v,w] [m/s]	[0, 0, 3]
-	Initial free surface [m]	-0.25

Table 21 – Initial conditions.

4.4.2. Mesh

The mesh used in the co-simulation is similar to the one used in the initial rigid wedge studies. Hexagonal cells are used, with a prism layer on the wedge surface. Volumetric control has been used to refine the mesh additionally where needed, see Figure 46. A morphing mesh has been used, as described in Section 2.2.3. The configurations for the morpher are seen in Table 22.

Boundary	Morphing condition
Front	In-plane
Back	In-plane
Symmetry	Fixed plane
End	In-plane
Top	In-plane
Bottom	In-plane
WedgeTop	Abaqus co-simulation
WedgeBottom	Abaqus co-simulation
WedgeEnd	Abaqus co-simulation

Table 22 – Mesh morpher conditions.

The parts of the wedge in direct contact with the water are set as co-simulation walls with imported displacement fields. Other boundaries are given the in-plane and fixed plane morphing condition. This allows the volume mesh to follow the deformed wedge effectively.

The symmetry boundary condition in STAR CCM+ automatically adapts a symmetry-plane condition for the morpher. This was found to pose a condition on the mesh morpher that was not strict enough. For a variety of morpher conditions tried, the symmetry boundaries were morphing out of plane, causing pressure divergence and simulation crash. Therefore, the boundaries were changed to free-slip walls, for which the morphing condition may be specified.

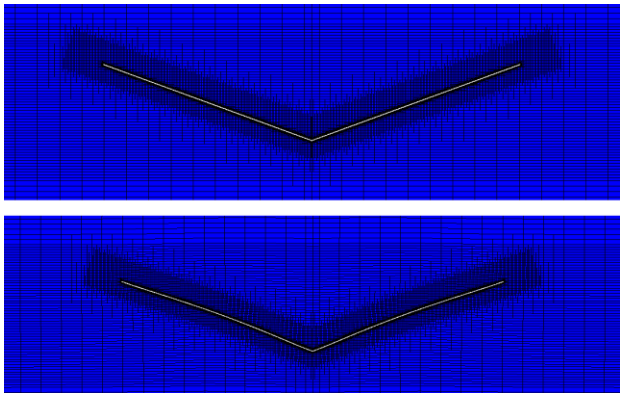

Figure 46 – Mesh scene for the original state and a deformed state.

4.4.3. Solver settings

The solver settings can be seen in Table 23. Due to the strong coupling between the fluid and the structure an implicit solver scheme is necessary. Attempts at co-simulating with an explicit scheme quickly diverged, even for very short time steps. The flow is modeled inviscid and compressible, with an artificial compressibility to suppress divergence. An Abaqus step is included at every inner iteration. The grid flux under-relaxation factor is set to 0.8, meaning that the fluid response to structural deformations is slightly reduced. Also, note that the under-relaxation factors for the velocity and pressure are lowered. This implies that a lower amount of the new solution is included at each new time step, and has been done to increase stability. The number of inner iterations must be raised, to reach a convergent solution with these under-relaxation factors. This has also been done. The STAR CCM+ solver first runs decoupled until shortly before impact. At this point, the co-simulation engine is enabled, and the Abaqus solver is included. This has been done to allow the fluid field to stabilize before the co-simulation starts.

Property	**Value**
Viscosity	No
Gravity	Yes
Compressibility	Yes
Convection discretization	2nd order
Time discretization	2nd order
Total simulation time [s]	0.130
Time of impact [s]	0.084
Velocity under-relaxation	0.9
Pressure under-relaxation	0.3
VOF under-relaxation	0.9
Imported fields under-relaxation	Adaptive 0.2-0.5
Grid flux under-relaxation	0.8
Time step [s]	0.00002
Inner iterations	20
Inner iterations per exchange	1

Table 23 – Solver settings.

Figure 47 and Figure 48 show comparison between the strain measured from the experiments, and the strain from the co-simulation for a 20° wedge and a 30° wedge. Abaqus operates with its own time history, and the impact occurs at approximately 4ms after the Abaqus monitoring has started. The strains are measured 30mm from the wedge apex, at the upper node with respect to the wedge thickness. It is seen that the agreement is rather poor. For the 20° impact the numerical model severely over-predicts the maximum strain. For the 30° impact the agreement is better, but not satisfactory. The non-zero initial strain for the 30° simulation is due to wedge bending under its own weight. This is not seen in the 20° impact, as the Abaqus solver was included closer to the time of impact.

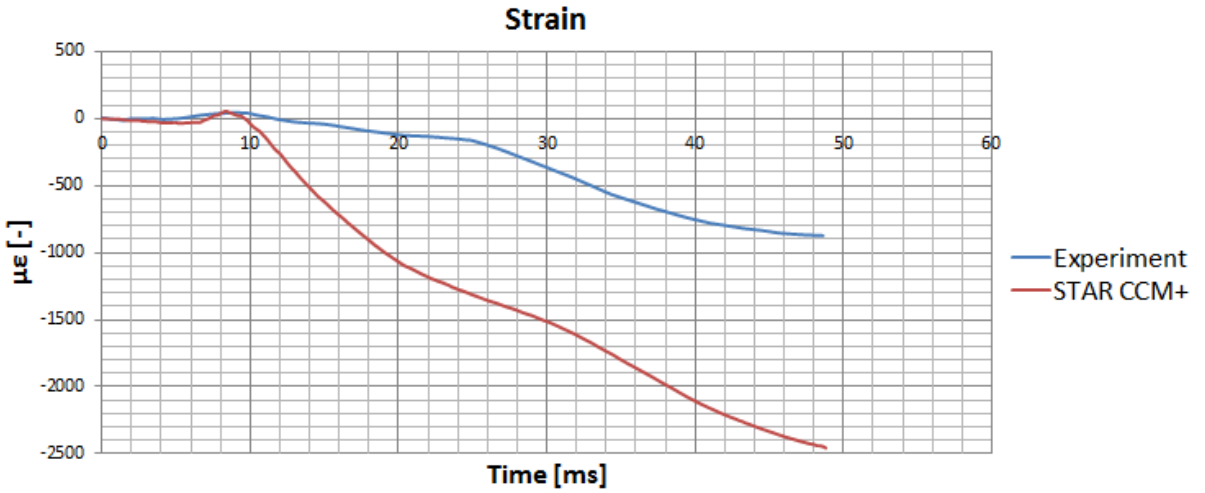

Figure 47 – Comparison between experiment and numerical model. Microstrains are measured at 30mm from the wedge apex. Impact velocity V=3m/s, wedge angle β=20°.

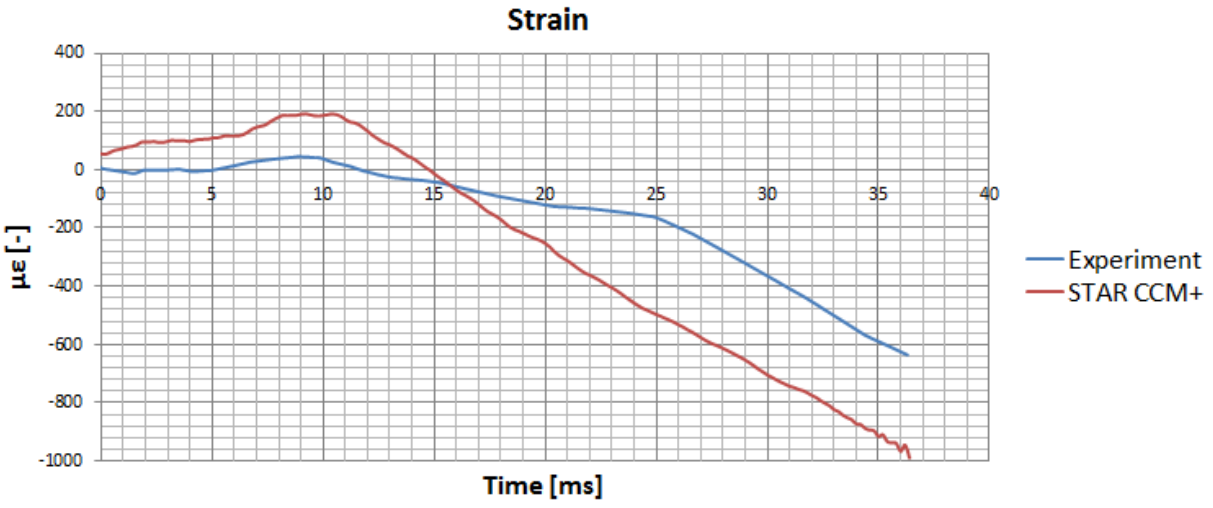

Figure 48 – Comparison between experiment and numerical model. Microstrains are measured at 30mm from the wedge apex. Impact velocity V=3m/s, wedge angle β=20°.

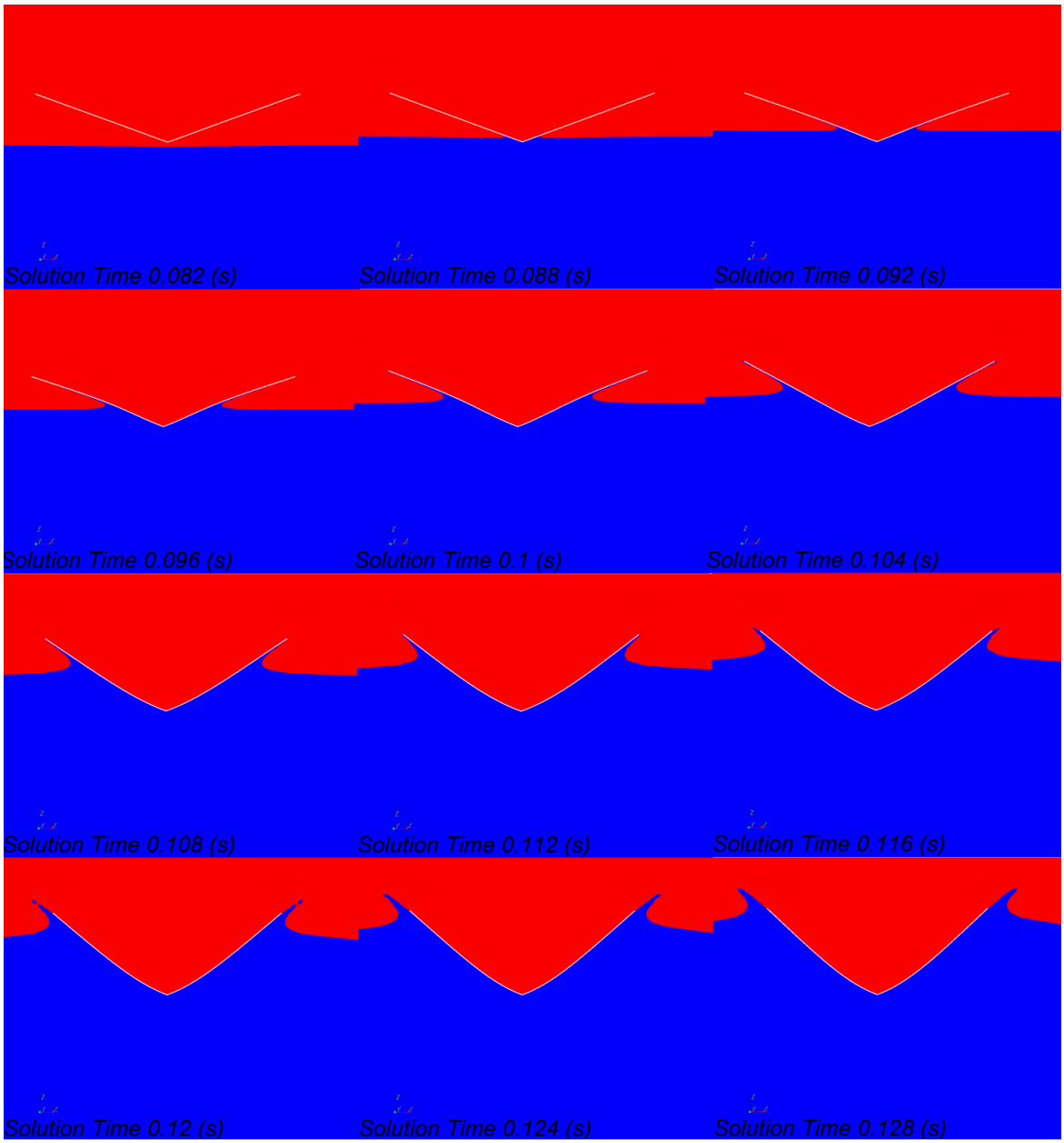

Figure 49 – VOF scenes from different time instants throughout the water impact. Impact velocity V=3m/s, wedge angle β=20°.

Figure 49 shows snapshots from the simulation. It is seen that the plate is deformed in its second eigenmode during the first 20ms of the impact. As the submergence increases the deformations are dominated by the first eigenmode. This observation is verified by observing the strain at 30mm and 120mm from the wedge apex, see Figure 50 and Figure 51. It is seen that for both angles, the strain monitored 120mm from the wedge apex show a large increase before dropping to negative values at approximately 20ms after impact. The increase corresponds to the tension during the second eigenmode deformation (Solution time<0.1s in Figure 49), and the negative

strains correspond to the compression during the first eigenmode deformation (Solution time>0.1s in Figure 49).

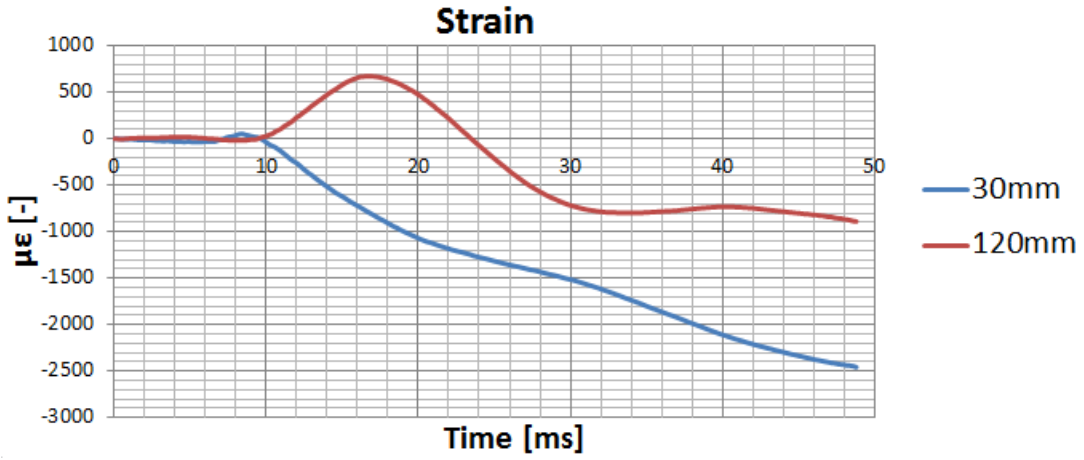

Figure 50 – Strains monitored at 30mm and 120mm from the wedge apex, β=20°.

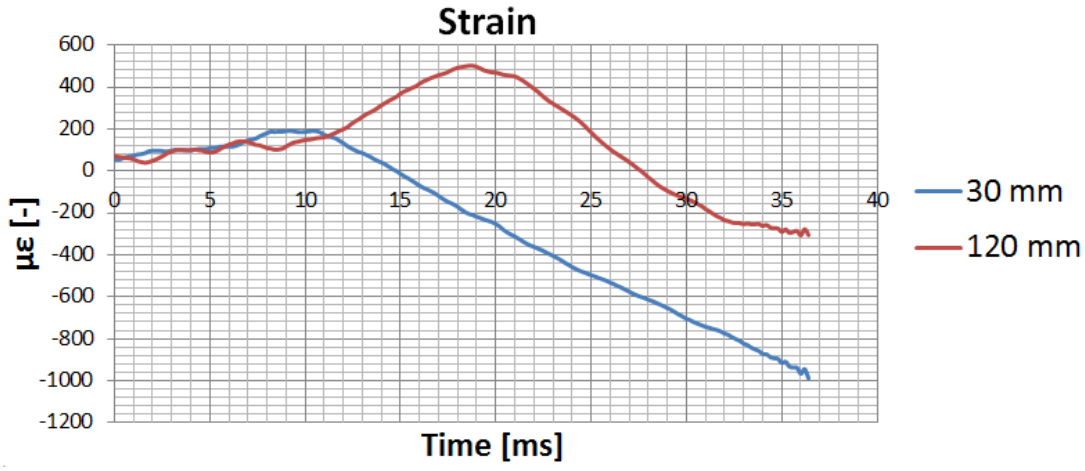

Figure 51 – Strains monitored at 30mm and 120mm from the wedge apex, β=30°.

Figure 52 shows the total vertical force on the wedge for the two different impact angles. It is seen that a higher angle yields a lower vertical force. It is also seen that the total vertical force is significantly lower than for the rigid case seen in for example Figure 37. As the wedge deforms, the effective impact velocity decreases and the impact angle increases, both of which lead to lower pressure peaks for impact problems.

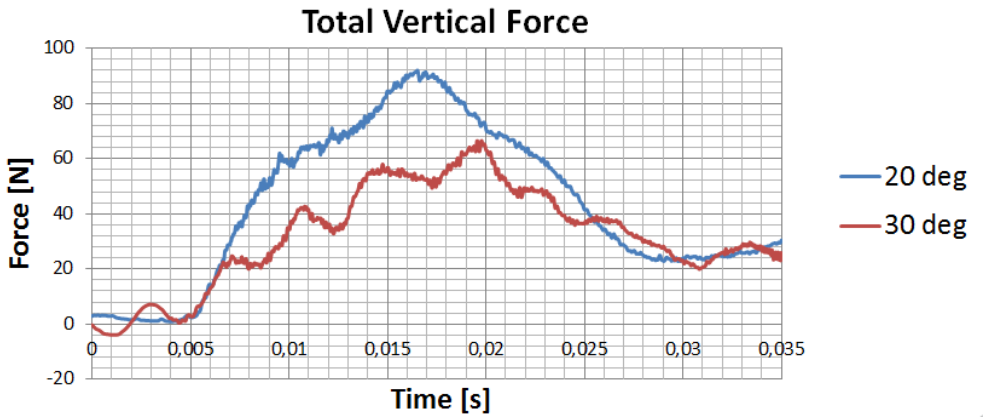

Figure 52 –Total vertical force on the wedge bottom for the 20° and 30° wedge.

There could be several reasons for the deviation between the simulation results and the experiment. For one, the box used in the experiment is rather small compared to the wedge, as was seen in Table 12. This implies that boundary conditions should have an effect on the results, as demonstrated in Figure 36. In this model, a rather large box has been used with no pressure limitations on the bottom boundary. This was done to avoid effects of the domain boundary, and also due to modeling convenience. With a mesh setup as the one used in this thesis, it would be difficult to impose a fixed depth of the domain, as the water is entering the domain from below. In hindsight, this may have been differently performed.

Also, the experimental setup uses plates with a width of 250mm in a box with a width of 800mm. This implies that 3-D effects in the experiment should be significant. Neglecting 3-D effects is generally considered to be conservative, meaning that 3-D slamming simulations should lead to lower pressures than 2-D slamming simulations (DNV, 2010). This is considered a contribution to the mismatch between the experiments and the simulations.

Finally, and most importantly, the co-simulation setup assumes constant velocity, whereas the experiment is conducted with freely falling wedges subjected to accelerations from both gravity and impact pressures. As can be seen in Section 3.1, the impact velocities decay to approximately one third of initial velocity after only 10ms. This is believed to be the main source of error when comparing the results.

The reason why this was done was partly because the effect of deceleration was underestimated initially and partly because of modeling convenience. As the scenario is modeled with a fixed wedge with water entering the domain from below, it is problematic to describe the inlet velocity accurately as a continuous function of the impact pressure. Alternatively, a prescribed velocity function based on an assumed deceleration can be adapted. This was in fact tried. However, as the wedge deceleration is very large compared to the gravitational acceleration, pockets of very low pressure arise at the velocity inlet as the inertia drives the water upwards and not enough

water enters the domain to fill the gap. This eventually leads to cavitation or pressure divergence altogether.

Indeed, this goes to show that the chosen model has some fundamental difficulties in describing even slightly complicated trajectories of the impacting body. It is seen that to give an accurate description of physical impacts, where the impacting object is accelerated in any degree of freedom, the DFBI-model should be chosen. This acknowledgement was reached at a late stage of the work with the master's thesis, and the time needed to set up such a configuration was considered to be too scarce. It is recommended that further work on FSI-problems should be conducted with an overset mesh-morphing DFBI-model as explained in Section 2.2.3.

4.4.4. Instabilities

During the initial co-simulations many simulations failed due to problems with the morphing mesh. One problem was the STAR CCM+ solver crashing due to too much vertex thinning. This was coped with by reducing the vertex thinning factor, which increases the accuracy of the mesh morpher along a surface. Distortion of the mesh was also a reason for many failed simulations, where the mesh boundaries were morphed out of their initial planes, quickly leading to pressure divergence. Divergence of the pressure field has in general been the largest problem for the FSI simulation. The morphing problems might have been smaller if an overset mesh were applied, with only the overset mesh morphing with the deformations.

Even when the mesh morpher was running smoothly, pressure divergence was seen for many simulations. This may be caused by the very strong coupling of the two physical domains. As the wedge is only 2mm thick and has a free end, deformations are very large and accordingly the fluid response to them, too. In fact, as will be shown in the next chapter, pinning the wedge leads to a significantly more stable simulation that converges for time steps in the same region as for the rigid wedge.

There could be some other reasons for the instability of the current setup. The Abaqus mesh could be a source of instability. Although convergent with respect to the deformations, the Abaqus grid is much coarser than the STAR CCM+ grid. This could lead to small-angled edges on the wedge boundary in STAR CCM+, that could trigger the divergence of the pressure field.

Another source could be the time-step simply needing to be extremely low to capture the effects expected from the experiment. In the experiment, cavitation and air pockets are seen on the wedge bottom as it starts to oscillate during water entry. The frequencies of these oscillations should be high. The current model does not even account for cavitation, and so it is possible that the governing physics are not sufficiently accurately captured.

5. PARAMETER STUDY ON HYDROELASTICITY

Simulations have been performed on a wedge built up by plates that are pinned at the ends as well as at the wedge apex, as seen in chapter 2.1.2. From a numerical point of view, this wedge will be more stable than the one seen in chapter 4, because the deformations will be smaller. Convergence tests with respect to time steps, domain size and under-relaxation factors are conducted. Parameter studies related to elasticity, coupling algorithm, structural solver scheme are presented and discussed.

5.1. Model

A pinned wedge is modeled in STAR CCM+ and Abaqus, as shown in Figure 53.

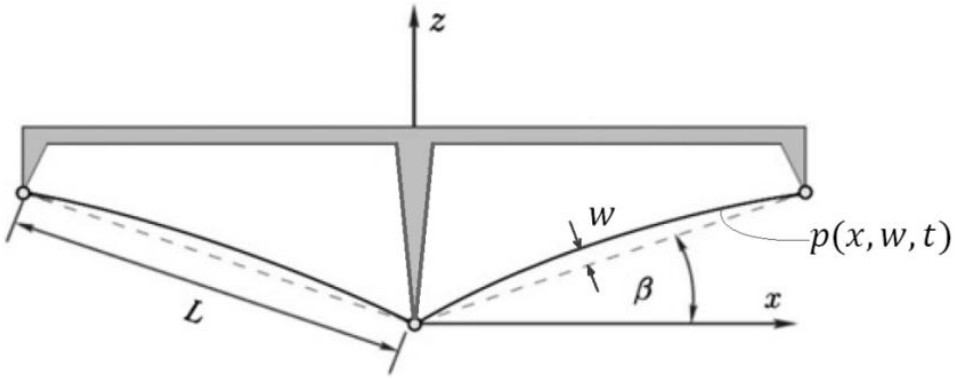

Figure 53 - Pinned-pinned wedge configuration.

Because the ends are now pinned, the wedge is modeled as a solid, triangular block with only the wedge-bottom set to FSI-boundary. This has some convenient implications. Only the bottom of the wedge will be deforming, posing less requirements to the mesh morpher, as well as to the time step. As the block encloses a fluid free region, the wedge bottom may be modeled with 2-D shell elements in Abaqus, as opposed to the free-end wedge, which was modeled with 3-D solid elements.

The geometry and mesh settings can be seen from Table 24 and Table 25. A thin 2x300mm plate is used also for these simulations, to investigate the hydroelastic impact of structures with nonlinear response. As free-fall lifeboats are often designed with thin composite walls that experience relatively large deformations, it is of interest to investigate the capabilities of the numerical method on this field. Physics and numerical properties are seen in Table 26.

Property	Value
Wedge length [m]	0.3
Wedge thickness [m]	0.002
Wedge angle [deg]	20
Impact velocity [m/s]	3

Table 24 – Water entry setup.

Property	Value
Domain height [m]	3
Domain width [m]	2
Domain depth [m]	0.005
Minimum cell height [m]	0.0004
Minimum cell width [m]	0.002
Number of cells	41252

Table 25 – Domain size and mesh setup.

Property	Value
Viscosity	No
Gravity	Yes
Compressibility	Yes
Convection discretization	2nd order
Time discretization	1st order
Velocity under-relaxation	0.9
Pressure under-relaxation	0.3
VOF under-relaxation	0.9
Nonlinear geometry (structure)	Yes

Table 26 – Solver setup.

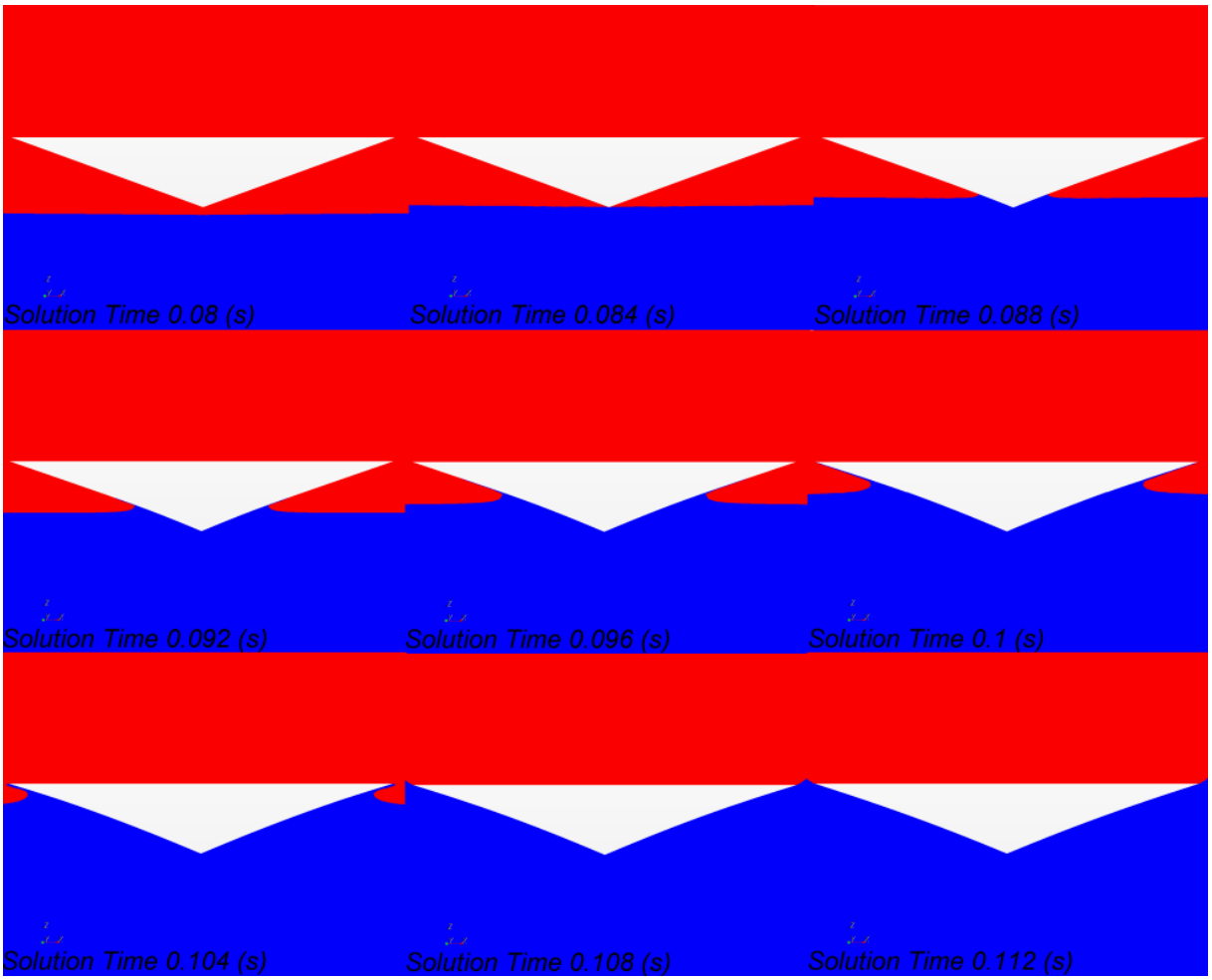

Figure 54 – Snapshots from a two-way coupled simulation of a pinned-pinned wedge.

5.2. Convergence tests

5.2.1. Time steps and iterations

Convergence tests with respect to time steps and inner iterations for the co-simulation are presented, this time from a structural point of view.

A case is set up with an aluminum wedge, with geometry and setup as described above. Different time steps and iteration setups are tried, and the von Mises stress at the upper midpoint of the wedge plate is monitored – 150mm from the wedge apex and 1mm from neutral axis. This is where the largest moments, stresses and deformations occur. The dry eigenfrequencies for the wedge plate are calculated in Abaqus and can be seen in Table 27.

Mode number	Frequency [Hz]
1	50.56
2	202.2
3	455.1
4	809.1
5	1264

Table 27 - Eigenfrequencies of the pinned aluminum wedge.

Figure 55 show the von Mises stress at the midpoint of the wedge plate for different time steps. It is seen that as for the rigid case, a time step of 0.0002s is sufficient to achieve convergence. Figure 56 shows the von Mises stress for different numbers of inner iterations. Figure 57 shows the von Mises stress for different numbers of inner iterations per exchange. Inner iterations per exchange refer to the number of inner iterations in the CFD-code between each inclusion of Abaqus. It is seen that the difference is minimal between the different setups for inner iterations and for the number of inner iterations per exchange. This is understood by considering that these parameters do not really govern the physical solution. If the number of inner iterations is too low, or the number of inner iterations per exchange is too high, a small inaccuracy in the result is not what is seen, but rather a large and sudden divergence of the entire solution. This has been the case for a number of attempted simulations, and the parameters are chosen accordingly.

Two stress peaks at approximately 0.013s and 0.027s after simulation start are recognized. They correspond to the first eigenmode. The reason that the peaks are separated by less than the expected 0.02s is believed to be related to additional stiffness arising from large deformation. The local variations of the stress curve correspond well with the second eigenmode of the plate.

An important conclusion to draw from these comparisons is that a stable and convergent result has been found with a relatively small amount of additional computation time, compared to the rigid wedge case. This is encouraging with respect to use of the method in later works.

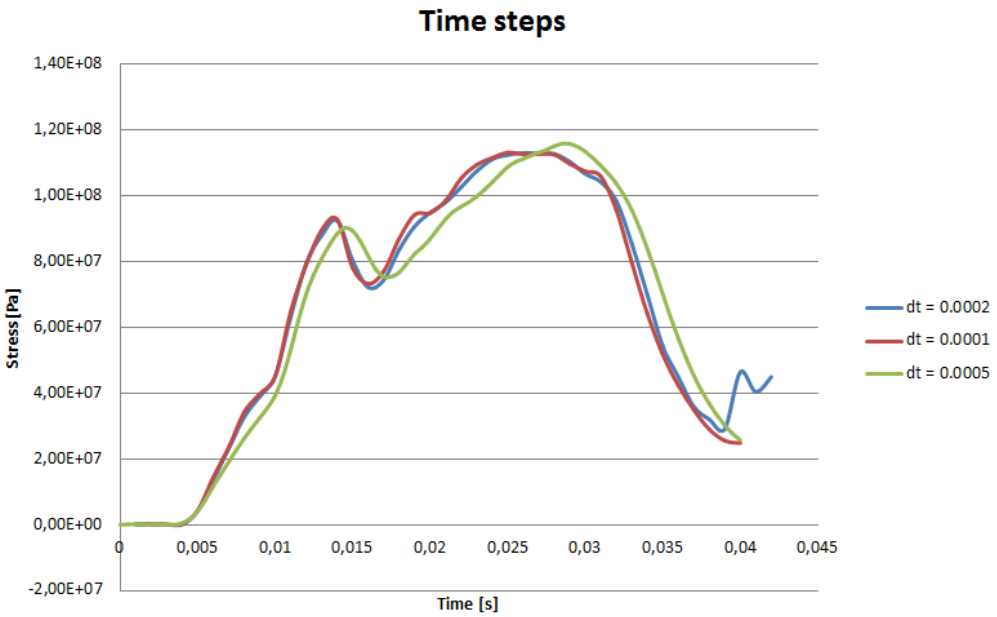

Figure 55 – von Mises stress at the midpoint of a wedge side (150mm from the wedge apex) for various time steps.

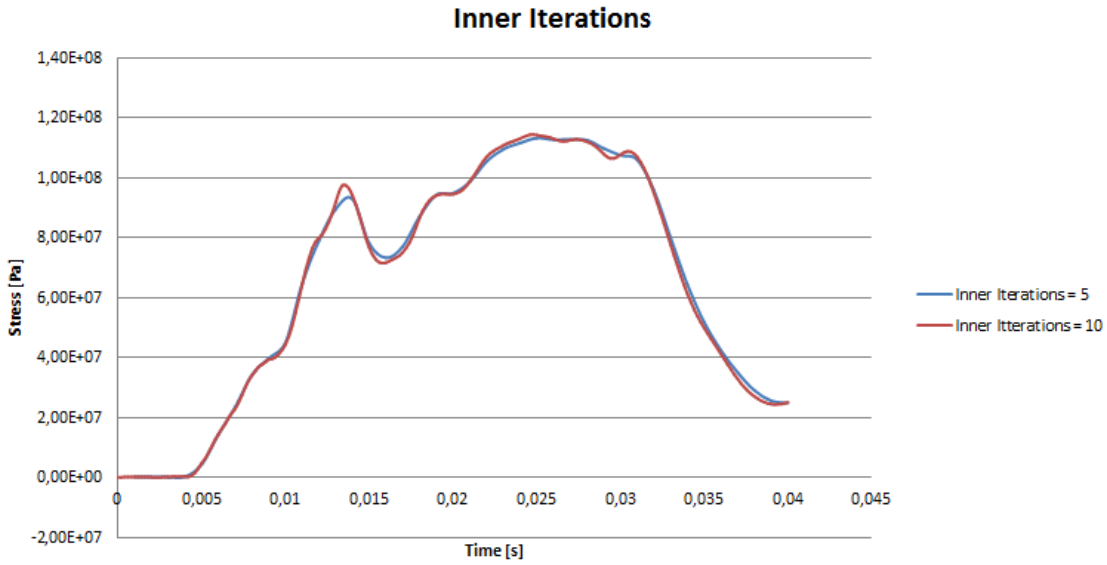

Figure 56 – von Mises stress at the midpoint of a wedge side (150mm from the wedge apex) for various numbers of inner iterations.

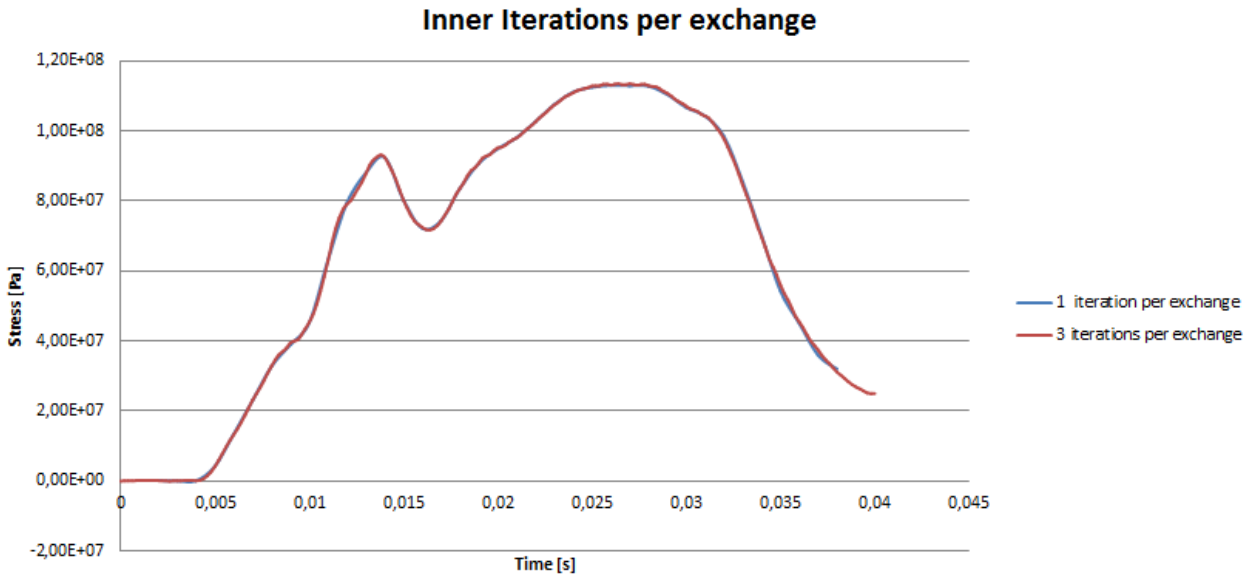

Figure 57 - von Mises stress at the midpoint of a wedge side (150mm from the wedge apex) for various numbers of iterations per exchange.

5.2.2. Imported Fields under-relaxation factor

The deformation field is imported from Abaqus to STAR CCM+, and applied to the FSI-boundaries at each time step. The imported field can be under-relaxed in STAR CCM+. The reason for this would be to stabilize the CFD-solution in cases of large sudden deformation. The effect of varying this under-relaxation factor has been investigated for the pinned aluminum wedge.

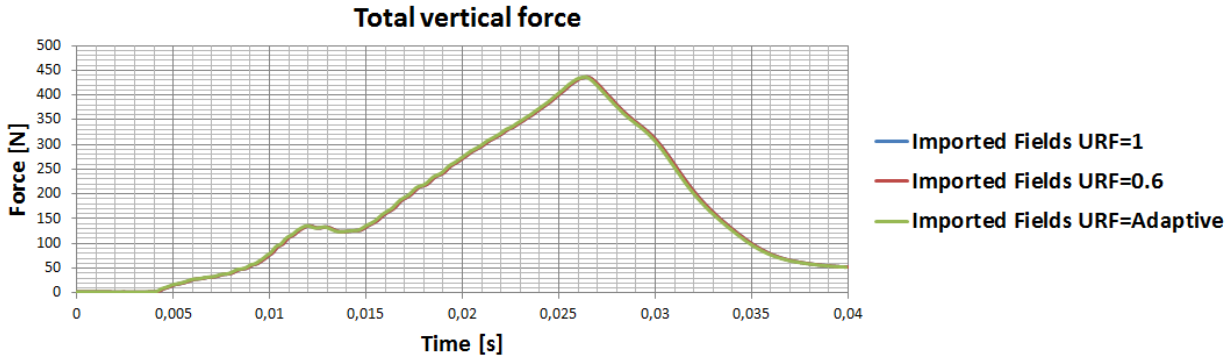

Figure 58 – Total vertical force on the wedge bottom for different imported field under-relaxation factors.

Figure 58 shows the total vertical force on the wedge bottom for different imported field under-relaxation factors. The effect of varying the imported field under-relaxation factor is seen to be negligible, as the different simulations agree completely. The default setting in STAR CCM+ is the adaptive under-relaxation factor. This is therefor used in the co-simulations.

5.2.3. Grid flux under-relaxation factor

The fluid response to the wedge deformations is based on the grid flux of the FSI boundary (see Section 2.5.3). The grid flux is the volume swept by the deformation of the wedge between two time steps. The fluid experiences an impulse due to the deformation, which in turn leads to changes in pressures and velocities.

The grid flux may be under-relaxed. This is done to stabilize a solution where the dynamic between deformations and fluid responses becomes unstable. This effectively neglects a fraction of the fluid response to the deformations. The effect of varying the grid flux under-relaxation factor has been investigated.

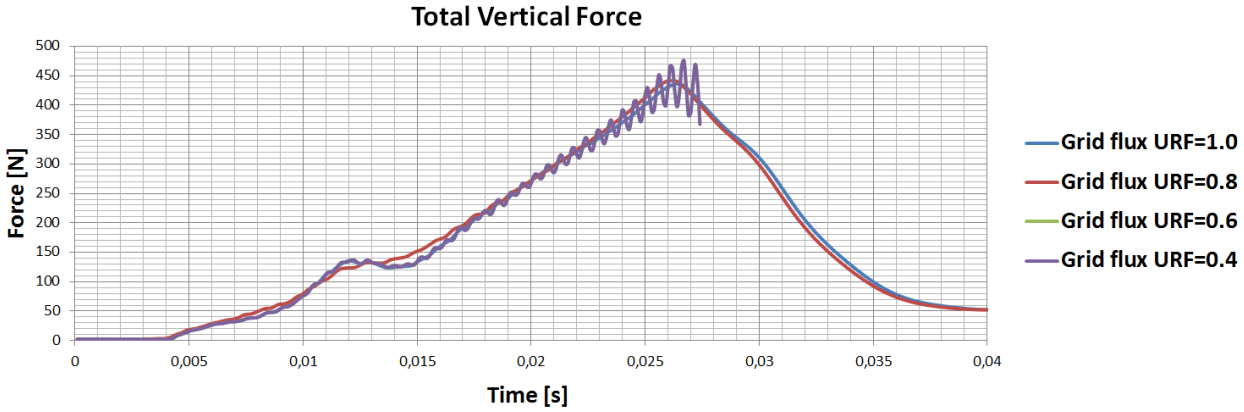

Figure 59 - Total vertical force on the wedge bottom for different grid flux under-relaxation factors.

Figure 60 shows the total vertical force on the wedge bottom for different grid flux under-relaxation factors. Curiously, it is seen that instabilities occur for the lower grid flux under-relaxation factors, i.e. 0.4 and 0.6 (They agree perfectly in the plot). The divergence is significant, and the last 15ms of simulation for these two cases are left out, for visual convenience. It is concluded that the grid flux should not be too strongly under-relaxed for the impact problem.

The divergence could come from precisely the bad correspondence between true deformations and fluid response. If so, it is not a proper tool to stabilize a strongly coupled problem. The parameter would be better suited to stabilize steady state hydroelasticity problems.

5.2.4. Structural nonlinearity

In Section 4.3.3, it was seen that nonlinear structural effects were negligible for the clamped wedge plate. This was explained by acknowledging that neither updated stiffness nor load appliance changed the fact that the boundary conditions did not allow for axial forces to develop. For the pinned beam, however, a nonlinear analysis should lead to an additional stiffness in the plate. This is investigated by observing the stress variation through the thickness of the wedge for a nonlinear analysis, as well as by running a full two-way coupled analysis with linear geometry.

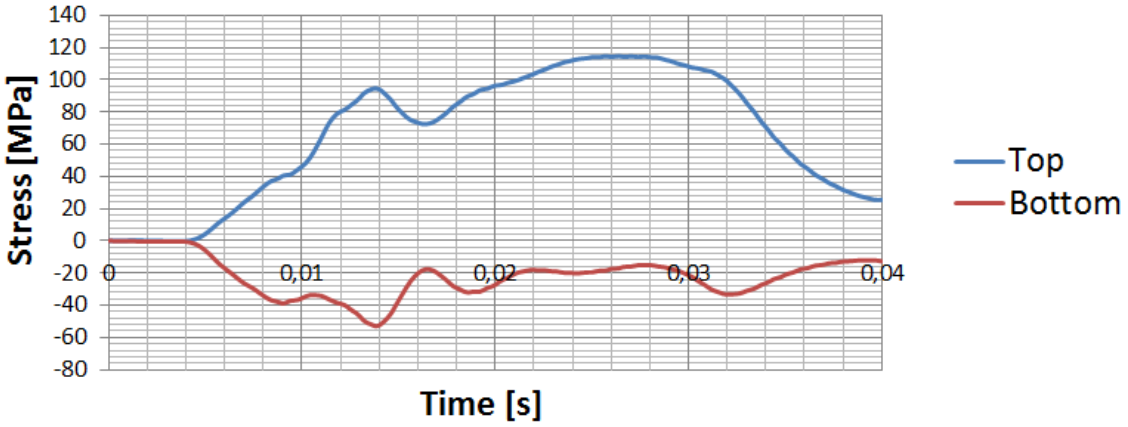

Figure 60 – Stress in the longitudinal direction at the top and bottom integration point at the midpoint of the wedge, for a two-way coupled simulation with nonlinear geometry.

Figure 60 shows the stress in longitudinal direction for the nonlinear analysis over time. The Top and Bottom lines refer to monitoring at the top and bottom integration point of the shell element. In a linear analysis these lines should be symmetrical with opposite signs. In this case it is seen that the bottom integration point has significantly lower absolute values than the top integration point. This implies that the nonlinear membrane stress contributes significantly to the results.

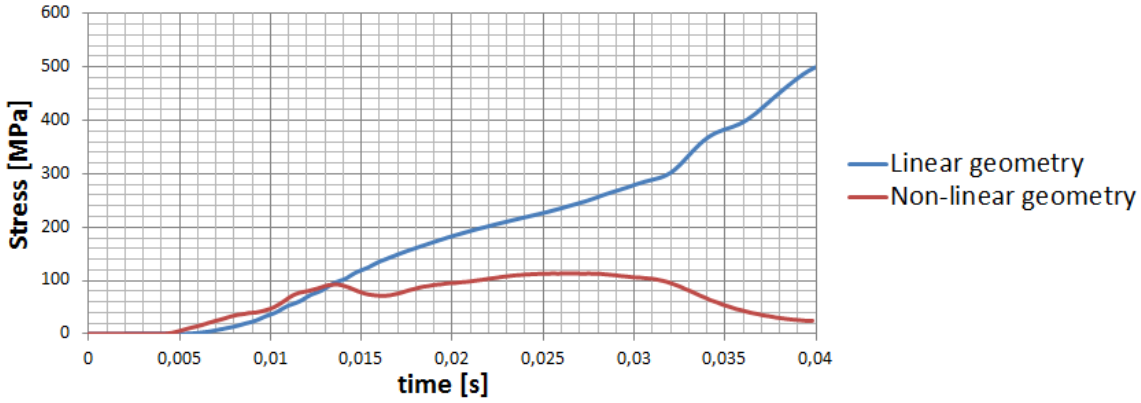

Figure 61 - von Mises stress at the midpoint of the wedge, for a two-way coupled linear analysis and a two-way coupled nonlinear analysis.

Figure 61 shows the maximum midpoint von Mises stress for a full two-way coupled analysis with nonlinear effects enabled and disabled. It is seen that the linear analysis reaches levels of stress multiple times higher than the nonlinear analysis. When deformations occur, the nonlinear analysis updates the geometry, allowing for large membrane forces that limit the deformations.

The effect of nonlinearity will be dependent on the stiffness and the slenderness of the structure. In this case, the effect is so important that the linear analysis is considered worthless from a

physical point of view. A visualization of the difference can be appreciated in Figure 62, where snapshots from STAR CCM+ illustrate the deformed wedge.

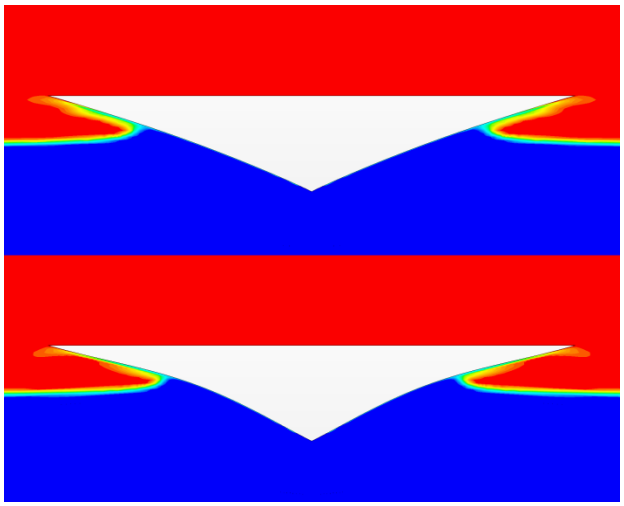

Figure 62 - Snapshots during the water entry. Top - Nonlinear geometry in Abaqus enabled, Bottom – Nonlinear geometry in Abaqus disabled.

5.2.5. One-way coupling

A one-way coupled analysis has been performed on the wedge, and the results are compared with the two-way coupled analysis. With one-way coupling it is meant that the pressures are being exported from STAR CCM+ to Abaqus, but the deformations are not imported back. This is therefore the equivalent of running a rigid analysis and applying the pressures as a dynamic load history.

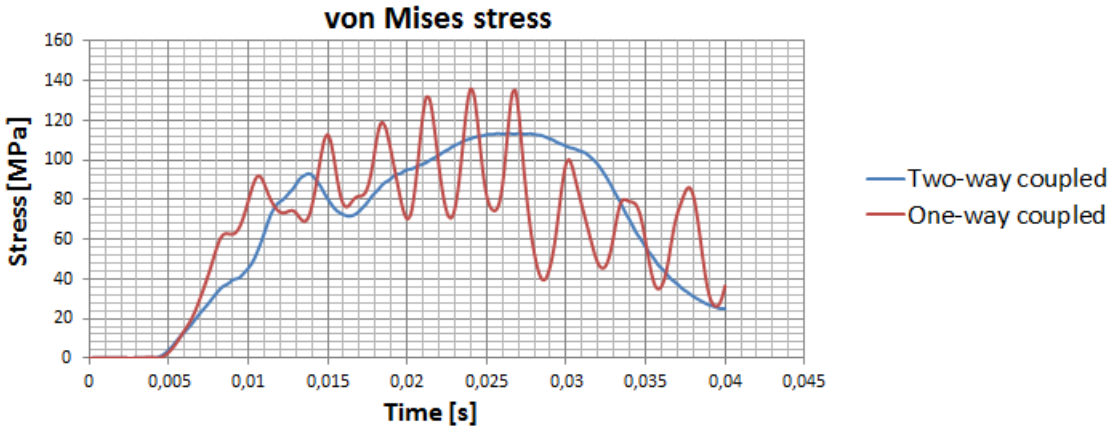

Figure 63 – von Mises stresses at the midpoint of the wedge, for a two-way coupled analysis and a one-way coupled analysis.

Figure 63 shows the von Mises stress for the two analyses. It is seen that the one-way coupled simulation shows large oscillations at a higher frequency than the two-way coupled simulation. The dominating frequency of oscillation appears to be approximately 400 Hz. This does not

correspond well with any of the eigenfrequencies. The reason for this is believed to be an additional nonlinear stiffness that comes from the large deformation and added membrane forces, leading to a stiffer system with altered and higher eigenfrequencies. Note that the stress from the two-way coupled simulation acts as a mean to the one-way coupled simulation. This implies that the higher order oscillations of the wedge are damped, or not even excited, in the two-way coupled analysis.

5.3. The wetting time quotient

5.3.1. Varying natural frequencies

In the theory of hydroelasticity, the relation between wetting time and the lowest eigenperiod of the system was seen to be an important parameter. The wetting time is defined as the time from initial submergence to full submergence of the system, in this case the wedge. To investigate this relationship, a series of coupled analyses has been performed. The wetting time quotient is defined as

$$WQ = \frac{t_{wet}}{T_1} \qquad \text{Eq. 5.1}$$

where t_{wet} is the wetting time and T_1 is the first eigenperiod of the system. For a pinned-pinned wedge entering water at constant velocity, the wetting time is given as a function of geometry and impact velocity. The wetting time is expressed as

$$t_{wet} = \frac{Ltan\beta}{V} \qquad \text{Eq. 5.2}$$

where L is the length of the wedge, β is the wedge angle and V is the initial impact velocity. The lowest natural frequency for a pinned-pinned beam is defined as

$$f_e = \frac{1}{2\pi}\left(\frac{\pi}{L}\right)^2 \sqrt{\frac{EI}{m}} \qquad \text{Eq. 5.3}$$

where m is the weight per meter of the wedge. By changing the Young's modulus of the material, systems with different wetting time quotients are obtained. It is expected to see a large difference in response for wedges with an eigenperiod lower than the wetting time, i.e. $WQ < 1$, and a more quasi-static response for the cases with $WQ > 1$. Table 28 shows the range of wetting time quotients chosen for the coupled analyses.

Young's modulus [GPa]	Eigenfrequency [Hz]	WQ [-]
2.885	10.41	0.25
11.54	20.83	0.5
25.96	31.25	0.75
46.16	41.66	1
72.13	52.08	1.25
103.8	62.50	1.5
184.1	83.33	2
1154	208.3	5
4616	416.6	10

Table 28 – Resulting eigenfrequencies and necessary Young's moduli to obtain a given wetting time quotient for the wedge.

The simulations have been run, varying the time step according to the magnitude of the deformations. It was seen that for the systems with higher stiffness, the time step could be set to 0.2ms, as for the rigid case. For the systems with a low stiffness, the time step was lowered to 0.02ms to achieve convergence. This illustrates the fragile nature of the coupling algorithm.

5.3.2. Deformations and strains

Figure 64 shows the vertical displacement at the midpoint of the wedge plate (150mm from wedge apex) for different wetting time coefficients. The upper plot shows the displacement normalized with respect to the wedge thickness, and the lower plot shows the displacement with a correction for Young's modulus dependency. One should recall that the wedge is very slender, with a thickness of $t = 2mm$, a length of $L = 300mm$, and accordingly a slenderness ratio of $L/t = 150$. Therefore it is not unexpected to see large relative deformations. Note that $u_{max} \propto E^{-1/3}$.

Figure 65 shows the strain at the midpoint of the wedge plate for different wetting time coefficients. The upper plot shows the monitored strain and the lower plot shows the strain with a correction for Young's modulus dependency. Note that $\varepsilon \propto E^{-1/2}$.

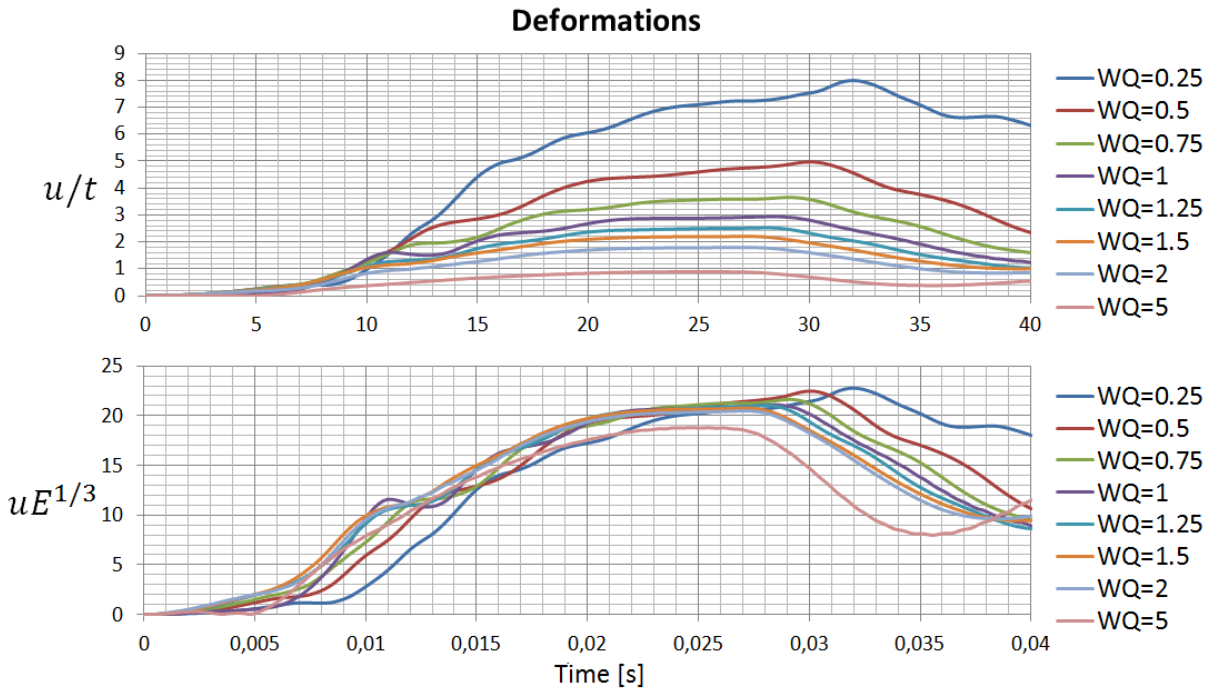

Figure 64 – Deformations at the midpoint of the wedge for two-way coupled simulations. Top – Deformations divided by the thickness of the wedge plate. Bottom – Deformations corrected for dependency to Young's modulus.

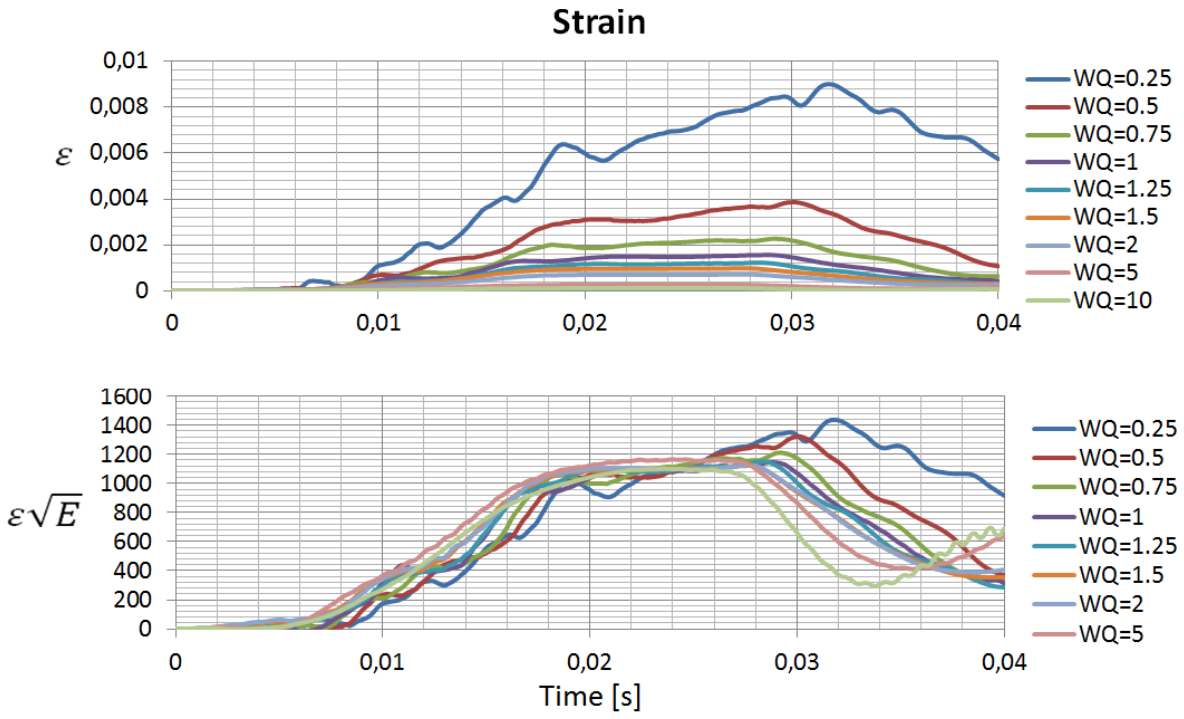

Figure 65 – Strains at the midpoint of the wedge for two-way coupled simulations. Top – Strains. Bottom – Strains corrected for dependency to Young's modulus.

As discussed in Section 2.1.3, linear beam theory implies that $u_{max} \propto E^{-1}$ for a quasi-static case. This is obviously not the case here. The nonlinear, quasi-static beam/catenary theory implies a nonlinear relationship between u_{max} and E. This is understood by recognizing that the catenary approximation assumes a linear relationship between the wedge plate elongation and the Young's moduli through the cinematic compatibility assumption, i.e. $\Delta L \propto E$, and at the same time observing that ΔL relates nonlinearly to u_{max} through the analytically unsolvable arc length integral of the sine approximation for u. Although a cushioning effect is expected to be seen on the pressures from the varying Young's moduli, such a well agreeing relationship between the maximum strains and the square root of the Young's moduli is surprising. The nature of the force distribution in the wedge is further investigated in the following.

5.3.3. Structural nonlinearity

The axial fraction of the response can be seen by considering Figure 66.

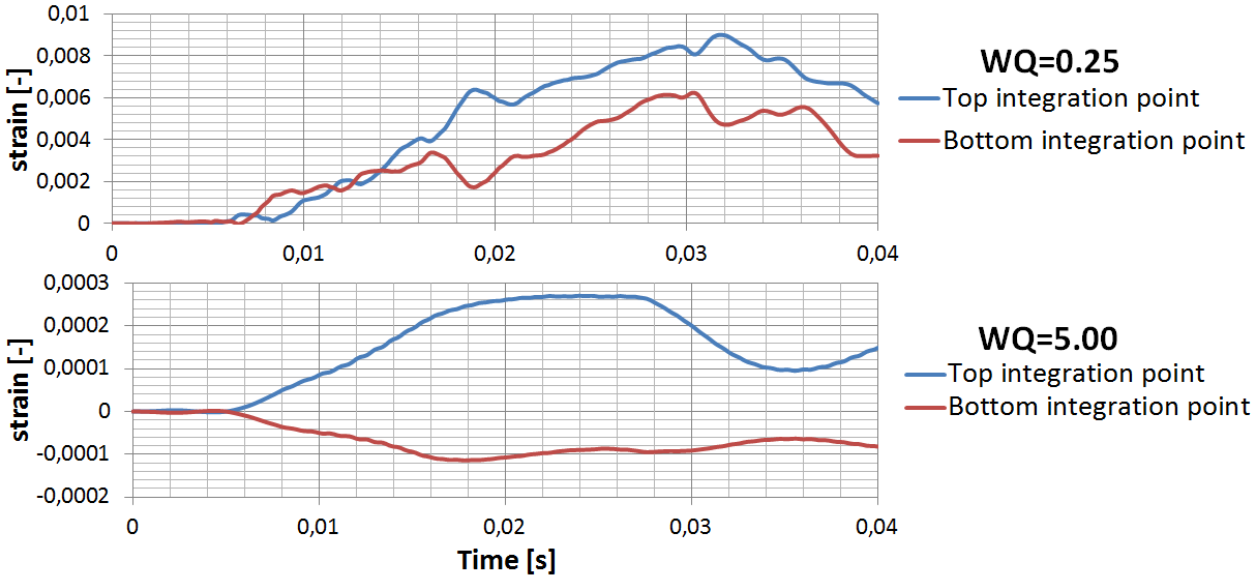

Figure 66 - Strain at the top and bottom integration point at the midpoint of the wedge for a two-way coupled simulation. Top plot – WQ=0.25. Bottom plot – WQ=5.00.

It is seen that for the WQ=0.25 case, the strains are positive throughout the water impact. This implies that the bending stiffness forces are dominated by the membrane forces. For the WQ=5.00 case the internal forces are distributed more evenly between axial and bending contributions. The conclusion to be drawn from this is that the response of the wedge is dominated by axial membrane forces in the wedge for almost all the WQs tried.

Figure 67 shows the pressure coefficient for different instants throughout the water impact for WQ=0.75. It is seen that the pressure coefficient grows steadily with a characteristic slamming distribution, until the entire wedge is submerged at approximately t=0.030s, and the pressure

coefficient decays gradually. The gradually growing pressure coefficient is in conflict with the rigid water entry presented in Section 2.1.1, where analytical solutions point towards a constant maximum value of C_p that moves along the wedge bottom with time. This difference is believed to be associated with the fact that the wedge is initially deforming, leading to a lower effective impact velocity, and subsequently a lower pressure. As the maximum deflection of the first deformation period is reached, the internal forces in the wedge plate make an addition to the counterforce of the pressure, and the coefficient grows to values that are larger than for a rigid wedge. As has been seen, these forces appear to be dominated by the membrane terms.

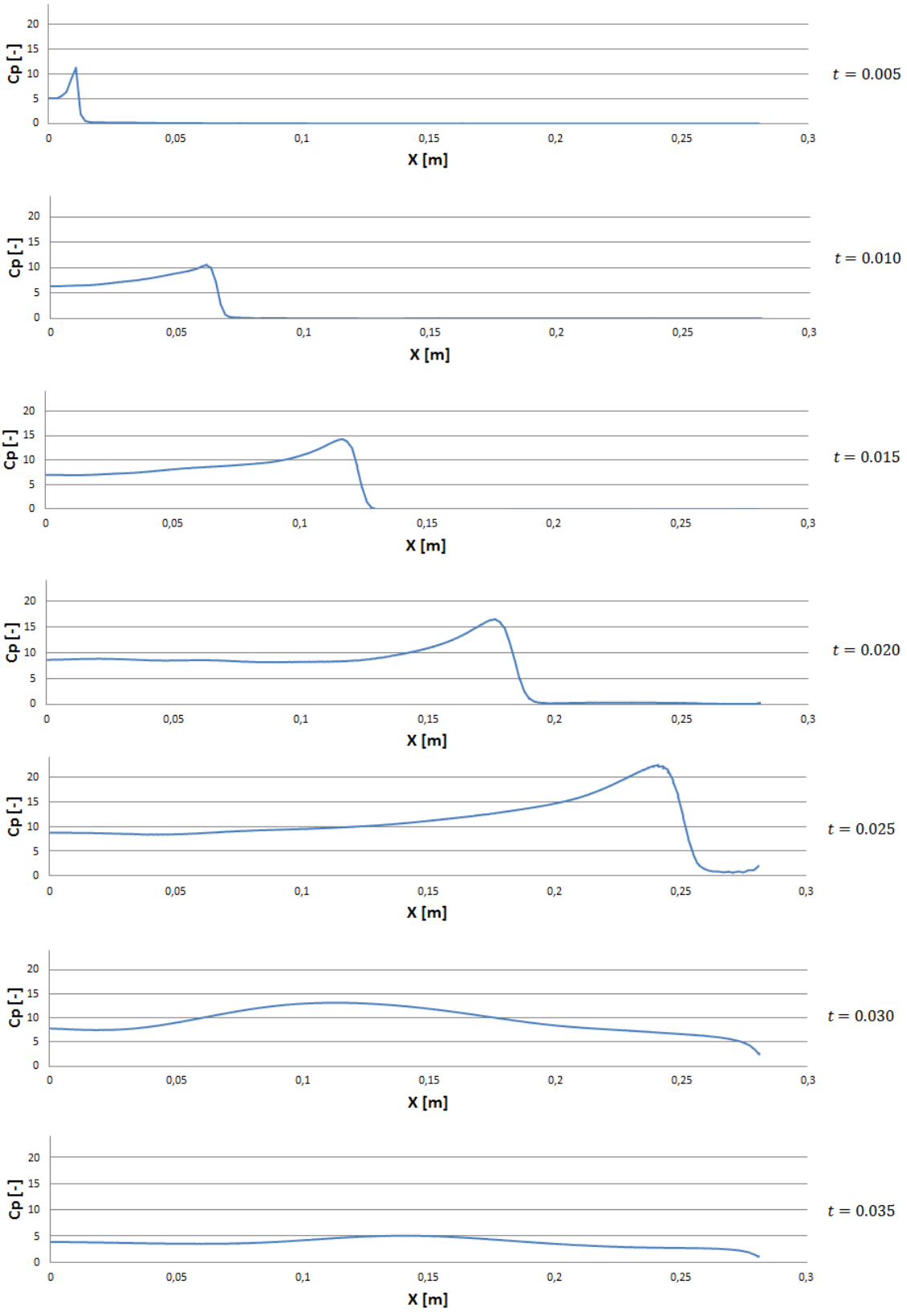

Figure 67 - Pressure coefficient on the wedge bottom for different time instants throughout the water impact for a two-way coupled simulation with WQ=0.75.

Figure 68 shows the total vertical force on the wedge for different wetting time quotients. The total vertical force for the all the wetting time quotients can be seen in APPENDIX A. The force displays a linear growth for the rigid wedge, but the elastic wedges show an increasingly exponential behavior with a decreasing Young's modulus. This is consistent with the conclusions drawn from evaluating the pressure coefficient time history. It is seen that the force significantly exceeds the rigid wedge case for the cases with low stiffness. As the wetting time quotient grows, the stiffness grows accordingly, and the vertical force of the coupled simulation converges towards the rigid case.

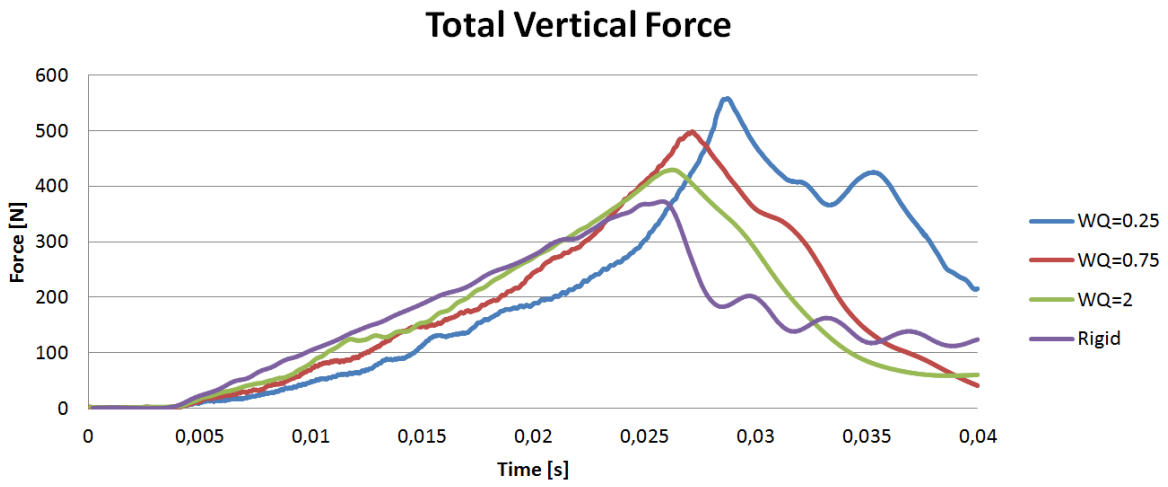

Figure 68 - Total vertical force for different wetting time quotients.

5.3.4. Hydroelastic amplification

Based on the maximum total force F_{max} from Figure 68, an equivalent pressure is defined as

$$p_{eq} = \frac{F_{max}}{BL} \qquad \text{Eq. 5.4}$$

where B is the width of the wedge and L is the length. This pressure is an evenly distributed pressure that results in a total force F_{max} when integrated over the wedge bottom. The degree of dynamical behavior in the problem can now be assessed by applying an equivalent pressure on the wedge bottom and conduct a quasi-static analysis in Abaqus. Table 29 shows the equivalent pressures calculated with Eq. 5.4.

WQ	**0.25**	**0.50**	**0.75**	**1.00**	**1.25**	**1.50**	**2.00**	**5.00**	**Rigid**
Maximum vertical force [N]	558	536	498	462	463	441	429	407	373
Equivalent pressure [kPa]	62.0	59.6	55.4	51.4	51.6	49.1	47.7	45.2	41.4

Table 29 – Equivalent pressures.

Quasi-static analyses of the wedge plate subjected to the equivalent pressure have been conducted in Abaqus. Figure 69 shows the response for the two-way coupled simulation compared to the response of the static analysis with an evenly distributed equivalent pressure.

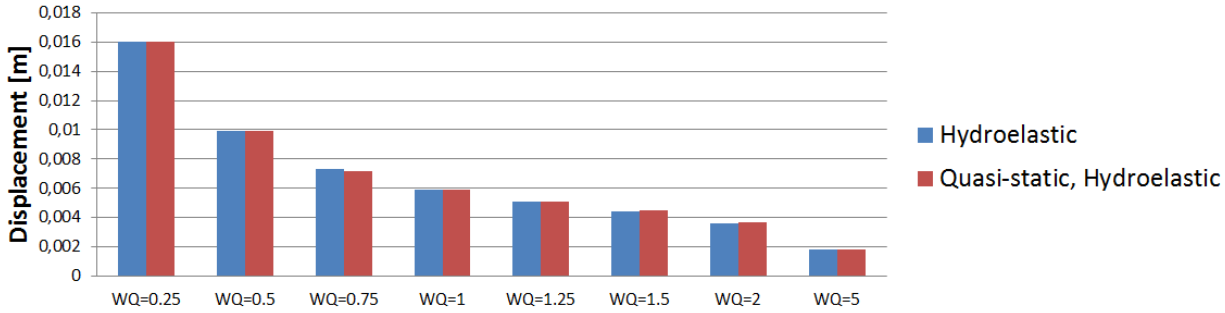

Figure 69 - Comparison between maximum wedge displacement at the midpoint of the wedge for a two-way coupled simulation and a quasi-static FE-analysis with hydroelastic equivalent pressures.

The comparison shows an almost identical response behavior. This does not imply that the problem can be analyzed quasi-static. The dynamics of hydroelasticity are implicitly accounted for because the pressures are derived from hydroelastic simulations. The figure does, however, show us that the even distribution of the equivalent pressure is a satisfactory representation of the impact pressure for this particular case.

Now consider Figure 70, where the quasi-static responses have been calculated using only the equivalent pressure from the rigid wedge case and applying it on the wedges with varying Young's moduli. It is seen that the hydroelastic response is greater for every wetting time quotient.

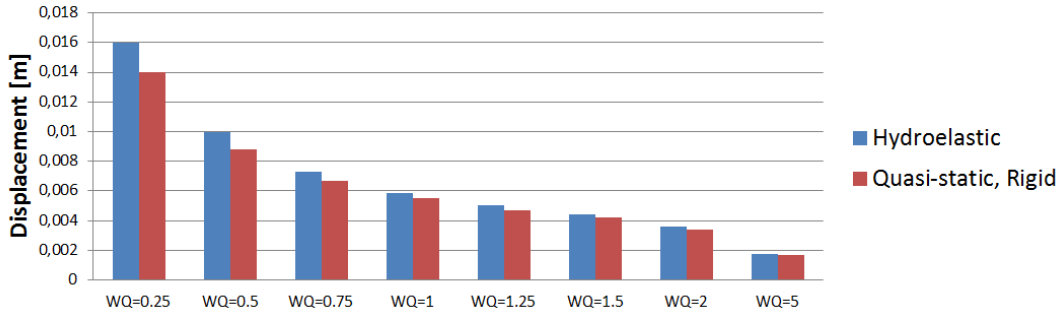

Figure 70 - Comparison between wedge displacements at the midpoint of the wedge for a two-way coupled simulation and a quasi-static FE-analysis with rigid impact equivalent pressures.

A *hydroelastic amplification factor* is now defined as

$$HAF = \frac{u_{hydroelastic}}{u_{rigid}} \qquad \text{Eq. 5.5}$$

where $u_{hydroelastic}$ refers to the maximum deformation for a hydroelastic simulation, and w_{rigid} refers to the quasi-static deformation for the rigid wedge equivalent pressure. Figure 71 shows the hydroelastic amplification factor for the different wetting time quotients.

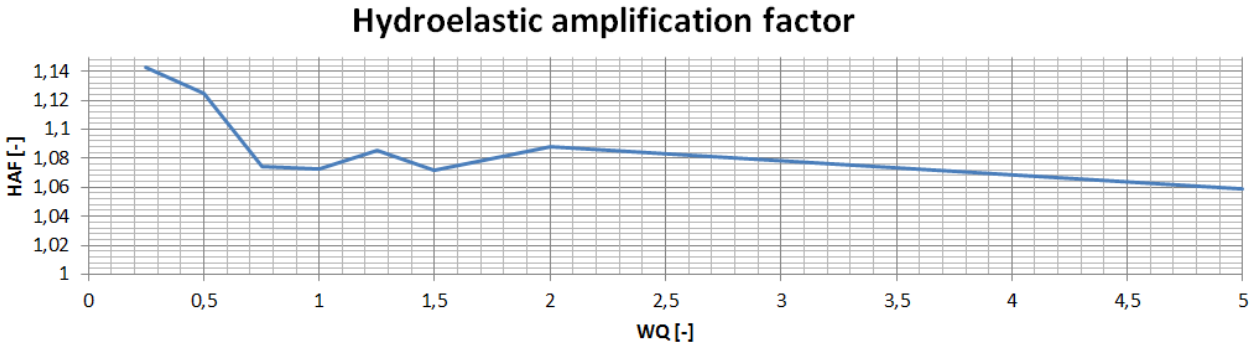

Figure 71 - Hydroelastic amplification factor

We arrive at a remarkable conclusion for the simulations of the elastic wedges analyzed in this section. The maximum structural responses from the dynamic, two-way coupled analyses are larger than the quasi-static responses to the highest pressures found in a rigid body analysis. This contradicts the assumption that the cushioning leads to a lower maximum response. In DNVs recommended practices (DNV, 2010) it is explicitly stated that it is considered conservative to neglect the effect of hydroelasticity. But these results indicate that if deformations are sufficiently large, and nonlinearity in the structural response is significant, the pressures may exceed those of a rigid body analysis and lead to higher strains and deformations.

For a last remark to the deformations, see Figure 72 and Figure 73. The maximum deformation has been computed based on the theoretical expressions proposed in Section 2.1.3 on nonlinearity, and compared to the static FE-analysis with equivalent pressures from the rigid wedge water entry. The beam theory approach and linear Abaqus solutions agree very well, and both lead to extreme over-predictions of the displacement, with $\frac{u}{L} > 0.5$. The simplified catenary theory approach shows surprisingly good agreement with the nonlinear Abaqus solutions, but slightly over-predicts the displacement. This is explained by recognizing that the bending stiffness is neglected, and the contributions from bending stiffness are expected to be present, although small for low-stiffness bodies. Additionally, the sine curve approximation to the catenary deformation is inaccurate, as the analytical solution to the catenary is actually a hyperbolic sine function, which gives slightly higher angles at the ends, and accordingly leads to a lower maximum deformation. Nevertheless, it is seen that a zero-stiffness approximation shows good agreement with the quasi-static, nonlinear Abaqus-deformations.

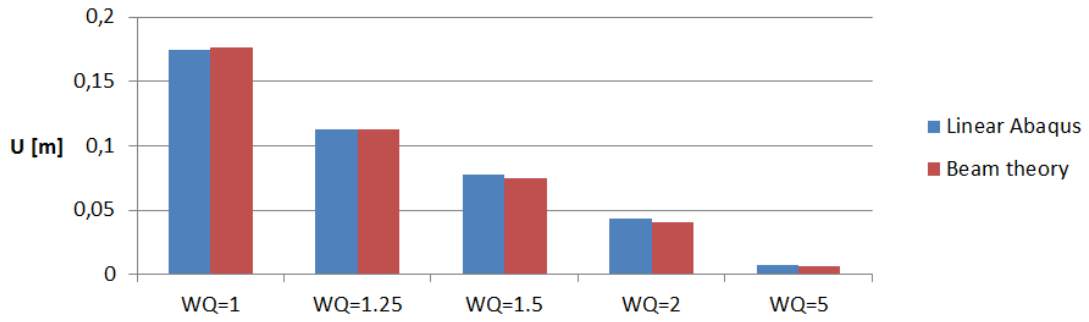

Figure 72 - Maximum deformations calculated with linear FEM and linear beam theory. The deformations are calculated statically based on the equivalent pressure from the rigid wedge simulations.

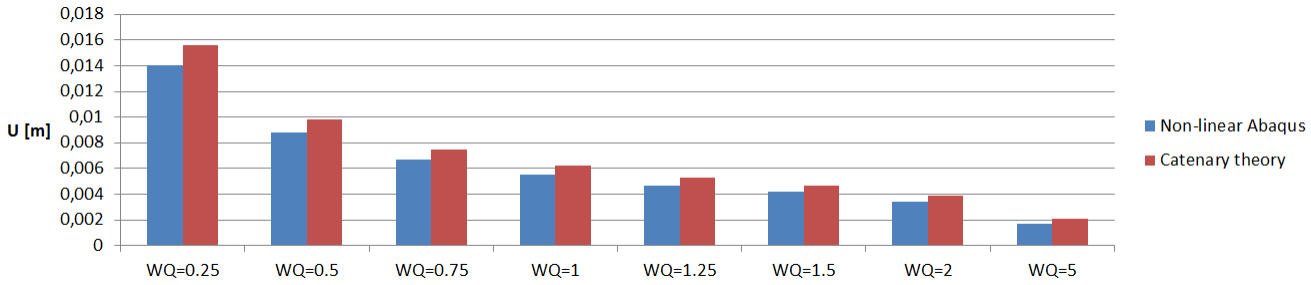

Figure 73 - Maximum deformations calculated with nonlinear FEM and nonlinear catenary theory. The deformations are calculated statically based on the equivalent pressure from the rigid wedge simulations.

5.3.5. One-way and two-way coupling

One-way coupled simulations have been run for the different wetting time quotients, for comparison to the two-way coupled simulations. Results from the one-way coupled simulations are seen in Figure 74. The deformations are corrected for dependency to the Young's moduli and divided by the plate thickness. Comparison between one-way coupled results and two-way coupled results for each wetting time quotient can be seen in APPENDIX B.

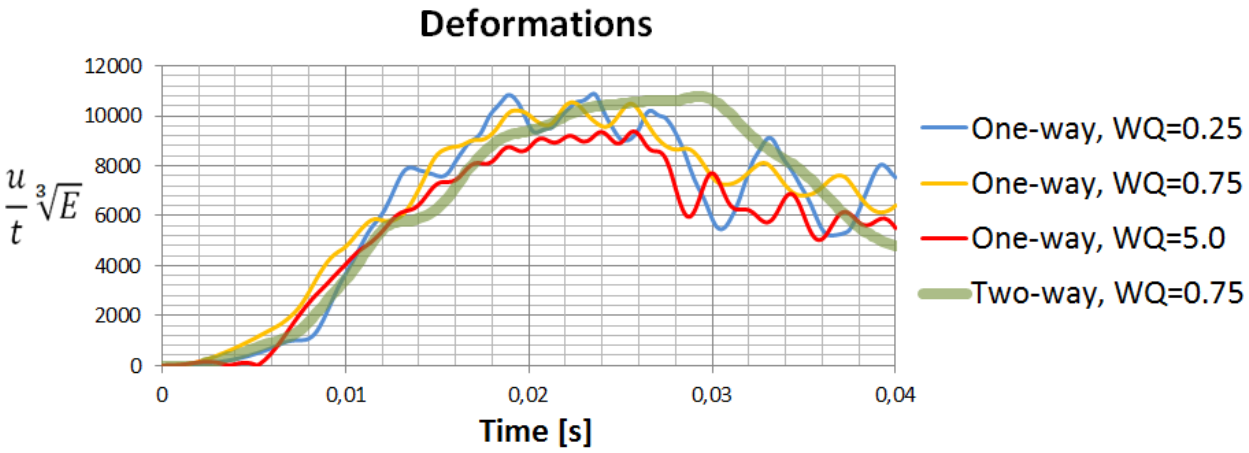

Figure 74 - Deformations at the midpoint of the wedge for one-way coupled simulations. The deformations are divided by the thickness of the plate, and corrected for dependency to the Young's moduli.

We recognize an oscillatory behavior for the one-way coupled simulations, with a low frequency for $WQ = 0.25$ and a high frequency for $WQ = 5.0$. This is expected, considering the stiffness variations. We also recognize that the two-way coupled deformations act as an arithmetic mean to the one-way coupled simulations. We see that the maximum deformation for the two-way coupled case is larger than then the corresponding one-way coupled case. This is yet another illustration of the large maximum pressures that come with large non-linear responses. It would be interesting to investigate the possibility of assessing the agreement between two-way coupled responses and the low-pass filtered, one-way coupled responses, but this has not been done, due to time considerations.

5.3.6. Deformation velocities

Figure 75 shows the magnitude of the displacement velocity throughout the water entry for different wetting time quotients. Deformation velocities for all the runs can be seen in APPENDIX C. The water impact occurs at approximately 5ms after monitoring has started. It is seen that the deformation velocity quickly rises to magnitudes that are large compared to the impact velocity of 3 m/s. For the WQ=0.25 case the deformation velocity approaches 2m/s. This implies a significant reduction in effective impact velocity, leading to the lower pressures as was seen in Figure 67. As submergence continues the displacement velocities go down (approximately between 15ms and 20ms after initialization). This is associated with the deformation state where large deformations have been reached, and the added axial stiffness prevents the wedge from further deformation. This is also the time instance where the pressure coefficient grows largest. At approximately 30ms after initialization, a slight increase is seen in the velocity magnitude. This is associated with the end of the submergence phase, where impact pressures gradually fade towards the hydrodynamic pressures of constant velocity vertical movement in water.

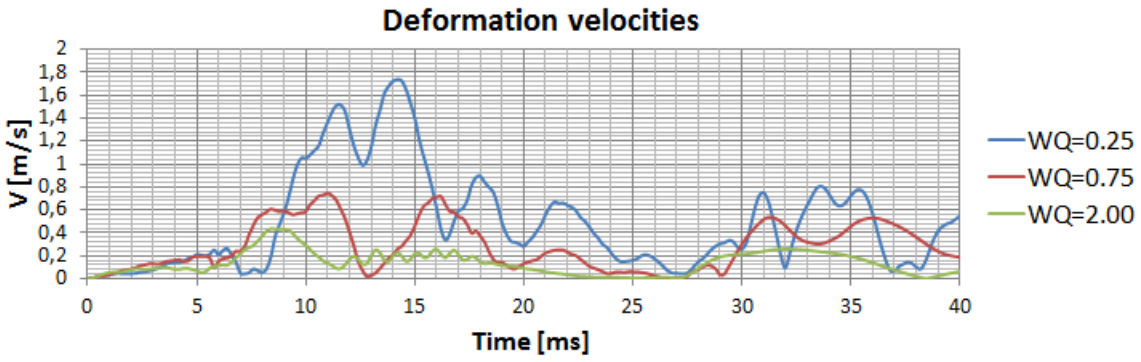

Figure 75 - Deformation velocity magnitude at the midpoint of the wedge for different wetting time quotients.

6. DISCUSSION

Some of the choices and results from this work are discussed and elaborated in the following.

The results from the rigid wedge simulations in Chapter 3 in STAR CCM+ agree well with previous results. The capabilities of the numerical model are found to be robust for the rigid body impact. It would have been interesting if more impact velocities and impact angles could have been included. The reason for the initial presence of oscillations in the total force remains unclear, but it is believed to be related to poor initialization of the fluid domain. As was seen, these oscillations were avoided as the experience with the program grew. The finding that viscosity may be excluded altogether is interesting, although expected. For different geometries, where the water separation point is of importance, the viscosity should not be excluded (Larsen, 2013). Also, it could be argued that because the jet behavior depends on the viscosity setting, and the structural response depends on a correctly expressed wetted surface with regard to added mass, viscous effects could be of importance.

In Chapter 4, the numerical model is compared to experimental data. Substantial deviations are found between calculations and measurements, particularly for smaller deadrise angles. It is believed that the main reason for this is related to the constant velocity assumption. Different boundary conditions and the presence of three-dimensional effects may also contribute to the deviation. Due to the very large flexibility of the experimental model, air pockets and cavitation could also be important. From an industry application point of view, the varying velocity and three-dimensional effects are most relevant to include in future calculations.

The experiment chosen has some limitations in its ability to verify the FSI-simulations. Firstly, the physics observed in the experiment include large relative deformations, which are found to be challenging to capture by the numerical model. Secondly, the slenderness of the wedge plate leads to a very strong coupling between the hydrodynamics and the structure. This is also numerically challenging, and a source of instabilities in the simulations. Finally, the experiments document scenarios where ventilation and cavitation play a role, and this further complicates the numerical problem.

To verify the co-simulation model properly, it is recommended to use an experiment or comparison that is not so extreme in nature. Measurements from full scale lifeboat drops are one alternative, and the numerical challenges related to such a simulation are considered to be fewer than for the experiment used in this thesis. Another interesting possibility is the experiment presented by Wang and Guedes Soares (2012). This is an idealized, three-dimensional experiment with hydroelastic responses that seem well suited to verify an FSI-model.

In Chapter 5 the capabilities of the model are demonstrated, but the setup chosen has some limitations. It was focused on hydroelastic slamming on very slender structures with a response dominated by nonlinearity. This is, to the candidate's knowledge, an unexplored field, as all theoretical formulations found for hydroelasticity are based on the small deformations

assumption. This makes it particularly interesting to investigate the results, and at the same time particularly challenging to compare the model to theoretical data. In hindsight, it might have been more convenient for the verification of the model if a linear system were chosen. Still, the fact that the numerical model was capable of capturing such extreme response behavior illustrates the possibilities of the FSI-analyses.

In the discussion on structural nonlinearity in Section 2.1.3, a simplified expression for the nonlinear deflection of the plate is used to compare with quasi-static analyses. Some work could be invested in finding a better comparable nonlinear expression that accounts for the bending stiffness. This was omitted, as the agreement with the simulations was satisfactory for the expression chosen. It is interesting to see that the zero-stiffness expression displays such good agreement with the simulation.

7. CONCLUSION

The main objective of this thesis has been to investigate hydroelastic slamming by establishing a numerical model to conducted coupled simulations between a CFD-code and a FEM-code. This has been achieved by using the commercial codes STAR CCM+ and Abaqus. Although the method requires the use of two independent commercial codes, it is found to be easily used, due to the built in co-simulation modules.

Water impact of a rigid wedge is simulated, and convergence tests with respect to domain size, mesh, time steps and number if iterations are presented. The model is compared to previous work and shows good agreement.

Additionally, the effect of viscosity and compressibility is investigated. It is concluded that viscosity may be neglected with an insignificant effect on the total vertical force on the wedge. It is concluded that artificial compressibility leads to an insignificant change in total vertical force on the wedge, and may be an effective way to reduce instabilities.

The FEM-code Abaqus is chosen for the structural simulations. Convergence tests are conducted with respect to mesh size, and the capabilities of the model are verified by comparison to theory.

Coupled FSI-analyses have been conducted. Convergence tests with respect to time steps, iterations, domain size, mesh size and coupling scheme are presented. The model is compared to experimental data. The agreement is poor, and it is concluded that the model setup does not accurately describe the physics of the experiment. Alternative experiments are proposed.

The impact of elastic wedges is parametrically studied by varying the Young's modulus of an elastic wedge. The effect of hydroelasticity and structural nonlinearity is investigated by comparing the results with quasi-static structural analyses and theoretical expressions for the response. It is concluded that hydroelasticity has a non-conservative effect on the highly deformed structures investigated. It is suggested that the main parameters dictating this non-conservativeness are the slenderness and stiffness of the structure.

One-way coupled simulations are compared to two-way coupled simulations, and the difference is seen to be significant. Particularly, the one-way coupled simulations show an oscillatory structural response that is avoided using the two-way coupled simulations.

Previous work on water impact and fluid-structure interaction is reviewed. A report demonstrating the relevance for free-fall lifeboats is presented.

A thorough description of the theory related to water impact of rigid and elastic wedges is presented. The CFD and FEM processes are described in detail, and the possibilities and limitations of coupling the solvers with one another are presented.

8. RECOMMENDATIONS FOR FUTURE WORK

For future work on CFD, FEM or coupling of the two, the software chosen for this work is strongly recommended. STAR CCM+ is a user-friendly software, with easy access to all the relevant parameters for the CFD-process. The possibilities to interact and visualize during the simulations have been very helpful. The software also has an easily accessible online documentation on theory and recommended practice. Abaqus is a well-known and much used software for complex FE-analyses. The coupling of Abaqus and STAR CCM+ is easy to set up, as both codes have integrated co-simulation modules specifically designed to couple with each another. If a student considers taking this work further, it is recommended that the student is familiar with at least one of the programs, as a considerable amount of time would be needed to familiarize with both codes.

As the results from the coupled analyses in this work deviate somewhat in comparison with experiments, different experiments are recommended to verify the model. For verification of the model, two setups are proposed. The experiment series presented by Wang and Guedes Soares (2012) seem easily reproduced, and are less extreme in nature than the experiment chosen in this thesis. A comparison to measurements from full scale experiment of the relevant structure is also recommended.

It is recommended to avoid a fixed-body approach as it was applied in this thesis. The limitations quickly outweigh the modeling convenience. An overset, morphing mesh combined with a DFBI-model is recommended. Limitations related to spatial correspondence between the models can be coped with by having Abaqus calculate the trajectory of the body.

The effect of varying structural nonlinearity should be investigated further to gain a good understanding of the mutual dependency between hydrodynamic forces and large structural responses.

The one-way coupled model used in this thesis worked excellently, and for problems with an assumed low degree of coupling between loads and responses, this method will give a robust and reliable method for analyzing FSI-problems. The method can be employed for hydroelastic analyses of such structures.

Curiously, the CFD-code STAR CCM+ has an integrated structural model, and the FEM-code Abaqus has an integrated CFD model. It would be interesting to compare the results from the co-simulations to results from simulations run internally in the two codes.

9. REFERENCES

AARSNES, J. 1994. An experimental investigation of the effect of structural elasticity on slamming loads and structural response. *Technology Report MT60 A95-0053,* 602119.

AARSNES, J. 2012. Compendium in hydroelasticity. *NTNU*.

CD-ADAPCO 2012. Documentation. www.cd-adapco.com.

DASSAULT-SYSTÈMES 2013. http://www.3ds.com/products/simulia/support/documentation/. *3DS.*

DNV 2010. DNV-RP-C205 Environmental conditions and environmental loads.

FALTINSEN, O. M. 1997. The effect of hydroelasticity on ship slamming. *Philosophical Transactions of the Royal Society of London. Series A: Mathematical, Physical and Engineering Sciences,* 355**,** 575-591.

FALTINSEN, O. M. 2000. Hydroelastic slamming. *Journal of Marine Science and Technology,* 5**,** 49-65.

FALTINSEN, O. M. & CHEZHIAN, M. 2005. A generalized Wagner method for three-dimensional slamming. *Journal of ship research,* 49**,** 279-287.

FERZIGER, J. H. & PERIC, M. 2011. *Numerische Strömungsmechanik,* Springer.

HTTP://THEMARITIMEBLOG.COM/. 2009. *http://themaritimeblog.com/wp-content/uploads/2009/07/FF1200.jpg* [Online].

JOHANNESSEN, S. R. 2012. *Use of CFD to Study Hydrodynamic Loads on Free-Fall Lifeboats in the Impact Phase.: A verification and validation study.* Master's thesis, NTNU.

KARMAN, V. 1929. The impact of seaplane floats during impact. *National Advisory Committee for Aeronautics*.

KOROBKIN, A., GUÉRET, R. & MALENICA, Š. 2006. Hydroelastic coupling of beam finite element model with Wagner theory of water impact. *Journal of Fluids and Structures,* 22**,** 493-504.

LARSEN, E. 2013. *Impact Loads on circular Cylinders.* Master's thesis, NTNU.

LU, C. H., HE, Y. S. & WU, G. X. 2000. Coupled Analysis of Nonlinear Interaction between Fluid and Structure during Impact. *Journal of Fluids and Structures,* 14**,** 127-146.

MARINTEK 2006. Confidential report.

MOAN, T. 2003. Finite Element Modelling and Analysis of Marine Structures. *NTNU*.

MOAN, T. 2012. Compendium in Nonlinear analysis. *NTNU*.

PANCIROLI, R. 2013. Hydroelastic Impacts of Deformable Wedges. *Dynamic Failure of Composite and Sandwich Structures.* Springer.

PANCIROLI, R., ABRATE, S. & MINAK, G. 2013. Dynamic response of flexible wedges entering the water. *Composite Structures,* 99**,** 163-171.

PANCIROLI, R., ABRATE, S., MINAK, G. & ZUCCHELLI, A. 2012. Hydroelasticity in water-entry problems: Comparison between experimental and SPH results. *Composite Structures,* 94**,** 532-539.

PIRO, D. J. & MAKI, K. J. Hydroelastic wedge entry and exit. Eleventh International Conference on Fast Sea Transport. Honolulu, Hawaii, USA, 2011.

TVEITNES, T., FAIRLIE-CLARKE, A. C. & VARYANI, K. 2008. An experimental investigation into the constant velocity water entry of wedge-shaped sections. *Ocean Engineering,* 35**,** 1463-1478.

WAGNER, H. 1932. Über Stoss- und Gleitvorgänge. *Z. Angew. Math. Mech.,* 12**,** 192-235.

WANG, H. & GUEDES SOARES, C. 2012. Numerical and experimental study of hydrodynamic impact and elastic response of one free-drop wedge with stiffened panels. *Ocean Engineering,* 40**,** 1-14.

WWW.PTIL.NO. 2005. *http://www.ptil.no/news/psa-follows-up-damage-to-lifeboat-on-veslefrikk-b-article2175-79.html* [Online].

ZHAO, R. & FALTINSEN, O. M. 1993. Water entry of two-dimensional bodies. *Journal of Fluid Mechanics,* 246**,** 593-612.

APPENDIX A

The Appendix contains monitor plots of the total vertical force of the wedge bottom for the different wetting time quotients presented in Chapter 5.

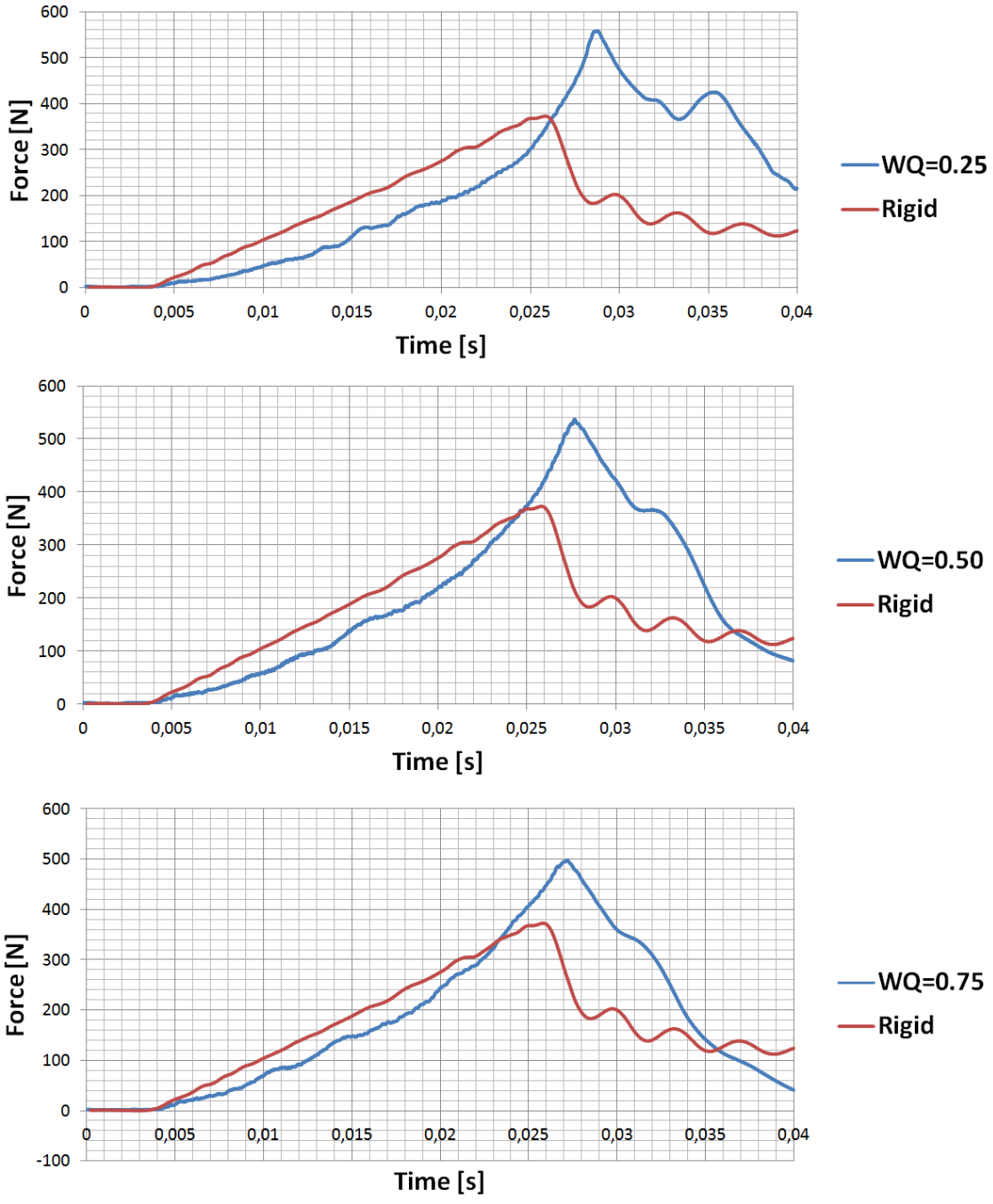

Figure 76 – Total vertical force on the wedge plate for wetting time quotients WQ=0.25, WQ=0.50 and WQ=0.75.

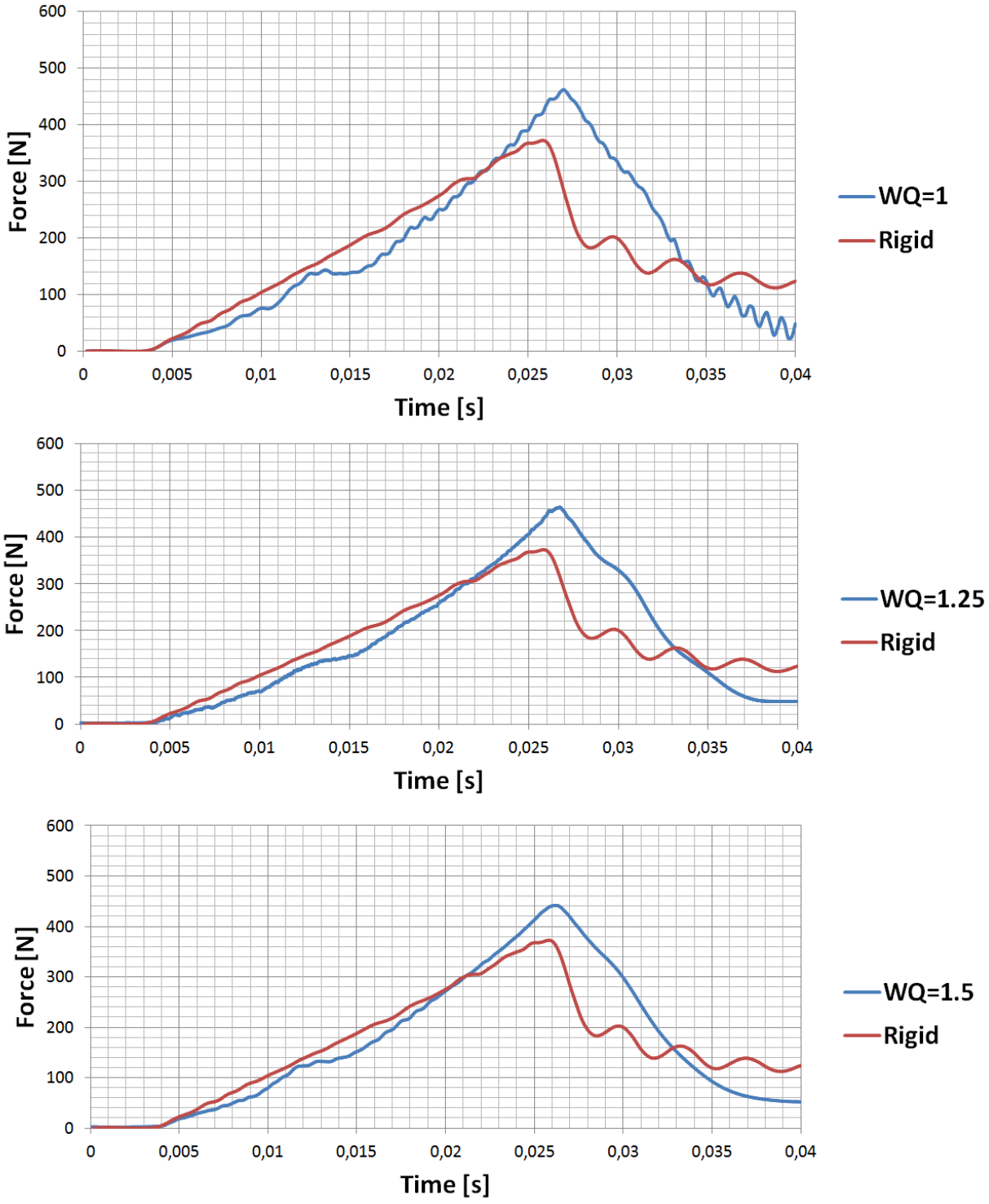

Figure 77 – Total vertical force on the wedge plate for wetting time quotients WQ=1.0, WQ=1.25 and WQ=1.5.

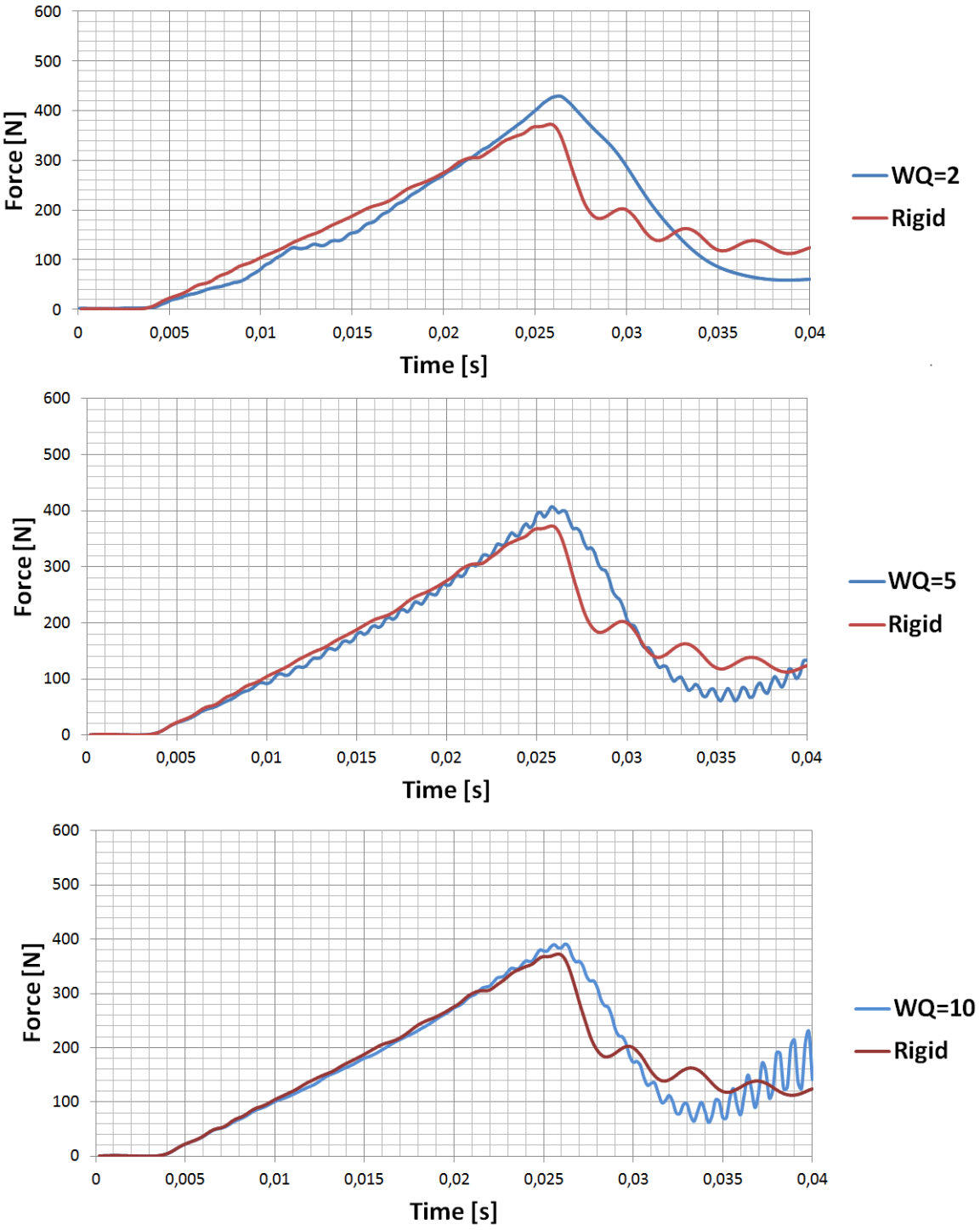

Figure 78 – Total vertical force on the wedge plate for wetting time quotients WQ=2, WQ=5 and WQ=10.

APPENDIX B

The Appendix contains a comparison between deformations at the midpoint of the wedge from one-way coupled simulations and two-way coupled simulations, as presented in Chapter 5.

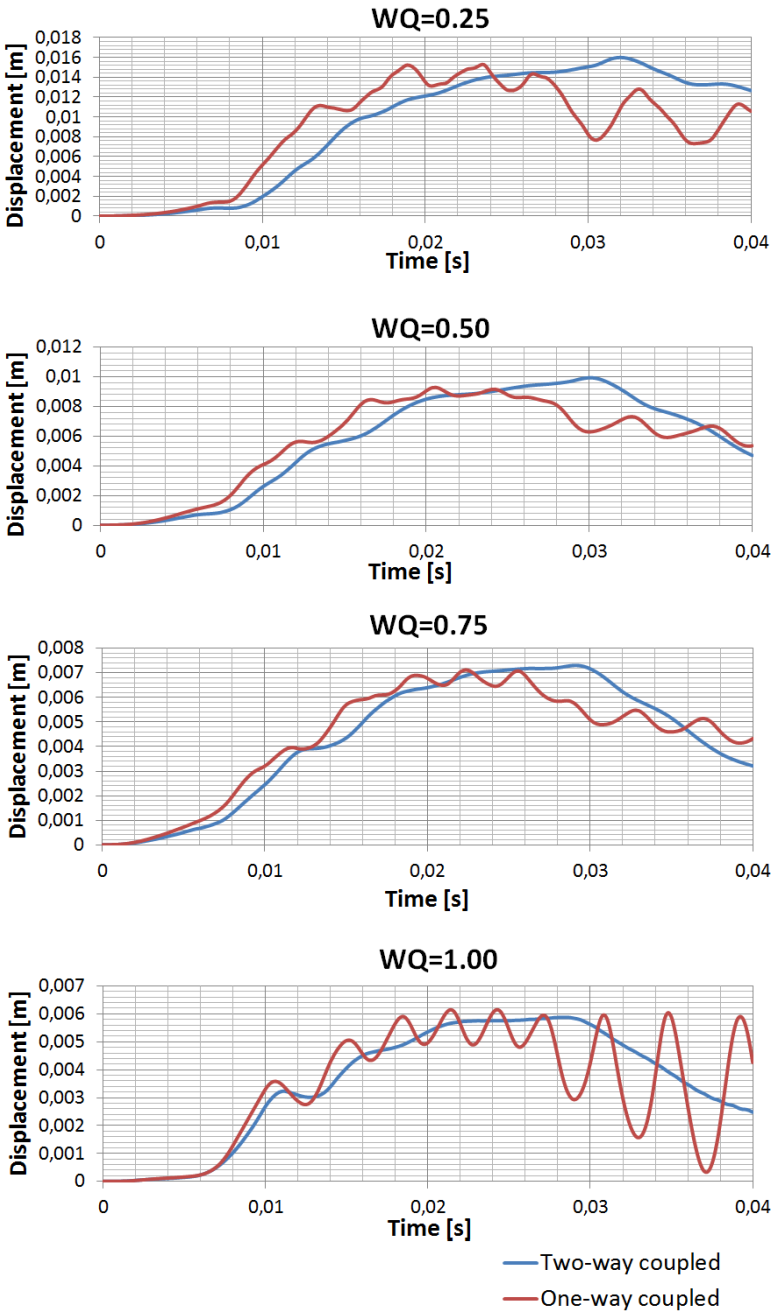

Figure 79 – Deformations at the midpoint of the wedge from one-way coupled simulations and two-way coupled simulations for WQ=0.25 to WQ=1.00.

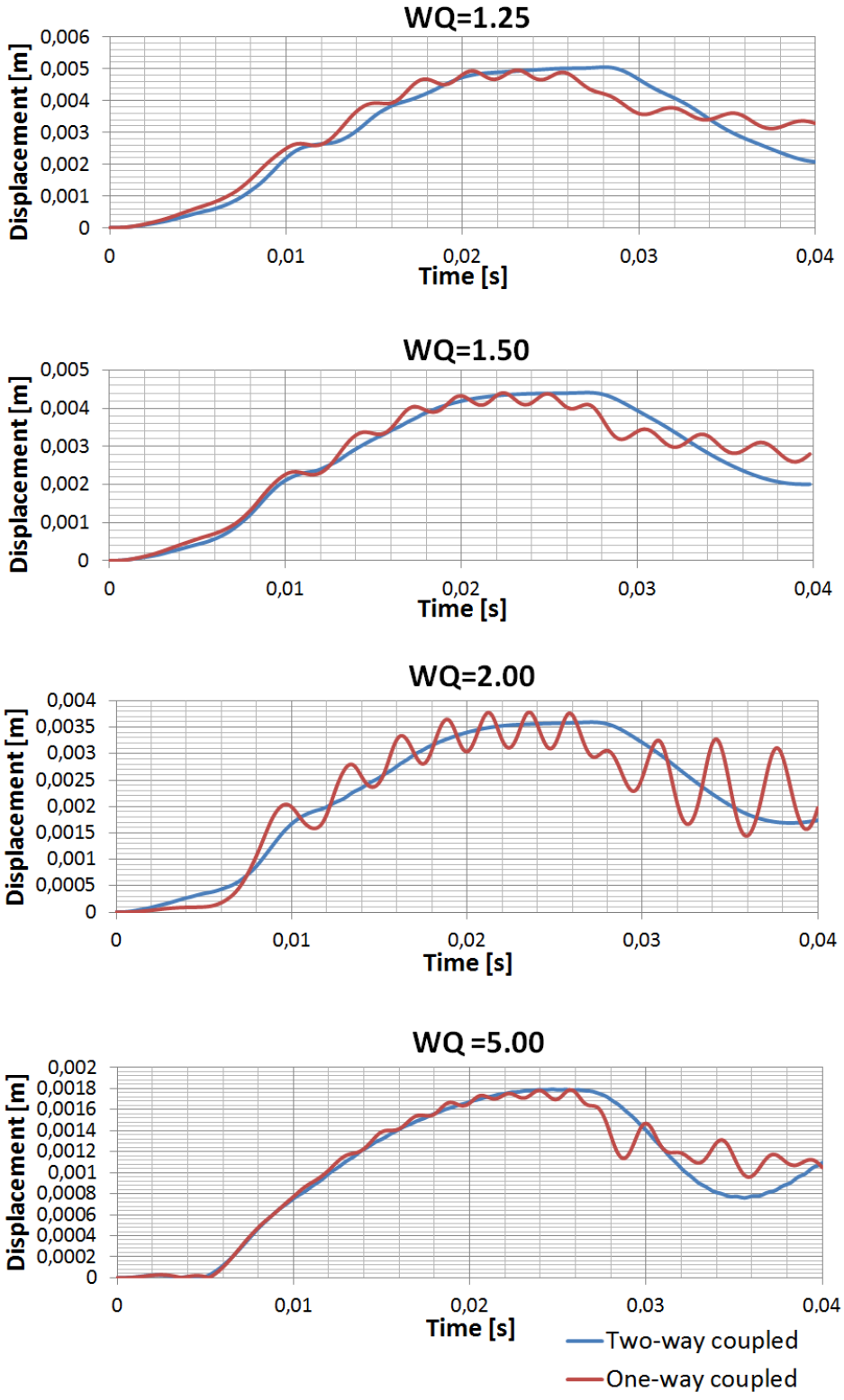

Figure 80 – Deformations at the midpoint of the wedge from one-way coupled simulations and two-way coupled simulations for WQ=1.25 to WQ=5.00.

APPENDIX C

The appendix contains displacement velocity magnitudes at the midpoint of the wedge for the two-way coupled simulations presented in Chapter 5.

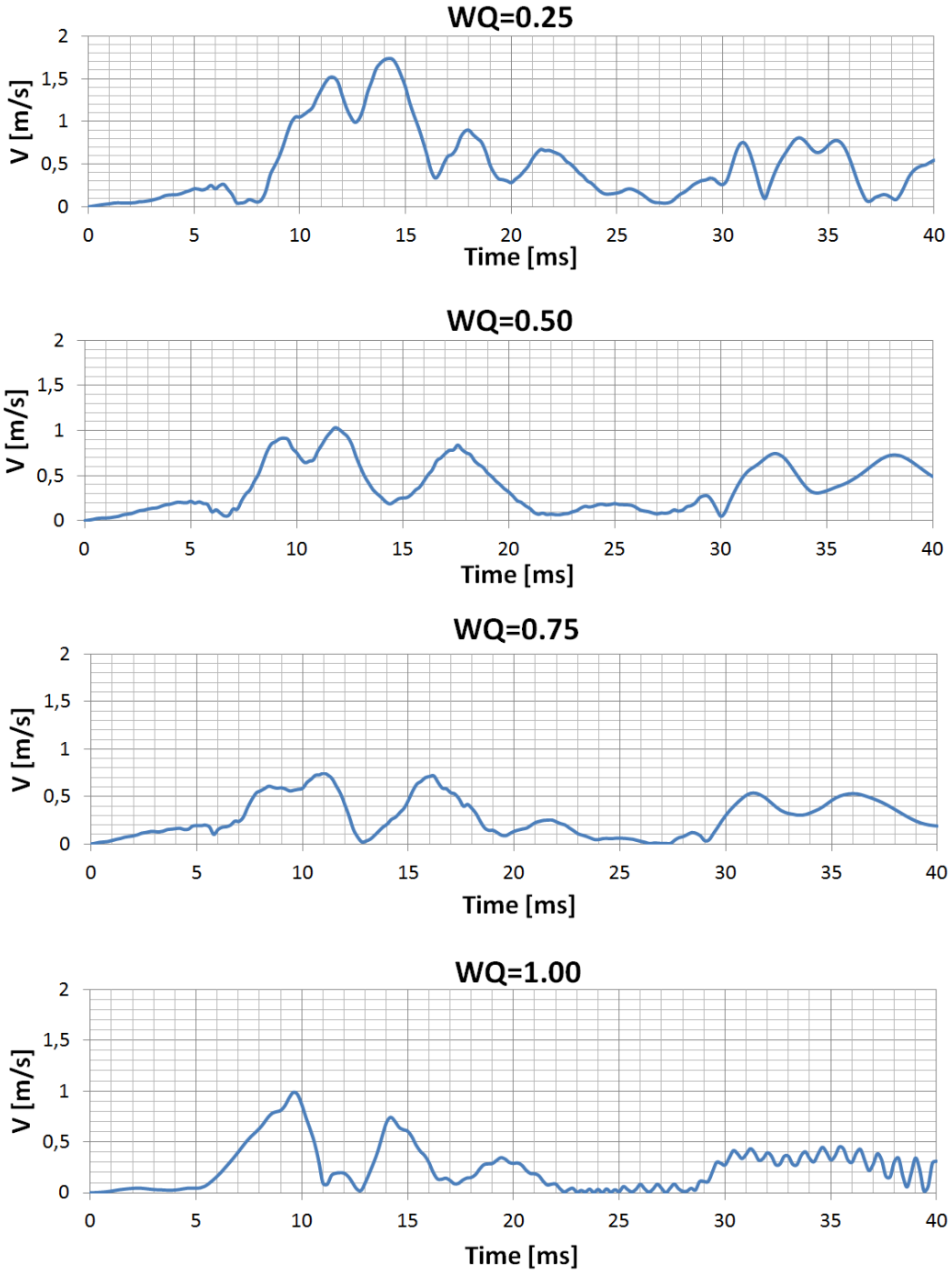

Figure 81 – Displacement velocity magnitudes at the midpoint of the wedge for two-way coupled simulations for WQ=0.25 to WQ=1.00.

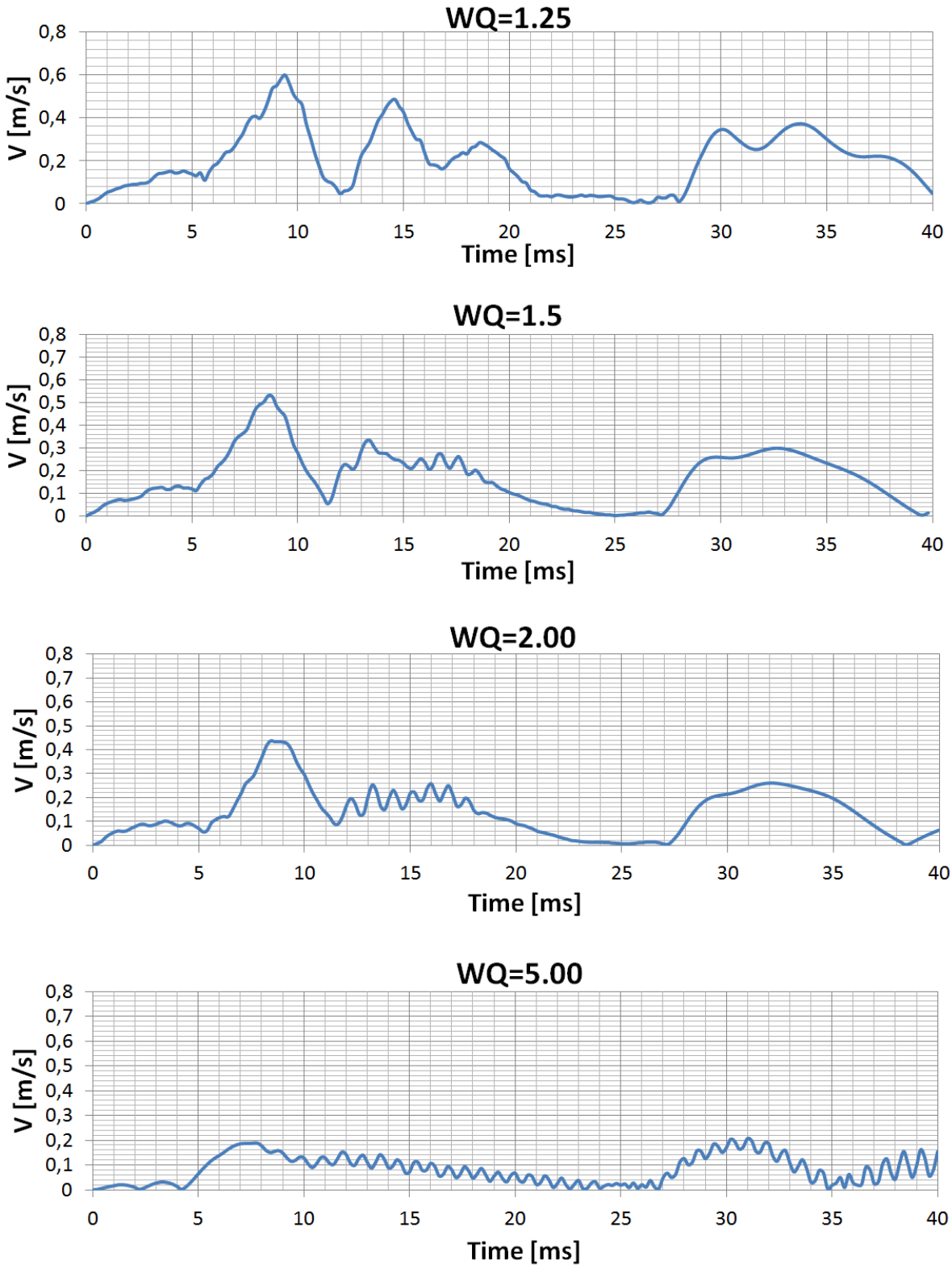

Figure 82 – Displacement velocity magnitudes at the midpoint of the wedge for two-way coupled simulations for WQ=1.25 to WQ=5.00.

APPENDIX D

The SIMPLE algorithm, as presented by CD-ADAPCO (2012).

SIMPLE Solver Algorithm

The SIMPLE algorithm is used to control the overall solution. This algorithm is summarized as follows:

1. Set the boundary conditions.
2. Computed the reconstruction gradients of velocity and pressure.
3. Compute the velocity and pressure gradients.
4. Solve the discretized momentum equation to create the intermediate velocity field $\mathbf{v}^*$.
5. Compute the uncorrected mass fluxes at faces $\dot{m}_f^*$.
6. Solve the pressure correction equation to produce cell values of the pressure correction p'.
7. Update the pressure field:
$$p^{n+1} = p^n + \omega p' \quad (181)$$
where ω is the under-relaxation factor for pressure.
8. Update the boundary pressure corrections p'_b.
9. Correct the face mass fluxes:
$$\dot{m}_f^{n+1} = \dot{m}_f^* + \dot{m}'_f \quad (182)$$
10. Correct the cell velocities:
$$\mathbf{v}^{n+1} = \mathbf{v}^* - \frac{V\nabla p'}{\mathbf{a}_p^{\mathrm{v}}} \quad (183)$$
where $\nabla p'$ is the gradient of the pressure corrections, $\mathbf{a}_p^{\mathrm{v}}$ is the vector of central coefficients for the discretized linear system representing the velocity equation and V is the cell volume.
11. Update density due to pressure changes.
12. Free all temporary storage.